Understanding up-down asymmetry in ferroelectric oxide materials

A Dissertation presented

by

Simon Divilov

to

The Graduate School

in Partial Fulfillment of the

Requirements

for the Degree of

Doctor of Philosophy

in

Physics

Stony Brook University

August 2018

Stony Brook University

The Graduate School

Simon Divilov

We, the dissertation committee for the above candidate for the

Doctor of Philosophy degree, hereby recommend

acceptance of this dissertation

Marivi Fernández-Serra - Dissertation Advisor
Associate Professor, Department of Physics and Astronomy

Matthew Dawber - Chairperson of Defense
Associate Professor, Department of Physics and Astronomy

Joanna Kiryluk
Associate Professor, Department of Physics and Astronomy

Taejin Kim
Assistant Professor, Department of Material Sciences and Engineering

This dissertation is accepted by the Graduate School

Charles Taber
Dean of the Graduate School

Abstract of the Dissertation

Understanding up-down asymmetry in ferroelectric oxide materials

by

Simon Divilov

Doctor of Philosophy

in

Physics

Stony Brook University

2018

Ferroelectrics are defined as materials whose spontaneous electric polarization can be reversed with an applied external electric field. An important family of ferroelectrics is oxides (chemical formula ABO_3), whose simple structure and robustness to degradation make them attractive candidates for both theoretical and engineering applications. However, ferroelectric oxides typically exhibit an unwanted phenomenon, known as up-down asymmetry, where one polarization state is easier to switch, using an external electric field, than the other. In the first part of this thesis we study bulk $PbTiO_3$ using Landau-Ginzburg-Devonshire mean field theory (LGDT) and density functional theory (DFT). We find that the up-down asymmetry can be understood as a built-in electric field, inside the ferroelectric, produced from the collective interactions of Pb-O divacancy (DV) dipole moments, causing one polarization state to be more energetically favorable. These collective interactions are represented, in the free energy of the ferroelectric, as linear coupling of the built-in electric field to the bulk polarization and interfaces of divacancies. In the second part of this thesis we study, using DFT, $PbTiO_3/SrTiO_3$ and $PbTiO_3/SrRuO_3$ superlattices. We show that the up-down asymmetry in $PbTiO_3/SrTiO_3$ is determined by the growth direction of the superlattice that fixes the direction of Pb-O DV dipole moments. However, in $PbTiO_3$/$SrRuO_3$ we find two regimes, based on the PbTiO3 layer thickness, with different polarization states that are more energetically favorable. For thin $PbTiO_3$ layers, the state is determined by the ordering of the PbO and RuO_2 planes at the interface of the $PbTiO_3$ and $SrRuO_3$ layers. While for thick $PbTiO_3$ layers, the state is determined by a Pb-O DV in those planes. Using the understanding of how the preferred polarization state is determined in each superlattice, we show, that we can control and effectively remove the up-down asymmetry by growing combined $PbTiO_3$/$SrTiO_3$/$PbTiO_3$/$SrRuO_3$ superlattices.

To my brother and parents

Contents

List of Figures

List of Tables

Preface

I have chosen to write this thesis in two parts. The first part of my thesis includes a non-exhaustive collection of derivations and detailed explanations (with plenty of references) about useful theories and methods needed to understand my work. Primarily, this was done to further my own understanding of the research topics. However, I hope my attempts will be fruitful to perspective students looking to build and improve on my work. The second part of my thesis includes the actual details of my work, which seasoned researchers of the field should skip to.

Acknowledgments

There are a number of individuals who have made this thesis a successful reality. I owe an immense gratitude to my advisor Prof. Marivi Fernández-Serra, whose patience and dedication with me was essential in nurturing my academic career. Countless discussions with Marivi honed my skills as a scientist and researcher. She taught me how to approach complex problems and ask the right questions. My biggest appreciation was that Marivi allowed me to pursue topics and ideas that I found interesting, while still being under her guidance as I built up my confidence in research. The work-life balance Marivi set for her group and me has made this chapter in my life an overall very positive and enjoyable experience that I will look back on in the future. I am also very grateful to her for helping me secure a postdoctoral position.

I am extremely indebted to Prof. Matt Dawber who I worked with very closely in my research. His insights and explanations were useful in furthering my understanding of the work I was doing. Being able to be part of his group and sit in on their group meetings really gave me a new appreciation for the experimental side of physics. Matts great character made going to their group meetings even more enjoyable.

I am extremely grateful to Prof. Max Stengel for not only providing me his first principles code that allowed be to complete my thesis, but also answer the large number of questions that I had using his code. I am also thankful to Prof. Phil Allen whose profound questions and seasoned perspective on problems always gave me something to ponder about. I would also like to extend my thanks to the defense committee group members Prof. Joanna Kiryluk and Prof. Taejin Kim for taking the time to read my thesis and sit on my defense.

I would like to thank Greg for the wonderful experimental results he was able to produce, as well as his help in helping me understand the intricacies of the experiments needed to supplement my work. I would also like to thank Judith whose thesis was a springboard to helping me understand the subject I have been researching now for a few years. In addition, I would like to thank Luana and Betul for taking the time to aid me in debugging first principle codes, while also allowing me to ask them an immense number of question. I would also like to thank the IACS staff who have been accommodating whenever I had bugs or needed printing. Also I want to thank the Rutgers group, especially Prof. Karin Rabe, Prof. Premi Chandra and John for their useful discussions.

Next, I want to thank my former group mates Dan, Adrian and Jean Paul for fruitful discussions and fun experiences during conferences. I would also like to thank all my other group mates Jian, Vidushi, Michelle and Sebastian who have made group meetings very enjoyable. I would also like to extend my thanks to the experimental group members I had the pleasure interacting with, Ben, Sara, Humed, Anya, Giulia, Amanda and Rui.

I would like to thank all the Stony Brook professors I took classes with who made me realize the amount of work I needed to put into being successful at something I enjoy. With that, I would also like to thank my undergraduate physics professors at City College who made me realize physics is something that I enjoy, specifically Prof. Tim Boyer, Prof. V. P. Nair and Prof. Alexios Polychronakos.

Next, I would like to thank the people who made a difference in my personal life. I would like to thank Arya for a wonderful friendship that we had over so many years since I started my graduate studies in physics, I have learned a lot from you. My other friends who gave me a lot of fun memories, Marc, John, Zack, and Chris, it was always a pleasure hanging out together. I would also like to thank Anna, her wisdom and compassion, as well as our great experiences, are things that I deeply value.

With great pleasure I would like to sincerely thank my parents whose sacrifices and love made me the person I am today and allowed me to pursue a career path that brought tremendous enjoyment to my life. To that, I want to extend my gratitude to my relatives for being supportive and extremely caring to me. Finally, and most importantly, I want to thank my loving brother for always being their for me as my equal.

Part I
Theory and Methods

1 Introduction

Ferroelectric materials are insulators with multiple stable or metastable states, defined by their electric polarization, where switching between the states is achieved with an applied external electric field. In this section we discuss the basis of ferroelectricity, specifically its microscopic origins and dynamics, as well as, experimentally detecting ferroelectric states. Then we discuss a specific family of materials, known as perovskite oxides, some of which are ferroelectric, in superlattice nanostructure form. Finally, we briefly discuss some applications of ferroelectric oxides and the problems associated with them which we investigate in the thesis.

1.1 Ferroelectricity

1.1.1 Crystallography

The stable or metastable states in a ferroelectric material are referred to as spontaneous polarizations. Physically, the spontaneous polarization, in a conventional ferroelectric, is a product of the atomic positions in the crystal. However, it is important to note, that just because the crystal is polarized does not make it a ferroelectric. The key attribute is the ability of the crystal to transition between different polarization states through atomic displacements forced by the external electric field. For this to exist, a ferroelectric crystal must have a non-polar, high symmetry phase and a polar, lower symmetry phase, where the symmetry-breaking transition occurs through atomic displacements. It turns out that this constraint severely limits the crystallographic structures which allow for ferroelectricity.[1]

1.1.2 Microscopic origins

Perovskite oxides, chemical formula ABO_3, where A and B are cations and O is an anion, are a class of crystal structures that allow for such a symmetry-breaking transition. In their non-polar high symmetry phase, the perovskite has a cubic centrosymmetric structure shown in Fig. 1. However, for atomic displacements to occur and create a ferroelectric phase the long range Coulomb forces need to be more energetically favorable than the short range repulsion forces that stabilize the centrosymmetric phase. Such a condition depends on the bonding characteristics of the ions and is known as a second-order Jahn-Teller (SOJT) effect. We can define this effect by a perturbative expansion of the centrosymmetric state energy in terms of the atomic distortion Q as[1]

$$E(Q) = E(0) + \frac{1}{2}\left(\langle 0|\delta^2 H/\delta Q^2|0\rangle - 2{\sum_n}' \frac{|\,\langle 0|\delta H/\delta Q|n\rangle\,|^2}{E_n - E(0)}\right) + \cdots \quad (1.1.1)$$

where the linear term in Q is discarded due to the centrosymmetry of the system. Here H, $E(0)$ and E_n is the Hamiltonian of the system, the energy of the centrosymmetric state and the energy of the excited states, respectively. The first term in the bracket describes the energy change due to atomic distortions, which is dominated by Coulomb repulsion, and therefore it is always positive. The second term in the bracket describes the energy change due to atomic distortions, taking into account electron redistribution, and from inspection is always negative. Evidently, to produce a SOJT effect and achieve ferroelectricity the second term must be larger than the first. For this to occur the excited state needs to be close in energy with the centrosymmetric state such that $E_n - E(0)$ is as small as possible, and $\langle 0|\delta H/\delta Q|n\rangle$ cannot be zero, meaning that the excited state, where the electrons redistribute, cannot be centrosymmetric. A simple physical example where this occurs is $BaTiO_3$ where the Ti cation is shifted off-center, due to the hybridization between the Ti 3*d* and O 2*p* orbitals, creating a polarized non-centrosymmetric structure.

Another possible mechanism to stabilize polar order in a centrosymmetric perovskite is oxygen octahedra rotations. While such rotations do not produce a ferroelectric nor a non-centrosymmetric state, they lower the overall energy difference $E_n - E(0)$ and in conjunction with SJOT help facilitate a ferroelectric phase transition. Sometimes the rotations stabilize dipole moments in adjacent cells that are in opposite directions giving no net polarization in the material, as in the case of antiferroelectric $PbZrO_3$. Hence the oxygen octahedra rotations are sometimes referred to as antiferrodistortive rotations.

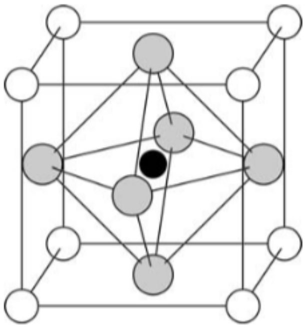

Figure 1: Unit cell of a cubic centrosymmetric perovskite crystal. The A cation, B cation and O anion are represented by white, black and grey spheres, respectively. Taken from Ref. [1]

1.1.3 Switching dynamics

The switching of a ferroelectric into a different state is not an instantaneous process nor is the switching process uniform throughout the material.[6] Nevertheless, Landau theory of phase transitions, which models the physics of switching the spins in a ferromagnet from up to down, has been used to great success to model the switching of the spontaneous polarization in a ferroelectric. However, the caveat is that Landau theory predicts the electric coercive field to be several orders of magntitude higher than what is observed experimentally.[6] This is because in the Landau theory the switching is governed by homogeneous nucleation, whereas, in reality, domains and domain wall kinetics are important in explaining the switching. Typically the switching occurs via the following step-wise Kolmogorov-Avrami-Ishibashi process: (i) a spherical microscopic domain, of opposite polarization, is formed in the polarized material, (ii) the domain spherically expands, at the speed of sound, until it reaches a critical diameter, determined by the surface tension of the domain wall, (iii) then the domain expands along the direction of the applied electric field, and (iv) finally when it reaches the boundary of the material or electrodes, it expands in the perpendicular direction.[6] However, in perovskite oxides the switching rate is limited by the nucleation of domains.[7] This is because the dependence of the domain nucleation time on the applied electric field E is $\sim \exp(1/E^2)$. Hence even for an infinite applied electric field, the nucleation time approaches a constant and does not go to zero.

1.1.4 Experimental measurement of switching

In an ideal ferroelectric, measuring the polarization while varying the applied electric field to switch between the two spontaneous polarization states would produce a (polarization-Efield) P-E hysteresis loop analogous to a M-H hysteresis loop in ferromagnets. However to accurately measure the hysteresis curve, in an experiment, can be a challenge, since not only can the sample be less than ideal, but also the electrodes and wires need to be accounted for. One popular way to measure the polarization, while discriminating against artifacts, is the positive-up negative-down (PUND) measurement. This measurement, shown in Fig. 2, involves a succession of five pulses, where the pulse is a brief period of an applied electric field or voltage. To begin the measurement an initial pulse (0) is sent to polarize the material in a particular polarization direction (up or down), then two pulse (1 and 2) in the opposite direction are applied, finally two more pulses (3 and 4) are sent in the direction of the initial pulse. Two pulses of the same voltage are sent to verify that the sample is fully polarized. In addition, we should not observe a change in the current between two pulses of the same voltage sign, allowing us to verify that no artifacts exist. A current is only produced when the sign of the voltage between two pulses is different and integrating the current with respect to time yields the polarization.

1.2 Perovskite Oxides

Perovskite oxides, with chemical formula ABO_3, is a very diverse family of materials. The compound, depending on the A and B cations, can be insulating or metallic and exhibit polar or magnetic order.[1]

1.2.1 $PbTiO_3$

$PbTiO_3$, the main material of interest in this thesis, has a paraeletric-ferroelectric phase transition at 760K. When $PbTiO_3$ is paraeletric, the unit cell is cubic with space group $Pm\bar{3}m$ where the Pb cation is on the corners of the cube, the Ti cation is in the center of the cube, and the O anion is on the faces of the cube, which make up an oxygen octahedra. In the ferroelectric state, the material is tetragonal with space group $P4mm$ and lattice constants $a = 3.904$ and $c = 4.152$ with a polarization of 75 μC/cm^2 at room temperature.[1] As previously discussed, the polarization is much

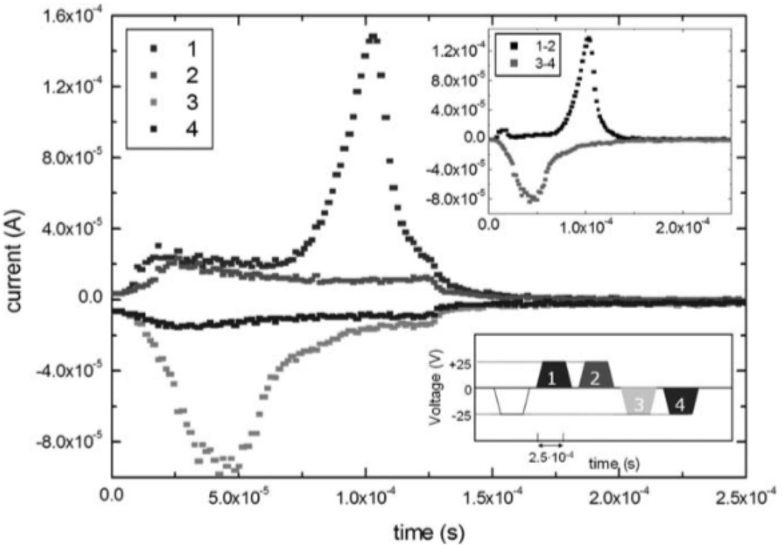

Figure 2: PUND measurement of a ferroelectric $PbTiO_3/SrTiO_3$ superlattice. The lower inset shows the voltage and time delay of the pulses. The upper inset shows the difference in the current between the 1st and 2nd pulse and the 3rd and 4th pulse. Taken from Ref. [1]

higher than one would expect if we just consider a simple ionic model, where Pb, Ti and O have charges of +2, +4, and -2, respectively. The primary reason for this is the hybridization between the Ti and O orbitals and the Pb and O orbitals.[8] The hybridization of the Ti 3d and O 2p orbitals weakens the short-range ionic repulsion, allowing for a larger displacement of the Ti ion from the center (shorter Ti-O bond), which enhances the ferroelectric order. Likewise, hybridization of the Pb 6s and 6p orbitals with the O 2p orbitals allow for shorter Pb-O bonds, stabilizing the polar tetragonal phase which indirectly enhances the ferroelectric order. The secondary reason, like for many perovskite oxides, is a strong coupling between the strain and ferroelectricity.[1] The in-plane strain, from the relatively small ionic radius of Pb, helps stabilize the polar tetragonal phase of the material.

1.2.2 $SrTiO_3$

$SrTiO_3$ is paraelectric and cubic with space group $Pm\bar{3}m$ and lattice constant $a = 3.905$Å. At 120K the material undergoes a structural phase transition where the oxygen octahedra undergo a antiferrodistortive (AFD) rotation, shown in Fig. 3, around a crystallographic axis lowering the overall symmetry of the crystal to the $I4/mcm$ space group. The material has a polar phonon, which is responsible for ferroelectric stability, with a frequency that decreases as the temperature is lowered. If the frequency of the polar phonon vanishes then $SrTiO_3$ can have a paraeletric-ferroelectric phase transition. However, even at low temperatures, the ferroelectric transition never occurs due to zero-point energy, preventing the frequency of the phonon from disappearing.[1] Hence the material is commonly referred to as an incipient ferroelectric. Although, it is possible, through the engineering of epitaxial strain or defect gradients, to convert the material into a ferroelectric.

1.2.3 $SrRuO_3$

$SrRuO_3$ is a metallic, itinerant ferromagnet with T_c around 150K which does not exhibit ferroelectric characteristics. The material is pseudo-cubic with space group $Pnma$ and lattice constant $a = 3.93$Å. The lack of polar order in the material has to due with the competing nature of ferromagnetism and ferroelectricity in perovskite oxides. To stabilize ferromagnetism, the *d* orbitals in the B ion need to be localized, where as, to stabilize ferroelectricicty, the *d* orbitals in the B ion need to hybridized.[1] Due to the oxygen

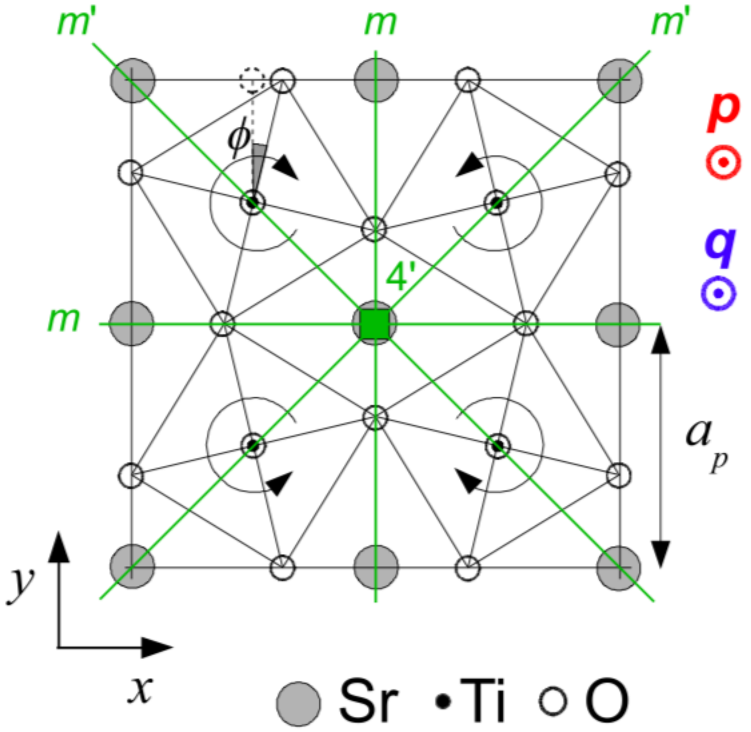

Figure 3: Oxygen antiferrodistortive rotations by angle ϕ in $SrTiO_3$ around the **q** vector. If the system was also ferroelectric the polarization would be along the **p** vector. The green text represents the symmetry operators associated with the rotations. Taken from Ref. [2]

octehdra that surround the Ru ion, the five degenerate Ru 4*d* orbitals split in energy into doubly degenerate e_g orbitals and triply degenerate t_{2g} orbitals. Both the e_g and t_{2g} orbitals are important for magnetic order.[9] Transport experiments on the the material reveal that it has a relatively poor conductivity and the temperature dependence on the conductivity does not follow conventional Drude theory.[10]

1.3 Superlattices

Superlattices are nanostructures where two or more materials are artificially layered on top of each other, in an alternating pattern, resulting in the interplay between the materials and leading to interesting physics.

1.3.1 $PbTiO_3/SrTiO_3$

$PbTiO_3/SrTiO_3$ superlattices are good candidate to probe the strain-ferroelectrcity coupling present in many perovskite oxides. The strain is produced due to the in-plane lattice mismatch during the growth process (a_{PTO} = 3.935 Å and a_{STO} = 3.925 Å). First principles and electrostatic models reveal that the system prefers to have the same polarization in both $PbTiO_3$ and $SrTiO_3$ layers, even at the energy cost of polarizing the paraelectric layers.[11] One would also expect that the ferroelectricity of the whole superlattice to scale with the thickness of the $PbTiO_3$ layers. However, experimental data has shown[11] that even for a single layer of $PbTiO_3$ the superlattice retains its ferroelectricity and domain structure. It turns out that for the short periods superlattices there are AFD rotations in the bilayers. This leads to a coupling between AFD rotations and polarization which lowers the overall energy and allows the superlattice to retain its ferroelectricity.[12]

1.3.2 $PbTiO_3/SrRuO_3$

Similar to $PbTiO_3/SrTiO_3$ superlattices, $PbTiO_3/SrRuO_3$ superlattices also involve the coupling of strain to ferroelectricity, which is achieved by growing the superlattice on an $SrTiO_3$ substrate. However there are also a number of differences. The first difference is that we have a ferroelectric/metal bilayer and second is that the interface has a broken inversion symmetry because the two materials have different A and B cations. The metallic characteristics of the superlattice leads to a two dimensional electron gas at the interface for sufficiently thick $PbTiO_3$ layers.[13] While the compositional breaking of the inversion symmetry leads to the superlattice self-poling in a particular direction due to one polarization state being more energetically favorable than the other. This effect is particularly attractive in piezoelectric devices where the goal is to apply an electric field either with or against the preferred polarization to increase or decrease the size of the material, respectively. The strength of the self-poling scales with the thickness of the $PbTiO_3$ layer. Theoretical and experimental data has shown[13] that the superlattice is not ferroelectric below 3/1, is an asymmetric ferroelectric between 3/1 and 7/1, and above 7/1 it is a conventional ferroelectric.

1.4 Applications

Ferroelectrics have a wide range of applications, of which, we only partially cover here and suggest Ref. [1] for further reading. For many years, ferroelectrics have been considered to be the most likely candidates for the next generation technology of non-volatile memory. Non-volatile memory is a highly desirable method of information storage with the advent of FLASH technology. Ferroelectric field effect transistors is an active field of research, where the ferroelectricity can potentially modify superconducting and magnetic properties of materials. In addition, since all ferroelectric are piezoelectrics, atomic force microscopy can be used to write extremely dense domains for information storage. Finally, ferroelectric nanostructures, such as superlattices are ideal candidates for nanocapacitor technology, due to retention of ferroelectricity at sub-micron sizes.

1.5 Problems

There are a number of problems associated with ferroelectric perovskite oxides which are related to the switching dynamics. The two most commonly discussed are fatigue and up-down asymmetry (sometimes referred to as imprint).[14] Fatigue is the decrease in magnitude of the polarization after repeated switching between the two polarization states, and up-down asymmetry occurs when one polarization state is easier to switch than the other. In this thesis we address the problem of up-down asymmetry for bulk $PbTiO_3$, as well as, $PbTiO_3/SrTiO_3$ and $PbTiO_3/SrRuO_3$ superlattices. In understanding this problem we provide potential solutions on how to synthesize symmetric ferroelectric devices.

2 Phenomenology

2.1 Mean Field Theories

A mean field theory ignores long range correlations to create a simpler model in an attempt to explain physical phenomena. In this section we will focus on Landau's formulation of a mean field theory to explain continuous phase transitions. While it is known that a phase transition in a crystal is accompanied by an abrupt change in its symmetry, Landau made the realization[15] that near the transition the electron density should exhibit a continuous change. This is evident if we think of the electron density $\rho(\mathbf{r})$ near the phase transition as $\rho_0 + \Delta\rho$, where ρ_0 is the electron density of the initial phase of space group S_1 and $\Delta\rho$ is a perturbation of the electron density with a lower space group S_2, therefore ρ has space group S_2. Clearly the phase transition in symmetry from S_1 to S_2 is discrete, yet the change in the electron density is continuous. This observation led Landau to formulate the energetics of the phase transition in a similar fashion, where, given a lowering of the space group, you have a perturbation in some continuous variable.

2.1.1 Landau Theory

We begin by considering the relevant thermodynamic potential Φ_γ, with a set of state variables $\{\gamma\}$, for the system, as a functional of the electron density. Near the phase transition, using the properties of functionals, we may write

$$\Phi_\gamma[\rho] = \Phi_\gamma[\rho_0 + \Delta\rho] = \Phi_\gamma[\rho_0] + \Phi_\gamma[\Delta\rho]. \tag{2.1.1}$$

Next we can expand the second term in a functional Taylor series[16] arriving at

$$\Phi[\rho] = \Phi[\rho_0] + \int \frac{\delta\Phi[\rho_0]}{\delta\rho(\mathbf{r})}\Delta\rho(\mathbf{r})d\mathbf{r} + \frac{1}{2}\int \frac{\delta^2\Phi[\rho_0]}{\delta\rho(\mathbf{r})\delta\rho(\mathbf{r}')}\Delta\rho(\mathbf{r})\Delta\rho(\mathbf{r}')d\mathbf{r}d\mathbf{r}' + \cdots \tag{2.1.2}$$

where γ is omitted for clarity. Now let us represent the symmetry group of $\Delta\rho$ as linear representations, so that

$$\Delta\rho(\mathbf{r}) = \sum_i c_i'\phi_i(\mathbf{r}) \tag{2.1.3}$$

where c'_i and ϕ_i is the normalization coefficient and the electron density of the i'th irreducible representation, respectively.[15] Inserting Eq. 2.1.3 into Eq. 2.1.2 and making use of Schur's lemma for irreducible representations,[15, 17] we can set all terms with odd powers of ϕ_i to zero. In other words, we can write

$$\begin{aligned}\Delta\rho(\mathbf{r})\Delta\rho(\mathbf{r}') &= \sum_i c'_i\phi_i(\mathbf{r})\sum_j c'_j\phi_j(\mathbf{r}') \Rightarrow \sum_{i,j}\delta_{ij}c'_ic'_j\phi_i(\mathbf{r})\phi_j(\mathbf{r}') \\ &= \sum_i c'^2_i\phi_i(\mathbf{r})\phi_i(\mathbf{r}') = \sum_j c_j^2\sum_i \phi_i(\mathbf{r})\phi_i(\mathbf{r}')\end{aligned} \tag{2.1.4}$$

where δ_{ij} and c_j is the Kronecker delta and the renormalized coefficient, respectively. Now let us define the following

$$\Delta\Phi = \Phi[\rho] - \Phi[\rho_0] \tag{2.1.5a}$$

$$\sum_j c_j^2 = \eta^2 \tag{2.1.5b}$$

$$A = \sum_i \int \frac{\delta^2\Phi[\rho_0]}{\delta\rho(\mathbf{r})\delta\rho(\mathbf{r}')}\phi_i(\mathbf{r})\phi_i(\mathbf{r}')d\mathbf{r}d\mathbf{r}' \tag{2.1.5c}$$

where η is referred to as the order parameter. This allows us to recast Eq. 2.1.2 as

$$\Delta\Phi = \frac{1}{2}A_\gamma\eta^2 + \frac{1}{4}B_\gamma\eta^4 + \cdots \tag{2.1.6}$$

where B has a similar definition as A.[15] This is one of the main results of Landau theory, where η now controls the strength of the perturbation. It is interesting to note, from the definition, η is positive definite, and therefore the usual undergraduate derivation of Landau theory based on symmetry arguments of the order parameter would not be applicable. In principle, we can have more than one order parameter, but we do not consider this case here.

The applicability of Landau theory is determined by the Ginzburg criterion,[18] which can be written as

$$\left\langle(\delta\eta)^2\right\rangle \ll \left\langle\eta^2\right\rangle \tag{2.1.7}$$

where $\delta\eta$ is the fluctuation of the order parameter. Deferring the details of calculation, we simply state that for Landau theory to be valid the average fluctuations of the order parameter should be much smaller than the order parameter itself.

2.1.2 Landau-Devonshire Theory

A comprehensive application of Landau's theory to ferroelectricity was first attempted by Devonshire,[19] where the order parameter is associated with the polarization P. For completeness we expand the Helmholtz free energy, truncating terms higher than 4th order

$$F = \frac{1}{2}AP^2 + \frac{1}{4}BP^4 - EP \tag{2.1.8}$$

where E is the applied electric field. As an example we derive the Curie-Weiss law for a ferroelectric, in the absence of an applied field, by first minimizing Eq. 2.1.8 with respect to P, and solving

$$\frac{\partial F}{\partial P} = AP + BP^3 = 0 \tag{2.1.9}$$

giving us two solutions, $P = 0$ and $P^2 = -A/B$. The two solutions corresponding to a stable paraelectric and ferroelectric phase. Usually, A is taken to be $A_0(T - T_c)$, where T_c is the Curie temperature and B is temperature independent. Hence we arrive at the well known result

$$P(T) = \sqrt{\frac{A_0(T_c - T)}{B}}. \tag{2.1.10}$$

An important characteristic of some ferroelectrics (called piezoelectrics) is their response to strain and in general we can write[5] the free energy (again truncated), only for uniaxial strain, as

$$F = \frac{1}{2}Ks^2 + Q_1 sP + Q_2 sP^2 - \sigma s \tag{2.1.11}$$

where K, Q_i, σ, is the elastic constant, coupling constant and hydrostatic stress constant, respectively. Since we now have two order parameters, we should minimize Eq. 2.1.11 for both order parameters. For now let us minimize with respect to s and solve

$$\frac{\partial F}{\partial s} = Ks + Q_1 P + Q_2 P^2 - \sigma = 0 \tag{2.1.12}$$

for s yielding

$$s = -\frac{Q_1}{K}P - \frac{Q_2}{K}P^2 + \frac{\sigma}{K}. \tag{2.1.13}$$

We note that if $P = 0$ we arrive at Hooke's law. We can plug Eq. 2.1.13 into Eq. 2.1.11 and combine with Eq. 2.1.8 to arrive, after some algebra, at

$$F = \frac{1}{2}\big(A - \frac{Q_1^2}{K}\big)P^2 - \frac{Q_1 Q_2}{K}P^3 + \frac{1}{4}(B - \frac{Q_2^2}{K}\big)P^4 - EP + \frac{\sigma^2}{2K}. \tag{2.1.14}$$

After relabeling, we obtain

$$F = \frac{1}{2}A'P^2 + \frac{1}{4}B'P^4 - CP^3 - EP \tag{2.1.15}$$

allowing us to discuss the free energy of the piezoelectric strictly in terms of only the polarization.

2.1.3 Landau-Ginzburg-Devonshire Theory

We begin by generalizing the order parameter η from a scalar to a scalar field $\eta(\mathbf{r})$.[18] Hence we can begin talking about spatial variation of the order parameter, such as its gradient $\nabla\eta$. Making use of Eq. 2.1.8 and following the same symmetry arguments as before, as well as, only keeping the lowest order terms we arrive at

$$F = \int \left[\frac{1}{2}AP^2(\mathbf{r}) + \frac{1}{2}C|\nabla P(\mathbf{r})|^2\right] d\mathbf{r} \tag{2.1.16}$$

where now $P(\mathbf{r})$ is the polarization density.[5] We can convert the gradient operation to multiplication by a Fourier transform

$$P(\mathbf{r}) = \int P(\mathbf{k}) e^{i\mathbf{k}\cdot\mathbf{r}} d\mathbf{k} \tag{2.1.17}$$

and, using Plancherel's theorem, arrive at

$$F = \int \frac{1}{2}\big(A + k^2C\big)|P(\mathbf{k})|^2 d\mathbf{k}. \tag{2.1.18}$$

We now return to the derivation of the fluctuation of the order parameter in the framework of the polarization density. First, by making use of the equipartition theorem for quadratic degrees of freedom[5] and Eq. 2.1.18 we can write

$$|P(\mathbf{k})|^2 = \frac{2k_BT}{A + k^2C} \tag{2.1.19}$$

where k_B is the Boltzmann constant. Then, defining the square of the fluctuation in P as

$$g(\mathbf{r}) \equiv \big(\delta P(\mathbf{r})\big)^2 = \langle P(\mathbf{r})P(\mathbf{0})\rangle - \langle P(\mathbf{0})\rangle^2 \tag{2.1.20}$$

which is also known as the two-site correlation function. Since we are interested in fluctuations near the phase transition, we can set $\langle P(\mathbf{0})\rangle = 0$ because of the paraelectric phase. Then, making use of Fourier transform again, we obtain

$$\big(\delta P(\mathbf{k})\big)^2 = \langle |P(\mathbf{k})|^2\rangle. \tag{2.1.21}$$

Inserting Eq. 2.1.21 into Eq. 2.1.19, we arrive at

$$\big(\delta P(\mathbf{k})\big)^2 = \frac{2k_BT}{A + k^2C} \tag{2.1.22}$$

and taking the inverse Fourier transform yields

$$\big(\delta P(\mathbf{r})\big)^2 = \frac{k_BT}{2\pi C}\frac{e^{-\mathbf{r}/\xi}}{\mathbf{r}} \quad A \neq 0 \tag{2.1.23a}$$

$$\big(\delta P(\mathbf{r})\big)^2 = \frac{k_BT}{2\pi C}\frac{1}{\mathbf{r}} \quad A = 0 \tag{2.1.23b}$$

where $\xi = \sqrt{C/A}$ is known as the correlation length. Physically, ξ corresponds to the length scale which the polarization exists and we note that it is temperature dependent.[5]

Equipped with our knowledge of correlations, we can now attempt to evaluate the Ginzburg criterion. Assuming the general behavior for A, we redefine

$$\xi = \sqrt{\frac{C}{A}} = \sqrt{\frac{C}{A_0(T - T_c)}} = \sqrt{\frac{C}{A_0T_c}}\sqrt{\frac{T_c}{|T - T_c|}} = \xi_0|t|^{-1/2} \tag{2.1.24}$$

where

$$\xi_0 = \sqrt{\frac{C}{A_0T_c}} \tag{2.1.25}$$

and

$$t = \frac{T - T_c}{T_c} \tag{2.1.26}$$

is the correlation length scale and the reduced temperature, respectively. First, to determine $(\delta P)^2$, near the phase transition, we assume $|\mathbf{r}| \sim \xi$ because that is the region where $P \neq 0$ and use Eq. 2.1.23b which yields

$$(\delta P)^2 = \frac{k_B T_c}{2\pi C}\frac{1}{\xi} \sim \xi_0^{-3}|t|^{1/2} \tag{2.1.27}$$

where we have used $C \sim \xi_0^2$. Likewise, using Eq. 2.1.10 we find

$$P^2 = \frac{A_0(T_c - T)}{B} \sim |t|. \tag{2.1.28}$$

Finally, evaluating Eq. 2.1.7 we derive the Levanyuk-Ginzburg criterion

$$\frac{1}{\xi_0^6} \ll |t| \tag{2.1.29}$$

whose validity, near the transition temperature, is strongly dependent on the correlation length scale.

2.2 Applications

Mean field theories have a number of applications such as predicting the behavior of physical quantities near critical points of the system, like the change in the resistance or polarization due to a phase transition. It turns out for ferroelectrics that the correlation length is quite large, which allows the modeling of polarization (the order parameter in question) a good deal away from the transition temperature. This becomes useful for materials that after synthesis are meant to stay in the same phase. Since the materials that we care about are ferroelectric superlattices, this section will be devoted to studying their properties from a mean field approach, however the work can be generalized to any layered structure with arbitrary order parameters.

2.2.1 Layered structures

The main aspect of a layered structure is that it is composed of unit cells designated either for the bulk of the materials or the interfaces. We assume that we have two alternating materials, however it can be easily generalized to more, as shown in Fig. 4 for a single bilayer. We observe that we have two bulk regions and three interface regions in this setup and note

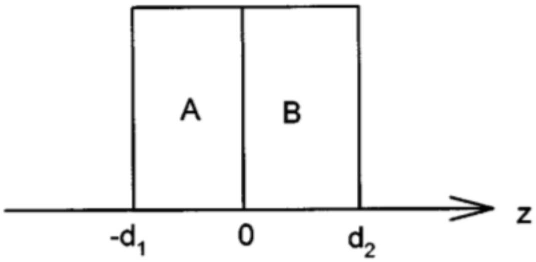

Figure 4: Schematic diagram of a bicolor ferroelectric superlattice grown along the z direction. Taken from Ref. [3]

that both material A and B need not be ferroelectrics, but at least one does. Concerning ourselves with only the planar averaged out of plane polarization $1/S \int P_z(x,y,z)dxdy \equiv P(z)$ we can use the Landau-Ginzburg-Devonshire (LGD) theory[3] to write

$$\begin{aligned} F_{\mathcal{A}} = & \int_{-d_1}^{0} \left[\frac{1}{2}A_1P_1^2 + \frac{1}{4}B_1P_1^4 + \frac{1}{6}C_1P_1^6 + \frac{1}{2}D_1\Big(\frac{\partial P_1}{\partial z}\Big)^2\right]dz \\ & + \frac{D_1}{2\delta_{11}}\Big[P_1(0)^2 + P_1(-d_1)^2\Big] + \frac{D_1^2}{2\delta_{12}}\Big[P_1(0)^4 + P_1(-d_1)^4\Big] \end{aligned} \tag{2.2.1a}$$

$$\begin{aligned} F_{\mathcal{B}} = & \int_{0}^{d_2} \left[\frac{1}{2}A_2P_2^2 + \frac{1}{4}B_2P_2^4 + \frac{1}{6}C_2P_2^6 + \frac{1}{2}D_2\Big(\frac{\partial P_2}{\partial z}\Big)^2\right]dz \\ & + \frac{D_2}{2\delta_{21}}\Big[P_2(0)^2 + P_2(d_2)^2\Big] + \frac{D_2^2}{2\delta_{22}}\Big[P_2(0)^4 + P_2(d_2)^4\Big] \end{aligned} \tag{2.2.1b}$$

$$\begin{aligned} F_{\mathcal{I}} = & -\xi\Big[P_1(0)P_2(0) + P_1(-d_1)P_2(d_2)\Big] \\ & -\eta_1\Big[P_1(0)^3P_2(0) + P_1(-d_1)^3P_2(d_2)\Big] \\ & -\eta_2\Big[P_1(0)P_2(0)^3 + P_1(-d_1)P_2(d_2)^3\Big] \end{aligned} \tag{2.2.1c}$$

where $F_{\mathcal{A}}$, $F_{\mathcal{B}}$ and $F_{\mathcal{I}}$ is the free energy of material A, the free energy of material B and the free energy of the interfaces, respectively. The constants A, B, C, D, δ, ξ and η are in principle known *a priori* through experiments, DFT calculations or intuition. The terms in Eq. 2.2.1c are produced by assuming only nearest neighbor coupling of adjacent unit cells at the interfaces. We note that the last two terms in Eq. 2.2.1a and Eq. 2.2.1b can be associated with the paraelectric order of the material.[20] Next we minimize the total free energy $F_{\mathcal{A}} + F_{\mathcal{B}} + F_{\mathcal{I}}$ with respect to P_1 and P_2 and obtain the following Euler-Lagrange equations

$$D_1 \frac{d^2 P_1}{dz^2} - A_1 P_1 - B_1 P_1^3 - C_1 P_1^5 = 0 \tag{2.2.2a}$$

$$D_2 \frac{d^2 P_2}{dz^2} - A_2 P_2 - B_2 P_2^3 - C_2 P_2^5 = 0 \tag{2.2.2b}$$

with the corresponding Robin boundary conditions

$$\begin{aligned} -D_1 \frac{dP_1}{dz}\bigg|_{z=-d_1} &+ \frac{D_1}{\delta_{11}} P_1(-d_1) + \frac{2D_1^2}{\delta_{12}} P_1(-d_1)^3 - \xi P_2(d_2) \\ &- 3\eta_1 P_1(-d_1)^2 P_2(d_2) - \eta_2 P_2(d_2)^3 = 0 \end{aligned} \tag{2.2.3a}$$

$$\begin{aligned} D_1 \frac{dP_1}{dz}\bigg|_{z=0} &+ \frac{D_1}{\delta_{11}} P_1(0) + \frac{2D_1^2}{\delta_{12}} P_1(0)^3 - \xi P_2(0) \\ &- 3\eta_1 P_1(0)^2 P_2(0) - \eta_2 P_2(0)^3 = 0 \end{aligned} \tag{2.2.3b}$$

$$\begin{aligned} -D_2 \frac{dP_2}{dz}\bigg|_{z=0} &+ \frac{D_2}{\delta_{21}} P_2(0) + \frac{2D_2^2}{\delta_{22}} P_2(0)^3 - \xi P_1(0) \\ &- 3\eta_2 P_2(0)^2 P_1(0) - \eta_1 P_1(0)^3 = 0 \end{aligned} \tag{2.2.3c}$$

$$\begin{aligned} D_2 \frac{dP_2}{dz}\bigg|_{z=d_2} &+ \frac{D_2}{\delta_{21}} P_2(d_2) + \frac{2D_2^2}{\delta_{22}} P_2(d_2)^3 - \xi P_1(-d_1) \\ &- 3\eta_2 P_2(d_2)^2 P_1(-d_1) - \eta_1 P_1(-d_1)^3 = 0. \end{aligned} \tag{2.2.3d}$$

Solving Eq. 2.2.2a and Eq. 2.2.2b is a challenge even numerically because we are dealing with non-linear coupled differential equations. One technique to solve these equations with their boundary conditions is to rewrite the equations using finite differences and build the corresponding matrix associated with the mesh used. Then, solving for the eigenvectors of that matrix, iteratively using Broyden's method,[21] yields the polarization profiles. While instabilities do arise from this numerical technique, they can be avoided by appropriately adjusting the constants (A, B, etc.) at the start of the relaxation. Finally, varying d_1 and d_2 we are able to create polarization profiles for different bilayer thicknesses of interest.

3 Modern Theory of Polarization

3.1 Failures of classical theory

Polarization is a quintessential descriptor of a dielectric material. However, calculating polarization in an infinite solid becomes problematic when extending its definition from isolated systems. Naively, we can calculate the polarization to be

$$\mathbf{P} = \frac{1}{\Omega}\int_{\Omega} \mathbf{r}\rho(\mathbf{r})d\mathbf{r} \tag{3.1.1}$$

where Ω is the volume of the primitive unit cell. To see why there is an explicit dependence of the polarization on the choice of the primitive unit cell, consider the following 1D example

$$\rho(x) = \rho\sin(\frac{2\pi}{L}x) \tag{3.1.2}$$

and

$$P = \frac{1}{L}\int_{a}^{L+a} x\rho\sin(\frac{2\pi}{L}x)dx \tag{3.1.3}$$

where a and L is a rigid shift of the primitive unit cell and the length of the primitive unit cell, respectively. This yields

$$P \equiv P(a) = -\frac{\rho L}{2\pi}\cos(\frac{2\pi}{L}a) \tag{3.1.4}$$

for the polarization which has explicit dependence on the definition of our primitive unit cell and can take any value.

We can reconcile the ill-defined polarization by taking a page from the experimentalists who define it not by absolute values but by its change, or derivatives. Mathematically, we can write it in the following way[22]

$$\Delta\mathbf{P} = \frac{1}{\Omega}\int\int_{\Omega} \mathbf{j}(\mathbf{r},t)d\mathbf{r}dt = \int \mathbf{J}(t)dt \tag{3.1.5}$$

where $\mathbf{j}(\mathbf{r},t)$ is the current induced when switching the polarization of the material. Clearly the polarization does not only dependent on the final measurement, but on the path taken, which means

$$\Delta\mathbf{P} = \int_{0}^{\Delta t} \mathbf{J}(t)dt = \int_{0}^{\Delta t} \frac{d\mathbf{P}}{dt}dt = \mathbf{P}(\Delta t) - \mathbf{P}(0) \tag{3.1.6}$$

where, in the adiabatic limit, $\mathbf{J}(t)$ decays to 0 as $\Delta t \to \infty$. In a more theoretical framework we can generalize Eq. 7.3.13 in the following way

$$\Delta \mathbf{P} = \int_0^1 \frac{d\mathbf{P}}{d\lambda} d\lambda \tag{3.1.7}$$

where λ is a scaled adiabatic parameter.[23] The adiabaticity of the polarization switching is essential since it means that quantum numbers are preserved when λ is varied,[24] which will be important when calculating polarization. We make a few observations about Eq. 3.1.7. First, a centrosymmetric configuration does not imply that $\mathbf{P} = 0$. Therefore when calculating $\Delta\mathbf{P}$ of some arbitrary configuration it is very convenient to take $\mathbf{P}(0)$ to be a centrosymmetric configuration, so that Eq. 3.1.7 yields the spontaneous polarization. Second, there must exist a path between $\mathbf{P}(1)$ and $\mathbf{P}(0)$ which is insulating, or otherwise the flow of charge is ambiguous. Later we will show how we can lift this restriction. Finally, we just need a method of calculating $d\mathbf{P}/d\lambda$ to evaluate Eq. 3.1.7.

3.2 Berry phase formalism

The Berry phase theory[25] to calculate polarization is given such a name because the polarization is expressed in terms of a quantum phase. The derivation begins by assuming that we have an infinite solid that can be represented by a primitive cell with periodic boundary conditions and no electric field. Working in the Bloch basis $|\psi_{n\mathbf{k}}\rangle = e^{i\mathbf{k}\cdot\mathbf{r}}|u_{n\mathbf{k}}\rangle$ the Hamiltonian which satisfies $H^0_{\mathbf{k}}|u_{n\mathbf{k}}\rangle = E_{n\mathbf{k}}|u_{n\mathbf{k}}\rangle$ is

$$H^0_{\mathbf{k}}(\lambda) = \frac{(\mathbf{p}(\lambda) + \mathbf{k}(\lambda))^2}{2m} + V(\mathbf{k}, \lambda) \tag{3.2.1}$$

where λ is some parameter such as strain, sublattice displacement, etc. which has an implicit time dependence. Before continuing, it is fruitful to diagonalize the Hamiltonian through a unitary transformation $U(\lambda)$ so that

$$\tilde{H}(\lambda) = U^\dagger(\lambda) H(\lambda) U(\lambda) \tag{3.2.2}$$

with the transformed eigenstate

$$|\tilde{\psi}(\lambda)\rangle = U^\dagger(\lambda)|\psi(\lambda)\rangle. \tag{3.2.3}$$

The new Scrödinger equation becomes

$$\begin{aligned}i\frac{d}{dt}|\tilde{\psi}\rangle &= i\frac{d}{dt}(U^\dagger|\psi\rangle) = i\frac{dU^\dagger}{dt}|\psi\rangle + iU^\dagger\frac{d}{dt}|\psi\rangle = i\frac{d\lambda}{dt}\frac{\partial U^\dagger}{\partial\lambda}|\psi\rangle + U^\dagger H|\psi\rangle\\ &= \dot{\lambda}i\frac{\partial U^\dagger}{\partial\lambda}U|\tilde{\psi}\rangle + U^\dagger HU|\tilde{\psi}\rangle = (\tilde{H} - \dot{\lambda}\tilde{A}_\lambda)|\tilde{\psi}\rangle\end{aligned} \tag{3.2.4}$$

where we have suppressed the λ dependence for brevity. Here $\tilde{A}_\lambda = -iU^\dagger\partial_\lambda U$ is called the adiabatic guage potential[26] and it is responsible for the transitions between energy levels. Dropping the tildes since we can preform an inverse unitary transformation, we can write the full Hamiltonian as

$$H_{\mathbf{k}}(\lambda) = H^0_{\mathbf{k}}(\lambda) - \dot{\lambda}A_\lambda. \tag{3.2.5}$$

If λ is adiabatic then the wave function to first order is

$$\begin{aligned}|\Psi_{n\mathbf{k}}(t)\rangle &= c_n|u_{n\mathbf{k}}\rangle - \dot{\lambda}\sum_{m\neq n}\frac{\langle u_{m\mathbf{k}}|A_\lambda|u_{n\mathbf{k}}\rangle}{E_{n\mathbf{k}} - E_{m\mathbf{k}}}|u_{m\mathbf{k}}\rangle\\ &= c_n|u_{n\mathbf{k}}\rangle + i\dot{\lambda}\sum_{m\neq n}\frac{\langle u_{m\mathbf{k}}|\partial_\lambda|u_{n\mathbf{k}}\rangle}{E_{n\mathbf{k}} - E_{m\mathbf{k}}}|u_{m\mathbf{k}}\rangle \equiv |0\rangle + |1\rangle\end{aligned} \tag{3.2.6}$$

where

$$|c_n|^2 = 1 - \dot{\lambda}^2\sum_{m\neq n}\frac{|\langle u_{m\mathbf{k}}|\partial_\lambda|u_{n\mathbf{k}}\rangle|^2}{(E_{n\mathbf{k}} - E_{m\mathbf{k}})^2} = 1 + \mathcal{O}(\dot{\lambda}^2) \tag{3.2.7}$$

from the normalization condition. To calculate the rate of change of the polarization, we try extend the classical definition of the dipole moment into the quantum one[23] such that

$$\frac{d\mathbf{P}}{dt} = e\frac{d\mathbf{r}}{dt} \Rightarrow \frac{e}{\Omega}\int\frac{d}{dt}\langle\mathbf{r}\rangle d\mathbf{r} = -\frac{ie}{\Omega}\int\langle[\mathbf{r}, H_{\mathbf{k}}]\rangle d\mathbf{r} = \frac{e}{m}\int\langle\mathbf{p} + \mathbf{k}\rangle\frac{d\mathbf{k}}{(2\pi)^3} \tag{3.2.8}$$

where we have made use of Ehrenfest's theorem and transforming to reciprocal space. Now inserting Eq. 3.2.6 into Eq. 3.2.8 yields

$$\frac{d\mathbf{P}_n}{dt} = \frac{e}{m}\int_{\Omega_{BZ}}\big(\langle 0|\mathbf{p} + \mathbf{k}|0\rangle + \langle 1|\mathbf{p} + \mathbf{k}|0\rangle + \langle 0|\mathbf{p} + \mathbf{k}|1\rangle + \langle 1|\mathbf{p} + \mathbf{k}|1\rangle\big)\frac{d\mathbf{k}}{(2\pi)^3} \tag{3.2.9}$$

where the n index is present because we are calculate the polarization for $|\Psi_{n\mathbf{k}}(t)\rangle$.

We can simplify Eq. 3.2.9 by noting that when $\mathbf{p}+\mathbf{k}$ acts on an eigenstate it changes it to a different eigenstate and therefore $\langle 0|\mathbf{p}+\mathbf{k}|0\rangle$ is 0 due to the orthogonality condition. Next, we drop any terms with $\mathcal{O}(\dot{\lambda}^2)$ or higher since we are working with only the first order corrections. Finally, note that due to $\dot{\lambda}$ we have dt on both sides of the equation that we can cancel out which yields

$$\frac{d\mathbf{P}_n}{d\lambda} = \frac{ie}{(2\pi)^3 m} \sum_{m\neq n} \int_{\Omega_{BZ}} \frac{\langle u_{n\mathbf{k}}|\mathbf{p}+\mathbf{k}|u_{m\mathbf{k}}\rangle\langle u_{m\mathbf{k}}|\partial_\lambda|u_{n\mathbf{k}}\rangle}{E_{n\mathbf{k}}-E_{m\mathbf{k}}} d\mathbf{k} + \text{c.c.} \tag{3.2.10}$$

where c.c is the complex conjugate. We can further simplify Eq. 3.2.10 by noting the following property[27] of $|u_{n\mathbf{k}}\rangle$

$$\nabla_{\mathbf{k}}|u_{n\mathbf{k}}\rangle = \frac{1}{m}\sum_{m\neq n} |u_{m\mathbf{k}}\rangle\langle u_{m\mathbf{k}}|\frac{\mathbf{p}+\mathbf{k}}{E_{n\mathbf{k}}-E_{m\mathbf{k}}}|u_{n\mathbf{k}}\rangle + ig(\mathbf{k})|u_{n\mathbf{k}}\rangle \tag{3.2.11}$$

where g is an arbitrary function, not dependent on λ. This allows us to rewrite Eq. 3.2.10 as

$$\frac{d\mathbf{P}_n}{d\lambda} = \frac{ie}{(2\pi)^3}\int_{\Omega_{BZ}} \langle \nabla_{\mathbf{k}} u_{n\mathbf{k}}|\partial_\lambda u_{n\mathbf{k}}\rangle d\mathbf{k} + \text{c.c.} + G_{nm}(\mathbf{k}) \tag{3.2.12}$$

where

$$G_{nm}(\mathbf{k}) = \frac{e}{(2\pi)^3}\int_{\Omega_{BZ}} \langle u_{n\mathbf{k}}|g(\mathbf{k})|u_{m\mathbf{k}}\rangle d\mathbf{k}. \tag{3.2.13}$$

Performing the integration over λ the last term results in

$$\frac{e}{(2\pi)^3}\int_{\Omega_{BZ}} \Big[\langle u_{n\mathbf{k}}(1)|g(\mathbf{k})|u_{m\mathbf{k}}(1)\rangle - \langle u_{n\mathbf{k}}(0)|g(\mathbf{k})|u_{m\mathbf{k}}(0)\rangle\Big] d\mathbf{k} \tag{3.2.14}$$

which is equal to zero, under the assumption that $V(\mathbf{k},0) = V(\mathbf{k},1)$ and therefore $|u_{n\mathbf{k}}(0)\rangle = |u_{n\mathbf{k}}(1)\rangle$. For the first two terms, after integration by parts, we find

$$\begin{aligned}\mathbf{P}_n &= \frac{ie}{(2\pi)^3}\int_{\Omega_{BZ}} \left[\langle u_{n\mathbf{k}}(\lambda)|\nabla_{\mathbf{k}}|u_{n\mathbf{k}}(\lambda)\rangle\Big|_0^1 - \int_0^1 \nabla_{\mathbf{k}}\langle u_{n\mathbf{k}}(\lambda)|\partial_\lambda|u_{n\mathbf{k}}(\lambda)\rangle d\lambda\right] d\mathbf{k} \\ &= \frac{ie}{(2\pi)^3}\left[\int_{\Omega_{BZ}} \langle u_{n\mathbf{k}}(\lambda)|\nabla_{\mathbf{k}}|u_{n\mathbf{k}}(\lambda)\rangle\Big|_0^1 d\mathbf{k} - \int_0^1 \langle u_{n\mathbf{k}}(\lambda)|\partial_\lambda|u_{n\mathbf{k}}(\lambda)\rangle\Big|_{\partial\Omega_{BZ}} d\lambda\right]\end{aligned} \tag{3.2.15}$$

where the last term yields zero because $\partial_\lambda|u_{n\mathbf{k}}(\lambda)\rangle$ is also periodic in the Brillouin zone. Finally summing over n we can write the total contribution of the electronic polarization to be

$$\mathbf{P}_{el}(\lambda) = \frac{e}{(2\pi)^3}\Im\sum_n \int_{\Omega_{BZ}} \langle u_{n\mathbf{k}}(\lambda)|\nabla_{\mathbf{k}}|u_{n\mathbf{k}}(\lambda)\rangle d\mathbf{k} \tag{3.2.16}$$

where $\mathbf{P}_{el}$ is to be evaluated at different λ. To obtain the total polarization, we add the ionic contribution which results in

$$\mathbf{P} = \frac{e}{(2\pi)^3}\Im\sum_n \int_{\Omega_{BZ}} \langle u_{n\mathbf{k}}(\lambda)|\nabla_{\mathbf{k}}|u_{n\mathbf{k}}(\lambda)\rangle d\mathbf{k} + \frac{e}{\Omega}\sum_I Z_I\mathbf{R}_I \tag{3.2.17}$$

where we note that Z_I should be the bare nuclear charge, although in actual calculations the core electrons should be included since they are not treated explicitly.

We conclude this section by noting that the polarization is a gauge dependent quantity. This can be seen explicitly by going to a different Bloch basis through a unitary transformation

$$|\tilde{u}_{n\mathbf{k}}\rangle = e^{i\theta_n(\mathbf{k})}|u_{n\mathbf{k}}\rangle \tag{3.2.18}$$

then the polarization becomes

$$\tilde{\mathbf{P}} = \mathbf{P} + \frac{e}{(2\pi)^3}\sum_n \int \nabla_{\mathbf{k}}\theta_n(\mathbf{k})d\mathbf{k}. \tag{3.2.19}$$

We can simplify the above equation by the physical restriction that $\theta_n(\mathbf{k})$ should be periodic in the Brillouin zone. Then without loss of generality[25] we can write

$$\theta_n(\mathbf{k}) = \beta_n(\mathbf{k}) + \mathbf{k}\cdot\mathbf{R}_n \tag{3.2.20}$$

where $\beta_n(\mathbf{k})$ is periodic in the Brillouin zone and $\mathbf{R}_n$ is a lattice vector. Finally, inserting Eq. 3.2.20 into Eq. 3.2.19 yields

$$\tilde{\mathbf{P}} = \mathbf{P} + \frac{e}{(2\pi)^3}\sum_n \beta_n(\mathbf{k})\Big|_{\partial\Omega_{BZ}} + e\sum_n \mathbf{R}_n \int \frac{d\mathbf{k}}{(2\pi)^3} \tag{3.2.21}$$

Since $\beta_n(\mathbf{k})$ is periodic, evaluating the limits at the boundary is zero and therefore we are left with

$$\tilde{\mathbf{P}} = \mathbf{P} + \frac{e}{\Omega}\sum_n \mathbf{R}_n \equiv \mathbf{P} + \frac{e}{\Omega}\mathbf{R} \tag{3.2.22}$$

where the polarization is only defined modulo the lattice vector $\mathbf{R}$.

3.3 Wannier formalism

Recasting the modern theory of polarization in the Wannier representation is beneficial from a conceptual point of view. As we will show, we can think of polarization as changes in the positions of electronic "molecular" orbitals allowing for easier visualization than working in reciprocal space. We begin with the realization that using the atomic orbitals in crystals as a basis is problematic because although they have translation symmetry, they are, in general, not orthogonal.[28] In other words

$$\int_\Omega \psi(\mathbf{r}-\mathbf{R})\psi^*(\mathbf{r}-\mathbf{R}')d\mathbf{r} \neq \delta_{\mathbf{R}\mathbf{R}'} \tag{3.3.1}$$

where Ω, ψ, and $\mathbf{R}$ is the volume of primitive cell, the atomic orbital and lattice vector, respectively. To circumvent this problem we make the following pseudo-Fourier transformation (Bloch sum)

$$\phi_{\mathbf{k}}(\mathbf{r}) = C(\mathbf{k})\sum_{\mathbf{R}} e^{i\mathbf{k}\cdot\mathbf{R}}\psi(\mathbf{r}-\mathbf{R}) \tag{3.3.2}$$

where $C(\mathbf{k})$ is a normalization constant. Now we show that $\phi_{\mathbf{k}}$ are orthonormal by

$$\int_\Omega \phi_{\mathbf{k}}(\mathbf{r})\phi^*_{\mathbf{k}'}(\mathbf{r})d\mathbf{r} = C(\mathbf{k})C^*(\mathbf{k}')\sum_{\mathbf{R}\mathbf{R}'} e^{i(\mathbf{k}\cdot\mathbf{R}-\mathbf{k}'\cdot\mathbf{R}')}\int_\Omega \psi(\mathbf{r}-\mathbf{R})\psi^*(\mathbf{r}-\mathbf{R}')d\mathbf{r} \tag{3.3.3}$$

where we can simplify the above expression by multiplying and dividing by $e^{i\mathbf{k}\cdot\mathbf{R}'}$ to yield

$$\begin{aligned}\langle\phi_{\mathbf{k}}|\phi_{\mathbf{k}'}\rangle &= C(\mathbf{k})C^*(\mathbf{k}')\sum_{\mathbf{R}\mathbf{R}'} e^{i\mathbf{k}\cdot(\mathbf{R}-\mathbf{R}')}e^{i(\mathbf{k}-\mathbf{k}')\cdot\mathbf{R}'}\int_\Omega \psi(\mathbf{r}-\mathbf{R})\psi^*(\mathbf{r}-\mathbf{R}')d\mathbf{r}\\ &= \delta_{\mathbf{k}\mathbf{k}'}C(\mathbf{k})C^*(\mathbf{k}')\sum_{\mathbf{R}''} e^{i\mathbf{k}\cdot\mathbf{R}''}\int_\Omega \psi(\mathbf{r})\psi^*(\mathbf{r}-\mathbf{R}'')d\mathbf{r} \equiv \delta_{\mathbf{k}\mathbf{k}'}\end{aligned} \tag{3.3.4}$$

where $\mathbf{R}'' = \mathbf{R}-\mathbf{R}'$ and the equivalence was made by defining the normalization constant as

$$\frac{1}{C^2(\mathbf{k})} = \sum_{\mathbf{R}} e^{i\mathbf{k}\cdot\mathbf{R}}\int_\Omega \psi(\mathbf{r})\psi^*(\mathbf{r}-\mathbf{R})d\mathbf{r}. \tag{3.3.5}$$

Since we have constructed an orthonormal basis we can take the inverse transformation of Eq. 3.3.2 to yield

$$w(\mathbf{r}-\mathbf{R}) \equiv w_{\mathbf{R}}(\mathbf{r}) = \sum_{\mathbf{k}} e^{-i\mathbf{k}\cdot\mathbf{R}}\phi_{\mathbf{k}}(\mathbf{r}) \tag{3.3.6}$$

an orthonormal basis set in real space that has translational symmetry known as Wannier functions. We note that while this is a natural scheme to generate real space orthonormal basis with translational symmetry, it is not unique, a point that we will come back to later.

In practice we usually do not have access to the atomic orbitals in crystals and therefore the Wannier functions are typically defined as

$$w_n(\mathbf{r}-\mathbf{R}) \equiv \langle \mathbf{r}|\mathbf{R}n\rangle = \frac{\Omega}{(2\pi)^3}\int_{\Omega_{BZ}} e^{-i\mathbf{k}\cdot\mathbf{R}}\langle \mathbf{r}|\psi_{n\mathbf{k}}\rangle d\mathbf{k} \tag{3.3.7}$$

where $|\psi_{n\mathbf{k}}\rangle$ is the Bloch wavefunctions, respectively. Likewise the inverse transformation leads to

$$|\psi_{n\mathbf{k}}\rangle = \sum_{\mathbf{R}} e^{i\mathbf{k}\cdot\mathbf{R}}|\mathbf{R}n\rangle \tag{3.3.8}$$

where we have dropped the $\langle \mathbf{r}|$ since it appears on both sides of the equation. We note that since the Bloch functions are completely delocalized, we can think of the Wannier functions as localized orbitals. The connection between Wannier functions and the polarization can be seen by calculating the center of mass of a Wannier function in the home cell ($\mathbf{R}=0$)

$$\langle \mathbf{0}n|\mathbf{r}|\mathbf{0}n\rangle \equiv \langle \mathbf{r}\rangle_n = \left(\frac{\Omega}{(2\pi)^3}\right)^2 \int_{\Omega_{BZ}} \langle \psi_{n\mathbf{k}'}|\mathbf{r}|\psi_{n\mathbf{k}}\rangle d\mathbf{k}d\mathbf{k}' \tag{3.3.9}$$

where we have used Eq. 3.3.7 in recasting the Wannier functions as Bloch functions. We can manipulate Eq. 3.3.9 using the following property[29]

$$\mathbf{r}^{\mu}|\psi_{n\mathbf{k}}\rangle = i\nabla^{\mu}_{\mathbf{k}}|\psi_{n\mathbf{k}}\rangle - i\sum_{n'}\langle u_{n\mathbf{k}}|\nabla^{\mu}_{\mathbf{k}}|u_{n'\mathbf{k}}\rangle|\psi_{n'\mathbf{k}}\rangle \tag{3.3.10}$$

and write

$$\begin{aligned}\langle \mathbf{r}\rangle_n =& \left(\frac{\Omega}{(2\pi)^3}\right)^2 \int_{\Omega_{BZ}} i\Big(\langle \psi_{n\mathbf{k}'}|\nabla_{\mathbf{k}}|\psi_{n\mathbf{k}}\rangle - \sum_{n'}\langle \psi_{n\mathbf{k}'}|\psi_{n'\mathbf{k}}\rangle\langle u_{n\mathbf{k}'}|\nabla_{\mathbf{k}}|u_{n'\mathbf{k}}\rangle\Big)d\mathbf{k}d\mathbf{k}' \\ =& \left(\frac{\Omega}{(2\pi)^3}\right)^2 \int_{\Omega_{BZ}} \frac{1}{2}i\langle \psi_{n\mathbf{k}'}|\psi_{n\mathbf{k}}\rangle\Big|_{\partial\Omega_{BZ}} d\mathbf{k} - i\frac{\Omega}{(2\pi)^3}\int_{\Omega_{BZ}}\langle u_{n\mathbf{k}}|\nabla_{\mathbf{k}}|u_{n\mathbf{k}}\rangle d\mathbf{k}\end{aligned} \tag{3.3.11}$$

where we have used integration by parts for the first term and $\langle \psi_{n\mathbf{k}'} | \psi_{n'\mathbf{k}} \rangle = \delta_{nn'}\delta_{\mathbf{k}\mathbf{k}'}$ for the second term. We can simplify Eq. 3.3.11 by noting that $|\psi_{n\mathbf{k}}\rangle$ are periodic in the BZ, and therefore the first term is zero because we are evaluating at the boundary, which yields

$$\langle \mathbf{r} \rangle_n = -i\frac{\Omega}{(2\pi)^3}\int_{\Omega_{BZ}} \langle u_{n\mathbf{k}} | \nabla_{\mathbf{k}} | u_{n\mathbf{k}} \rangle d\mathbf{k}. \tag{3.3.12}$$

Comparing our previous result for the electric polarization we observe that we can write the total polarization as

$$\mathbf{P} = \frac{e}{\Omega}\sum_n \langle \mathbf{r} \rangle_n + \frac{e}{\Omega}\sum_I Z_I \mathbf{R}_I \tag{3.3.13}$$

which we note again is defined modulo $e\mathbf{R}/\Omega$.

While we have defined the polarization in terms of the Wannier centers, we have not given as scheme as to which gauge we should be working in. This is answered by considering the gauge where the Wannier functions are maximally localized, which means that the Wannier functions are real and exponentially decaying in real space.[30] Therefore, in this gauge we can think of the Wannier functions as electronic molecular orbitals of the crystal. Mathematically, these Wannier functions are constructed by minimizing the spread

$$\sum_n \left(\langle r^2 \rangle_n - \langle \mathbf{r} \rangle_n^2 \right) \tag{3.3.14}$$

where

$$\langle \mathbf{0}n | r^2 | \mathbf{0}n \rangle \equiv \langle r^2 \rangle_n = \frac{\Omega}{(2\pi)^3}\int_{\Omega_{BZ}} |\langle u_{n\mathbf{k}} | \nabla_{\mathbf{k}} | u_{n\mathbf{k}} \rangle|^2 d\mathbf{k} \tag{3.3.15}$$

which can be derived in a similar fashion as Eq. 3.3.12. Numerically, the minimization is achieved by beginning with trial wavefunctions which then undergo unitary transformations such that the gradient of the spread is steepest.[30]

4 Computational Methods

4.1 Density Functional Theory

Inhomogeneous electron gas systems are the basis of solid state physics. Tackling the many-body problem to understand these systems would be impossible if we were to treat each electron explicitly. Instead we work with the electron density of the system, which is the focal point of density functional theory (DFT). The method developed by Kohn and Sham[31] involves a set of self consistent equations that are solved iteratively to obtain the ground state. Here we attempt to give a short introduction into the methodology of DFT, as well as, also highlighting the shortcomings of the theory.

4.1.1 Hohenberg-Kohn energy functional

We begin with the general formulation of the many-body electronic Hamiltonian, to describe the inhomogeneous electron gas under an ionic potential, given by Hohenberg and Kohn[32] (HK) which has the following form

$$\hat{H} = \hat{T} + \hat{V} + \hat{U} \tag{4.1.1}$$

where

$$\hat{T} = \frac{1}{2}\int \nabla\psi^*(\mathbf{r})\nabla\psi(\mathbf{r})d\mathbf{r} \tag{4.1.2}$$

$$\hat{V} = \int v(\mathbf{r})\psi^*(\mathbf{r})\psi(\mathbf{r})d\mathbf{r} \tag{4.1.3}$$

$$\hat{U} = \frac{1}{2}\int \frac{1}{|\mathbf{r}-\mathbf{r}'|}\psi^*(\mathbf{r})\psi^*(\mathbf{r}')\psi(\mathbf{r})\psi(\mathbf{r}')d\mathbf{r}d\mathbf{r}' \tag{4.1.4}$$

is the kinetic, potential and interaction (Coulomb) term, respectively. Here $v(\mathbf{r})$ and $\psi(\mathbf{r})$ is the ionic potential, under the Born-Oppenheimer approximation and the second quantized electron field $\langle\mathbf{r}|\psi\rangle$, respectively. Then the electron density is given by

$$n(\mathbf{r}) = \psi^*(\mathbf{r})\psi(\mathbf{r}) \tag{4.1.5}$$

which can easily be shown to be a unique functional of $v(\mathbf{r})$ for a given ground state. Motivated by the idea that we can think of the system as a liquid, represented by a single parameter rather than a collection of abstract wavefunctions, we recast Eq. 4.1.1 in terms of $n(\mathbf{r})$ rather than $\psi(\mathbf{r})$. This is done not without difficulty and the new expression, now a functional of $n(\mathbf{r})$, becomes

$$E_v[n] = \int v(\mathbf{r})n(\mathbf{r})d\mathbf{r} + \frac{1}{2}\int \frac{n(\mathbf{r})n(\mathbf{r}')}{|\mathbf{r}-\mathbf{r}'|}d\mathbf{r}d\mathbf{r}' + G[n] \tag{4.1.6}$$

where $G[n]$ is the kinetic energy of the interacting system. The expression in Eq. 4.1.6 is known as the HK energy functional. We note that due to the nonlocal nature of derivatives, $G[n]$ consists of an exchange and correlation term. We state that Eq. 4.1.6 can always be written in this form for any many-body system and that given the correct $n(\mathbf{r})$ the true ground state can be calculated. The proofs to these two claims arise naturally when considering the formulation using Legendre transformations.[33, 34]

4.1.2 Kohn-Sham equations

A methodology to solving the HK energy functional beyond simple systems is done by extending the approximation that the interacting kinetic energy can be written as a sum of the non-interacting kinetic energy and a correction, as follows

$$G[n] = T[n] + E_{xc}[n] \tag{4.1.7}$$

where the correction, E_{xc}, is known as the exchange-correlation energy. The functional form of E_{xc} is not known for an arbitrary $n(\mathbf{r})$, however we can make another approximation that the density is slow varying such that

$$n(\mathbf{r}) = n_0 + \delta n(\mathbf{r}) \tag{4.1.8}$$

where n_0 and $\delta n(\mathbf{r})$ is the constant and variational electron density, respectively. The variational electron density is therefore subject to two conditions

$$\frac{\delta n(\mathbf{r})}{n_0} \ll 1 \tag{4.1.9a}$$

$$\int \delta n(\mathbf{r})d\mathbf{r} = 0. \tag{4.1.9b}$$

Then it can be shown[32] that

$$E_{xc}[n] = \int n(\mathbf{r})\epsilon_{xc}(n(\mathbf{r}))d\mathbf{r} \tag{4.1.10}$$

where ϵ_{xc} is the exchange-correlation density of a uniform electron gas. In practice, ϵ_{xc} is determined through parametric fitting.[35] We note that Eq. 4.1.10 is known as the local density approximation (LDA).

Now having simplified the HK functional we want to determine the $n(\mathbf{r})$ which produces the ground state energy. This minimization of the energy functional is nothing more than solving the Euler-Lagrange equation[36] as follows

$$\frac{\delta E[n]}{\delta n} = \frac{\partial}{\partial n}\left[v_{ion}(\mathbf{r})n(\mathbf{r}) + \frac{1}{2}\int \frac{n(\mathbf{r})n(\mathbf{r}')}{|\mathbf{r}-\mathbf{r}'|}d\mathbf{r}' + n(\mathbf{r})\epsilon_{xc}(n(\mathbf{r}))\right] + \frac{\delta T[n]}{\delta n} = 0. \tag{4.1.11}$$

Simplifying and relabelling terms we arrive at

$$v_{ion}(\mathbf{r}) + v_H(\mathbf{r}) + v_{xc}(\mathbf{r}) + \frac{\delta T[n]}{\delta n} = 0 \tag{4.1.12}$$

where

$$v_{ion}(\mathbf{r}) = -\sum_I \frac{Z}{|\mathbf{r}-\mathbf{R}_I|} \tag{4.1.13a}$$

$$v_H(\mathbf{r}) = \int \frac{n(\mathbf{r}')}{|\mathbf{r}-\mathbf{r}'|}d\mathbf{r}' \tag{4.1.13b}$$

$$v_{xc}(\mathbf{r}) = \frac{\partial}{\partial n}\left[n(\mathbf{r})\epsilon_{xc}(n(\mathbf{r}))\right] \tag{4.1.13c}$$

is the ionic, Hartree and exchange-correlation potential, respectively. Here Kohn and Sham (KS) made the realization that Eq. 4.1.12 is a system of non-interacting electrons under some effective potential and therefore the easiest way to find $n(\mathbf{r})$ is to solve the following one particle Shrödinger equation

$$\left\{-\frac{1}{2}\nabla^2 + v_{eff}(\mathbf{r})\right\}\psi_i(\mathbf{r}) = \epsilon_i\psi_i(\mathbf{r}) \tag{4.1.14}$$

where

$$v_{eff}(\mathbf{r}) = v_{ion}(\mathbf{r}) + v_H(\mathbf{r}) + v_{xc}(\mathbf{r}) \tag{4.1.15}$$

is the effective potential. This allows us to obtain

$$n(\mathbf{r}) = \sum_i f_i|\psi_i(\mathbf{r})|^2 \tag{4.1.16}$$

where f_i is the fractional occupation, and hence the ground state energy. The Eqs. 4.1.9b, 4.1.14, 4.1.15 and 4.1.16 are known as the KS equations which have to be solved self-consistently.[31] In practice, with a known $v_{ion}(\mathbf{r})$, one makes a guess for $n(\mathbf{r})$ then constructs $v_{eff}(\mathbf{r})$ to produce a new $n(\mathbf{r})$, subject to the constraint of 4.1.9b, by solving Eqs. 4.1.15 and 4.1.16.

4.1.3 Failures of Density Functional Theory

While DFT has proven its usefulness in computational physics, we highlight a few of its failures. We begin by noting that DFT, by construction, is a ground state theory and therefore any conclusions drawn about excitations, such as the band gap of a system, would be erroneous. Accurate calculations of the band gap can achieved using the *GW* approximation[37] which builds upon the DFT formalism. Next, we emphasize that the exact form of ϵ_{xc} is not possible to determine, and therefore any attempts to approximate it are uncontrolled. This is in contrast to controlled approximation techniques, such as the configuration interaction method[38], however they tend to be much more computationally expensive. Furthermore, we note that the conventional local density approximation does not take into account non local long range potentials, such as van der Waals, and therefore would produce the wrong ground state where such potentials are crucial, such as for liquid water.[39] However, techniques exist[40] that allow long range potentials to be incorporated into DFT. We conclude with the fact that DFT is able to calculate the total energies of many-body systems with a high relative, but not necessarily absolute, accuracy.[41]

4.2 SIESTA program

The SIESTA[42] (Spanish Initiative for Electronic Simulation with Thousands of Atoms) electronic structure code has a number of advantages (and disadvantages) over other *ab initio* packages. The main features of the package are a fully self-consistent DFT using a linear combination of atomic orbitals (LCAO) with $\mathcal{O}(N)$ scaling. We will comment on a select few of the important methodologies employed by the package.

4.2.1 Pseudopotentials

Pseudopotentials are a method to decrease computational costs by not explicitly considering the core electrons. In addition, they allow for a smooth charge density on a uniform grid. For general calculations the Troullier-Martins parametrization scheme[43] is used. Under this scheme, the ionic pseudopotentials are constructed by first assuming spherical screening and then solving, self-consistently, the all-electron radial KS Schrödinger equation for the isolated atom

$$\left\{ -\frac{1}{2}\frac{d^2}{dr^2} + \frac{l(l+1)}{2r^2} + v_{scr}^{AE}(r) \right\} rR_{nl}^{AE}(r) = \epsilon_{nl} rR_{nl}^{AE}(r) \tag{4.2.1}$$

where

$$v_{scr}^{AE}(r) = v_{ion}^{AE}(r) + v_{H}^{AE}(r) + v_{xc}^{AE}(r) \tag{4.2.2}$$

and R_{nl}^{AE} is the all-electron screened potential and all-electron wavefunction, respectively.

With the R_{nl}^{AE} we begin to construct the pseudowavefunctions R_{nl}^{PP} by considering four criteria that would increase computational efficiency and accuracy. First to reduce oscillations in the R_{nl}^{PP} we only consider node-free solutions to the radial equation. Second, we can tailor our R_{nl}^{PP} to how much of the core electrons we want to properly capture and therefore R_{nl}^{AE} and R_{nl}^{PP} should be equal below some chosen core radius, r_{nl}^{c}. Third, to improve the property of transferability[44] (how well a psuedopotential can be used from one system to another), R_{nl}^{PP} should satisfy

$$\int_0^{r_{nl}^c} |R_{nl}^{PP}(r)|^2 r^2 dr = \int_0^{r_{nl}^c} |R_{nl}^{AE}(r)|^2 r^2 dr. \tag{4.2.3}$$

Fourth, to further improve transferability, the eigenvalues of R_{nl}^{AE} and R_{nl}^{PP} must all be equal. The pseudopotential that will be generated from the above four criteria is referred to as a norm-conserving pseudopotential.

Now using the constructed R_{nl}^{PP} we solve for $v_{scr}^{PP}(r)$ by inverting Eq. 4.2.1,

$$v_{scr,nl}^{PP}(r) = \epsilon_{nl} - \frac{l(l+1)}{2r^2} + \frac{1}{2rR_{nl}^{PP}(r)}\frac{d^2}{dr^2}\left[rR_{nl}^{PP}(r)\right]. \tag{4.2.4}$$

We note that $v_{scr,l}^{PP}(r)$ has a dependency on the principle and angular quantum number, n and l, respectively. We can now calculate the ionic pseudopotential of interest by rearranging terms as follows

$$v_{ion,nl}^{PP}(r) = v_{scr,nl}^{PP}(r) - v_{H}^{PP}(r) - v_{xc}^{PP}(r) \tag{4.2.5}$$

where $v_H^{PP}(r)$ and $v_{xc}^{PP}(r)$ are calculated from R_{nl}^{PP}. We can further reduce computation time by separating $v_{ion,nl}^{PP}(r)$ into a local and nonlocal (has l dependence) part, where the nonlocal part can be calculated using a procedure developed by Kleinman and Bylander.[45]

4.2.2 Numerical basis set

One way to solve the one particle Schrödinger equation is to decompose the wavefunctions into a linear combination of atomic orbitals as follows

$$\psi_i(\mathbf{r}) = \sum_\alpha c_{\alpha i}\phi_\alpha(\mathbf{r}) \tag{4.2.6}$$

where $\phi_\alpha(\mathbf{r})$ is the α'th atomic orbital. For atom I at position $\mathbf{R}_I$, we can further decompose $\phi_\alpha(\mathbf{r})$ using separation of variables in spherical coordinates

$$\phi_\alpha(\mathbf{r}) = R_{Inl}(r_I)Y_{lm}(\hat{r}_I) \tag{4.2.7}$$

where $r_I = r - \mathbf{R}_I \cdot \hat{r}$. Our goal is to determine a computationally efficient basis set of radial functions.

The method of Sankey and Niklewski[46] to produce such a balanced basis set involves solving

$$\left\{ -\frac{1}{2}\frac{d^2}{dr^2} + \frac{l(l+1)}{2r^2} + v_{ion,Inl}^{PP}(r) \right\} rR_{Inl}(r) = \left(\epsilon_{Inl} + \delta\epsilon_{Inl}\right) rR_{Inl}(r) \tag{4.2.8}$$

Here $\delta\epsilon_{Inl}$ is introduced because, in practice, we want to truncate the radial functions after some cut-off radius r_{Inl}^{cut} to zero. This is achieved by fixing $\delta\epsilon_{Inl}$ such that R_{Inl} vanishes at the first node, located at r_{Inl}^{cut}, hence $R_{Inl}(r_{Inl}^{\text{cut}}) = 0$. Since the radial dependence, for a given l, is represented by only one function (just R_{Inl}), this is referred to as a single-ζ basis. Multiple-ζ bases can be constructed by different schemes, of which SIESTA uses the split-valence method.[47] The formalism outlined in this section allows us to produce numerical orbitals $\phi_\alpha(\mathbf{r})$ with different ζ bases, for efficient calculations, in contrast to, expressing the orbitals using plane waves, such as LAPW.[48]

4.2.3 Real and reciprocal space integrals

As previously stated we expand the one-particle wavefunctions $\psi_i(\mathbf{r})$ in terms of basis of atomic orbitals $\phi_\alpha(\mathbf{r})$ therefore we can write the electron density as

$$n(\mathbf{r}) = \sum_i f_i \psi_i^*(\mathbf{r})\psi_i(\mathbf{r}) = \sum_i f_i \sum_\alpha c_{\alpha i}^* \phi_\alpha^*(\mathbf{r}) \sum_\beta c_{\beta i}\phi_\beta(\mathbf{r}) \tag{4.2.9}$$

then rearranging and relabeling terms we arrive at

$$n(\mathbf{r}) = \sum_{\alpha\beta} \rho_{\alpha\beta}\phi_\alpha^*(\mathbf{r})\phi_\beta(\mathbf{r}) \tag{4.2.10}$$

where

$$\rho_{\alpha\beta} = \sum_i f_i c_{\alpha i}^* c_{\beta i} \tag{4.2.11}$$

is the density matrix. We observe that after $\rho_{\alpha\beta}$ is calculated once we only need a few atomic orbitals to calculate the density at a given grid point, allowing for $\mathcal{O}(N)$ scaling. For calculating the Hamiltonian (KS energy functional) matrix in the atomic orbital basis, we can write

$$\langle\psi|H|\psi\rangle = \sum_{\alpha\beta} \rho_{\alpha\beta} H_{\alpha\beta} \tag{4.2.12}$$

therefore,

$$H_{\alpha\beta} = \int \phi_\alpha^*(\mathbf{r})H(\mathbf{r})\phi_\beta(\mathbf{r})d\mathbf{r}. \tag{4.2.13}$$

We note that, by convention, the grid fineness is determined by E_{cut}, the maximum kinetic energy of the plane waves that could be represented in the grid without superposition.[49]

While simulations in real space are appropriate for isolated or large systems, simulating a crystalline solid with a unit cell requires one to take advantage of reciprocal space to naturally account for the periodicity of the system. We can perform a Bloch-state expansions of the one-particle wavefunctions

$$\psi_i(\mathbf{r},\mathbf{k}) = \sum_{\alpha'} c_{\alpha' i}(\mathbf{k})\phi_{\alpha'}(\mathbf{k})e^{i\mathbf{k}\cdot\mathbf{R}_{\alpha'}} \tag{4.2.14}$$

where $\mathbf{R}_\alpha$ is the vector to the α'th unit cell and the primed index runs over all atomic orbitals in the auxiliary supercell (collection of neighbouring unit cells). This allows us to obtain the electron density by

$$n(\mathbf{r}) = \sum_i f_i(\mathbf{k})\psi_i^*(\mathbf{r},\mathbf{k})\psi_i(\mathbf{r},\mathbf{k}) = \sum_{\alpha'\beta'} \rho_{\alpha'\beta'}\phi_{\alpha'}^*(\mathbf{r})\phi_{\beta'}(\mathbf{r}) \tag{4.2.15}$$

where

$$\rho_{\alpha'\beta'} = \sum_i \int_{\Omega_{BZ}} f_i(\mathbf{k}) c^*_{\alpha' i}(\mathbf{k}) c_{\beta' i}(\mathbf{k}) e^{i\mathbf{k}\cdot(\mathbf{R}_{\beta'}-\mathbf{R}_{\alpha'})} \tag{4.2.16}$$

is the density matrix. We note, due to the system being periodic, $\rho_{\alpha'\beta'} = \rho_{\alpha\beta}$. Likewise, we can extend Eq. 4.2.13 to neighbouring cells by

$$H_{\alpha\beta}(\mathbf{k}) = \sum_{\beta'} H_{\alpha\beta} e^{i\mathbf{k}\cdot(\mathbf{R}_{\beta'}-\mathbf{R}_{\alpha})} \tag{4.2.17}$$

where the primed index runs over all unit cells. We note that the prefactor $H_{\alpha\beta}$ has no $\mathbf{k}$ dependence because it is calculated in the unit cell only. For performing calculations the k-grid fineness is determined by l_{cut}, which is related to E_{cut} by l^2_{cut} in atomic units.[49] A method developed by Monkhorst and Pack[50] to decrease computational cost involves displacing the origin of the k-grid from $\mathbf{k} = 0$, reducing the amount of inequivalent k-points. The idea behind this method is that the majority of the contribution to a BZ integral (e.g. $\rho_{\alpha\beta}$) is from $\mathbf{k}$ near the BZ boundary, with the error for a finite mesh, for $\mathbf{k} \neq 0$, proportional to $e^{-|\mathbf{k}|}$.

4.3 LAUTREC program

The LAUTREC (LAUsanne Total REal to Complex energy package) electronic structure code is an in-house code with a number of features not found in other electronic structure packages. This package uses plane-waves to perform self-consistent DFT calculations, with the unique capability to perform Wannier based polarization calculations in metallic systems. We will comment on a select few of the important methodologies employed by the package, that were not already discussed for the SIESTA program.

4.3.1 Plane-wave basis set

Since DFT focuses on solving problems involving crystals or other large periodic systems, representing wavefunctions using plane-waves as done by Bloch turns out to be advantageous.[51] We begin by considering a single particle electronic wavefunction ψ_i in a lattice potential with lattice vectors $\mathbf{a}_j$. To understand how the wavefunction varies in such a potential, we act on the wavefunction with a translation operator to get

$$\hat{T}_{\mathbf{R}}\psi_i(\mathbf{r}) = \psi_i(\mathbf{r}+\mathbf{R}) = c(\mathbf{R})\psi_i(\mathbf{r}) \tag{4.3.1}$$

where $c(\mathbf{R})$ is the eigenvalue of the translation operator. We show that $c(\mathbf{R})$ needs to be unitary because the total probability of finding the particle should be invariant under a translation, as follows

$$\int |\psi_i(\mathbf{r}+\mathbf{R})|^2 d\mathbf{r} = \int |c(\mathbf{R})\psi_i(\mathbf{r})|^2 d\mathbf{r} = \int |\psi_i(\mathbf{r})|^2 d\mathbf{r} \Rightarrow |c(\mathbf{R})|^2 = 1 \quad (4.3.2)$$

therefore we may write $c(\mathbf{R})$ as $e^{i\lambda(\mathbf{R})}$. To obtain the form of $\lambda(\mathbf{R})$ we note the following

$$\hat{T}_{\mathbf{R}_1}\hat{T}_{\mathbf{R}_2}\psi_i(\mathbf{r}) = c(\mathbf{R}_1)c(\mathbf{R}_2)\psi_i(\mathbf{r}) = \hat{T}_{\mathbf{R}_1+\mathbf{R}_2}\psi_i(\mathbf{r}) = c(\mathbf{R}_1+\mathbf{R}_2)\psi_i(\mathbf{r}) \quad (4.3.3)$$

which means that

$$c(\mathbf{R}_1)c(\mathbf{R}_2) = c(\mathbf{R}_1+\mathbf{R}_2) \quad (4.3.4)$$

for any $\mathbf{R}_1$ and $\mathbf{R}_2$. The functional form which fits this criteria is $e^{i\mathbf{k}\cdot\mathbf{R}}$ where $\mathbf{k}$ is, as of now, an arbitrary vector. Now since the wavefunction is in the lattice potential, the following must hold

$$\hat{T}_{\mathbf{R}}\psi_i(\mathbf{r}) = \psi_i(\mathbf{r}+\mathbf{R}) = e^{i\mathbf{k}\cdot\mathbf{R}}\psi_i(\mathbf{r}) \Rightarrow e^{i\mathbf{k}\cdot\mathbf{R}} = 1 \quad (4.3.5)$$

this suggests that

$$\mathbf{k} = \sum_i \theta_i \mathbf{b}_i \quad (4.3.6)$$

where θ_i are arbitrary constants and $\mathbf{b}_i$ are the reciprocal lattice vectors defined by $\mathbf{a}_i \cdot \mathbf{b}_j = 2\pi\delta_{ij}$. Then Eq. 4.3.5 is known as Bloch's theorem. To obtain the Bloch wavefunction, we modify Eq. 4.3.5 as follows

$$\psi_i(\mathbf{r}+\mathbf{R})e^{-i\mathbf{k}\cdot\mathbf{r}} = e^{i\mathbf{k}\cdot\mathbf{R}}\psi_i(\mathbf{r})e^{-i\mathbf{k}\cdot\mathbf{r}} \quad (4.3.7)$$

then after some algebra we arrive at

$$\psi_i(\mathbf{r}+\mathbf{R})e^{-i\mathbf{k}\cdot(\mathbf{r}+\mathbf{R})} = \psi_i(\mathbf{r})e^{-i\mathbf{k}\cdot\mathbf{r}} \equiv u_i(\mathbf{r}) \Rightarrow \psi_i(\mathbf{r}) = e^{i\mathbf{k}\cdot\mathbf{r}}u_i(\mathbf{r}) \quad (4.3.8)$$

where $u_i(\mathbf{r})$ is the periodic part of the Bloch wavefunction.

To avoid the calculation of a system with an infinite amount of electrons we can Fourier transform the periodic part of the electronic wavefunctions using plane-waves as follows

$$u_i(\mathbf{r}) = \sum_{\mathbf{G}} c_{i,\mathbf{G}} e^{i\mathbf{G}\cdot\mathbf{r}} \quad (4.3.9)$$

where $\mathbf{G}$ is the reciprocal lattice vector and the Bloch wavefunction becomes

$$\psi_i(\mathbf{r}) = \sum_{\mathbf{G}} c_{i,\mathbf{k}+\mathbf{G}} e^{i(\mathbf{k}+\mathbf{G})\cdot\mathbf{r}}. \tag{4.3.10}$$

While in theory the sum in Eq. 4.3.10 involving the basis set of $\mathbf{G}$ vectors is infinite, it turns out that the weights for small $\mathbf{G}$ are much more important than for the large ones.[52] Substituting Eq. 4.3.10 into the Kohn-Sham equations and integrating over $\mathbf{r}$, we arrive at

$$\begin{aligned}\sum_{\mathbf{G}'} \Big\{ &|\mathbf{k}+\mathbf{G}|^2 \delta_{\mathbf{G}\mathbf{G}'} + v_{ion}(\mathbf{G}-\mathbf{G}') + v_H(\mathbf{G}-\mathbf{G}') \\ &+ v_{xc}(\mathbf{G}-\mathbf{G}') \Big\} c_{i,\mathbf{k}+\mathbf{G}'} = \epsilon_i c_{i,\mathbf{k}+\mathbf{G}}.\end{aligned} \tag{4.3.11}$$

In calculations, the cut-off of the basis for the Hamiltonian matrix $H_{\mathbf{k}+\mathbf{G},\mathbf{k}+\mathbf{G}'}$ is determined by the energy cut-off $|\mathbf{k}+\mathbf{G}_c|^2$.

4.3.2 Car-Parrinello dynamics

Density functional theory usually concerns itself with finding the electronic ground state in the absence of temperature, while molecular dynamics is able to probe the dynamic evolution of systems at the cost of missing electronic information. The merging of the two principles was a huge step in *ab initio* simulations, and one of the first pioneers in this endeavor were Car and Parrinello.[53]

The derivation of the scheme begins by considering the energy functional of a single-particle system

$$\sum_i \langle \psi_i | \hat{H} | \psi_i \rangle = \sum_i \int \psi_i^*(\mathbf{r}) \Big\{ -\frac{1}{2}\nabla^2 + v_{eff}(\mathbf{r}) + v_N(\{R\}) + v_{ext}[\{\alpha\}] \Big\} \psi_i(\mathbf{r}) d\mathbf{r} \tag{4.3.12}$$

where v_{eff} includes the ionic, Hartree and exchange-correlation potentials, v_N is the nuclear potential, including external nuclear contributions and v_{ext} is the external functional where $\{\alpha\}$ are external constraints such as the volume or strain. We note that in this scheme our generalized coordinates are the sets of $\{\psi\}$, $\{R\}$ and $\{\alpha\}$. From Eq. 4.3.12 we can write down the time dependent Lagrangian

$$L = K - U - \Lambda \tag{4.3.13a}$$

$$K = \sum_i \int \frac{1}{2}\mu|\dot{\psi}_i|^2 d\mathbf{r} + \sum_I \frac{1}{2} M_I \dot{R}_I^2 + \sum_\nu \frac{1}{2}\mu_\nu \dot{\alpha}_\nu^2 \tag{4.3.13b}$$

$$U = \sum_i \int \psi_i^* \Big\{ -\frac{1}{2}\nabla^2 + v_{eff}(\mathbf{r}) + v_N(\{R\}) + v_{ext}[\{\alpha\}] \Big\} \psi_i d\mathbf{r} \tag{4.3.13c}$$

$$\Lambda = \sum_j \Lambda_{ij} \Big\{ \int \psi_i^* \psi_j d\mathbf{r} - \delta_{ij} \Big\} \tag{4.3.13d}$$

where we omit the $\mathbf{r}$ and t dependence of ψ for clarity and Λ_{ij} is the Lagrangian multiplier, μ and μ_ν are appropriate normalization constants and M_I is the atomic mass. The last term in Eq. 4.3.13a comes from the holonomic constraint that

$$\int \psi_i^*(\mathbf{r},t)\psi_j(\mathbf{r},t) d\mathbf{r} = \delta_{ij}. \tag{4.3.14}$$

We note that Eq. 4.3.13b has only quadratic terms since the first term is subject to constraints of Eq. 4.3.14 and the generalized coordinates of the last two terms do not have explicit time dependence.[54] Solving for the Euler-Lagrange equations from Eq. 4.3.13a we obtain the following equations of motion

$$\mu\ddot{\psi}_i(\mathbf{r},t) = \frac{1}{2}\nabla_{\mathbf{r}}^2 \psi_i(\mathbf{r},t) - v_{eff}(\mathbf{r}) + \sum_j \Lambda_{ij}\psi_j(\mathbf{r},t) \tag{4.3.15a}$$

$$M_I \ddot{R}_I = -\nabla_{R_I} v_N(\{R\}) \tag{4.3.15b}$$

$$\mu_\nu \ddot{\alpha}_\nu = -\frac{\partial v_{ext}[\{\alpha\}]}{\partial \alpha_\nu}. \tag{4.3.15c}$$

Usually to solve the equations of motion numerically, first the generalized velocities are initialized according to a Maxwellian distribution and then the Verlet algorithm[55] is employed which leads to a set of recurrence relations. Finally the equilibrium is reached when $\ddot{\psi}_i = 0$ corresponding to the Kohn-Sham ground state.

4.3.3 Finite field calculations

One of the main challenges in *ab inito* calculations is to relax a periodic system under an external electric field. This is primarily due to the ambiguity in calculating the polarization and the electrical boundary conditions that go along with it. We begin by using our knowledge of Maxwell's equations to write down the energy functional in the presence of a homogeneous electric field in the framework of DFT as

$$F[n;\mathbf{E}] = E_{KS}[n] + \int V(\mathbf{r})n(\mathbf{r})d\mathbf{r} = E_{KS}[n] - \int \mathbf{E}\cdot\mathbf{r}n(\mathbf{r})d\mathbf{r} \qquad (4.3.16)$$

where n is the electronic density and E_{KS} is the Kohn-Sham energy functional. Minimizing the new functional in Eq. 4.3.16 with respect to n, we arrive at the following Hamiltonian

$$\hat{H} = -\frac{1}{2}\nabla^2 + v_{eff}(\mathbf{r}) - \mathbf{E}\cdot\mathbf{r} \equiv \hat{H}^0 - \mathbf{E}\cdot\mathbf{r}. \qquad (4.3.17)$$

We can interpret Eq. 4.3.17 in the Bloch wavefunction basis and working in reciprocal space, we arrive at

$$F[u_{n\mathbf{k}};\mathbf{E}] = \sum_n \int_{\Omega_{BZ}} \langle u_{n\mathbf{k}}|\hat{H}^0_{\mathbf{k}}|u_{n\mathbf{k}}\rangle d\mathbf{k} - \frac{\Omega}{(2\pi)^3}\mathbf{E}\cdot\sum_n \int_{\Omega_{BZ}} \langle u_{n\mathbf{k}}|i\nabla_{\mathbf{k}}|u_{n\mathbf{k}}\rangle d\mathbf{k} \qquad (4.3.18)$$

where Ω is the volume of the supercell. While it looks like the minimization of Eq. 4.3.18 with respect to $u_{n\mathbf{k}}$ is tractable and can be solved, it actually turns out that stationary (bounded) states cannot exist because $V(\mathbf{r})$ is unbounded.[56, 57] Luckily, stationary solutions can exist, under a weak field, for a discrete k-mesh, which would be the case when Eq. 4.3.18 is solved numerically.[58]

Sometimes, having to fix $\mathbf{E}$ is not ideal, such as, in the case of ferroelectrics, where a non-zero electric field would prevent probing the properties near the centrosymmetric metastable state, like the energy barrier height. The paradigm shift to analyze these type of situations is by considering the displacement field $\mathbf{D}$ as the fixed variable rather than $\mathbf{E}$.[59] We begin by invoking the modern theory of polarization to realize that the last term in Eq. 4.3.18 contains the polarization, allowing us to write

$$F[n;\mathbf{E}] = E_{KS}[n] - \Omega\mathbf{E}\cdot\mathbf{P}[n] \qquad (4.3.19)$$

which is known as the electric enthalpy.[58] Then, we can create the following Legendre transformation (LT) relationship

$$F[\mathbf{E}] = \min_{\mathbf{P}}\Big[E_{KS}[\mathbf{P}] - \Omega\mathbf{E}\cdot\mathbf{P}\Big] \Leftrightarrow E_{KS}[\mathbf{P}] = \max_{\mathbf{E}}\Big[F[\mathbf{E}] + \Omega\mathbf{E}\cdot\mathbf{P}\Big] \quad (4.3.20)$$

where we dropped the n dependence for clarity. From Eq. 4.3.20 we have the following conjugate variables

$$\mathbf{P} = -\frac{1}{\Omega}\frac{dF}{d\mathbf{E}} \tag{4.3.21a}$$

$$\mathbf{E} = \frac{1}{\Omega}\frac{dE_{KS}}{d\mathbf{P}} \tag{4.3.21b}$$

which describe the same physics but in different ways. Another way to think about this is that the variable that is not fixed becomes a Lagrangian multiplier used in the extremization.[60] However, $\mathbf{P}$ is an awkward variable to fix since we do not know *a priori* what is a suitable polarization range to work with. Instead what we want are the conjugate variables of $\mathbf{E}$ and $\mathbf{D}$. This can be realized by noting that the long-range ($\mathbf{G} = 0$) field effects are missing from Eq. 4.3.19.[59] Including this contribution is equivalent to adding the energy from the electric field, resulting in

$$\tilde{F}[\mathbf{E}] = E_{KS} - \Omega\mathbf{E}\cdot\mathbf{P} - \frac{\Omega}{8\pi}|\mathbf{E}|^2. \tag{4.3.22}$$

Then we build a new LT relationship

$$U[\mathbf{D}] = \max_{\mathbf{E}}\left[\tilde{F}[\mathbf{E}] + \frac{\Omega}{4\pi}\mathbf{D}\cdot\mathbf{E}\right] \Leftrightarrow \min_{\mathbf{D}}\left[U[\mathbf{D}] - \frac{\Omega}{4\pi}\mathbf{D}\cdot\mathbf{E}\right] \tag{4.3.23}$$

with

$$\mathbf{E} = \frac{4\pi}{\Omega}\frac{dU}{d\mathbf{D}} \tag{4.3.24a}$$

$$\mathbf{D} = -\frac{4\pi}{\Omega}\frac{d\tilde{F}}{d\mathbf{E}} \tag{4.3.24b}$$

where the functional U is known as the internal energy. It is trivial to verify that Eq. 4.3.24b does indeed equal $\mathbf{E} + 4\pi\mathbf{P}$ as to be associated with the displacement field. Finally, rewriting U using Eq. 4.3.24a and after some algebra we arrive at

$$U[\mathbf{D}] = E_{KS}[n] + \frac{\Omega}{8\pi}\big(\mathbf{D} - 4\pi\mathbf{P}[n]\big)^2 \tag{4.3.25}$$

which needs to be minimized with respect to n, using essentially the same technique employed in Eq. 4.3.18.

5 Interfaces

5.1 Non-polar crystals

Interfaces are a natural part of materials and give them their properties much like the bulk. Even if the material is not known to have any intrinsic interfaces, it still comes in contact with the vacuum and if electrical properties need to be measured, a metal. We will highlight the microscopic effects at interfaces and how these effects contribute to the measurable macroscopic properties of the material. As it turns out these microscopic effects are crucial to understanding the electrostatics in superlattices. While the derivations here will be for semiconductors, modifications to the ideas and formulas for metals should be readily apparent.

5.1.1 Surfaces

Before we discuss interfaces, it is important to understand what happens in quasi-infinite crystals. We begin by intuitively stating that surface states should exist near the surface region and decay inside the bulk. If we consider a perfect crystal then the Bloch wavefunctions are a natural basis to work with. Then, if we want decaying solutions it is evident that **k** should take on complex values. This observations motivates us to solve

$$-\nabla^2\psi(\mathbf{r}) + V(\mathbf{r})\psi(\mathbf{r}) = E\psi(\mathbf{r}) \tag{5.1.1}$$

where $V(\mathbf{r})$ is the crystal potential, such that $V(\mathbf{r}+\mathbf{R}) = V(\mathbf{r})$. For a given E, we let $\psi_1(\mathbf{r},E)$ and $\psi_2(\mathbf{r},E)$ be the two solutions of Eq. 5.1.1. Then, assuming the full solution ψ have the same periodicity as the crystal potential we may write

$$\psi(\mathbf{R}) = \lambda\psi(0) \tag{5.1.2a}$$

$$\psi'(\mathbf{R}) = \lambda\psi'(0) \tag{5.1.2b}$$

with

$$\psi(\mathbf{r}) = \alpha\psi_1(\mathbf{r}) + \beta\psi_2(\mathbf{r}) \tag{5.1.3}$$

where λ is the eigenvalue of the translation operator and α and β are arbitrary constants to be determined. Inserting Eq. 5.1.2a and Eq. 5.1.2b into Eq. 5.1.3 we arrive at

$$\lambda^2 - 2\lambda\mu(E) + 1 = 0 \tag{5.1.4}$$

where

$$\mu(E) \equiv \frac{1}{2}\big[\psi_1(\mathbf{R}, E) + \psi_2'(\mathbf{R}, E)\big] \tag{5.1.5}$$

is referred to as the energy function. From the properties of the translation operator, λ can be written as $e^{i\mathbf{k}\cdot\mathbf{R}}$ and Eq. 5.1.4 can be rewritten as

$$cos(\mathbf{k}\cdot\mathbf{R}) = \mu(E) \tag{5.1.6}$$

and if we restrict ourselves to real $\mathbf{k}$, we recover the Bloch wavefunctions.[61]

The energy function gives the relation between $\mathbf{k}$ and E and has the following properties

$$E_{\mathbf{k}} = E_{-\mathbf{k}} \tag{5.1.7a}$$

$$E_{\mathbf{k}} = E_{\mathbf{k}+2\pi/\mathbf{R}} \tag{5.1.7b}$$

$$E_{\mathbf{k}^*} = (E_{\mathbf{k}})^*. \tag{5.1.7c}$$

In addition, in the large E limit, we should recover the free particle scenario, so that $|k| \approx E^{1/2}$ and $\mu(E) \approx cos(E^{1/2}|R|)$. Then writing $|k|$ as $2\pi n/|R|$ we can infer

$$\left.\frac{d\mu}{dE}\right|_{E=E_n} = 0, \qquad n \in \mathbb{N} \tag{5.1.8}$$

where negative integers were discarded because it would lead to solutions that blow up at large negative E. Furthermore from Eq. 5.1.8 we can Taylor expand near E_n to obtain

$$\mu(E) = \mu_n + \alpha_n(E - E_n)^2 + \cdots \tag{5.1.9}$$

which can be rearranged to

$$E(\mu) = E_n + \frac{1}{\sqrt{\alpha_n}}(\mu - \mu_n)^{1/2} \tag{5.1.10}$$

near the extremum. Note that inserting Eq. 5.1.6 into Eq. 5.1.10, shows that each μ_n is a branch point of $E(\mu)$. This is seen more clearly seen by considering

$$\frac{dE}{d\mathbf{k}} = \frac{dE}{d\mu}\frac{d\mu}{d\mathbf{k}} = -\frac{dE}{d\mu}(\hat{\mathbf{k}}\cdot\mathbf{R})sin(\mathbf{k}\cdot\mathbf{R}) \tag{5.1.11}$$

which means that E is analytical with respect to $\mathbf{k}$ except when $d\mu/dE$ vanishes, occurring at

$$\mu_n = cos(\mathbf{k}_n\cdot\mathbf{R}). \tag{5.1.12}$$

Then again, near E_n we can write

$$E(\mathbf{k}_n) = E_n + \beta_n(\mathbf{k} - \mathbf{k}_n)^{1/2} \tag{5.1.13}$$

where $\mathbf{k}_n$ is a solution to Eq. 5.1.12 and likewise has the same branch order.[61] We conclude by noting that the branch points $E(\mathbf{k}_n)$ are always found in between two adjacent bands and therefore we can physically attribute surface states to the density of states found in an energy gap.

Now we will highlight other properties of surfaces, from a macroscopic perspective, beginning with a physical fact that the electric potential V must be smooth. Then, for the infinite crystal let us define the cell averaged crystal potential

$$\bar{V}(\mathbf{r}) = \frac{1}{\Omega}\int_{\Omega} V(\mathbf{r} + \mathbf{r}')d\mathbf{r}' \tag{5.1.14}$$

where Ω is the volume of the primitive cell. For a perfect infinite crystal $\bar{V}(\mathbf{r})$ is a constant V_{cell}, arbitrarily chosen, because we cannot reference a point out at infinity, away from the charge distribution. In the literature it is conventional to set V_{cell} to either ϵ_F or ϵ_{VBM}, the Fermi energy of the metal (chemical potential in gapped materials) or the eigenenergy of the valence band maximum, respectively.

However once a surface is introduced, $\bar{V}$ is no longer a constant and, near a surface, we can write

$$\bar{V}(\mathbf{r}) = V_{cell} + V_{SXD}(\mathbf{r}) \tag{5.1.15}$$

where V_{SXD} is the electric potential due to surface effects (both intrinsic and extrinsic), enforcing the smoothness as we pass from the bulk region into the vacuum and is usually slow varying. The $\mathbf{r}$ dependence of $\bar{V}$ means that the energies of the crystal have the same dependency as follows

$$E_i(\mathbf{r}) = \epsilon_i + \bar{V}(\mathbf{r}) \tag{5.1.16}$$

where ϵ_i are the eigenenergies of the bulk Hamiltonian defined in Eq.5.1.1. To highlight why this is important, Fig. 5 shows a semiconductor-vacuum interface where the band edges (E_{CBM} and E_{VBM}) are bent (aligned) towards the vacuum energy level at infinity ($E_{vac}^{\infty} = 0$). Details of the surface states are responsible for this band alignment, which modifies experimentally measurable quantities, such as the ionization energy I_S and the electron affinity χ_S.[4] We defer discussing the specific form of $V_{SXD}(\mathbf{r})$ and just state that it can be recovered from *ab initio* calculations.[62]

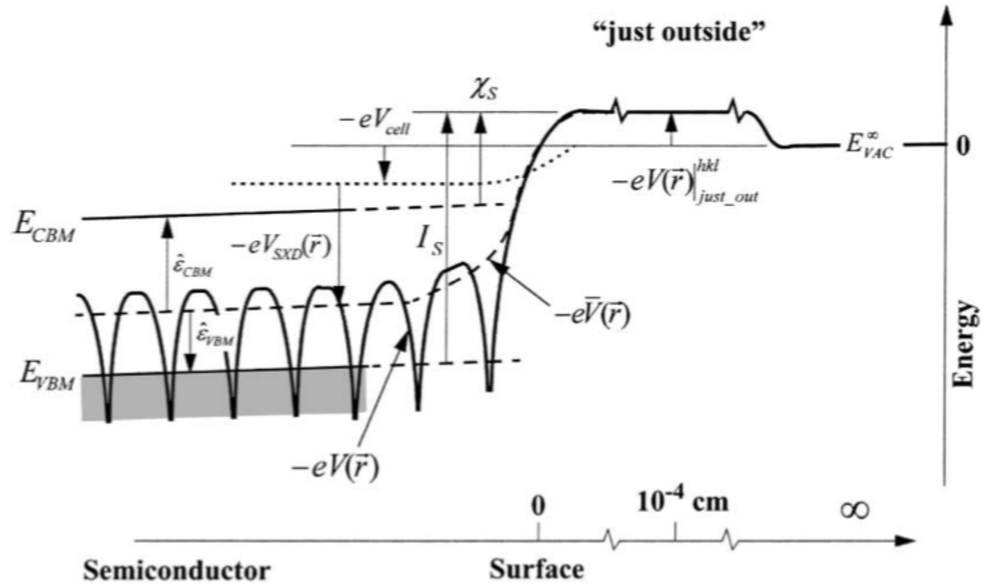

Figure 5: The distribution of electric potentials as well as the band edges near a surface of a semiconductor. Taken from Ref. [4]

5.1.2 Charge neutral Fermi energy

Throughout this discussion we will restrict ourselves to only considering interfaces between non-polar crystals, such as most semiconductors and metals. In mathematical terms, any material that does not have a polar point group symmetry.[63] The important idea governing interfaces is the redistribution of free charge, at the interface between two materials, occurring in such a way that the average charge around the interface region should be neutral. In other words, combining two charge neutral materials should not give rise to large regions of net deficient or excess charge.

The main principle behind a net neutral system is that the position of the Fermi energy must be matched (pinned) between the two materials, such that the total contributions from the surface density of states averages to zero.[4] From our previous discussion on complex bands, we know that surface states exist on branch points $\mathbf{k}_n$ between bands of real $\mathbf{k}$ and therefore it is likely that the pinned Fermi energy should be near those branch points.[64] In addition because the Bloch wavefunctions form a complete basis, we could write our surface states as linear combinations of Bloch states. It turns out a convenient tool to parse the Bloch wavefunctions (and thus the surface states) is to analyze their "response" or more qualitatively their contribution to the Green's function of the system.[65]

The Green's function for the Hamiltonian given in Eq.5.1.1 was calculated[66] to be

$$G(\mathbf{r},\mathbf{r}',\epsilon) = \sum_{n\mathbf{k}} \frac{\psi_{n\mathbf{k}}(\mathbf{r})\psi^*_{n\mathbf{k}}(\mathbf{r}')}{\epsilon - \epsilon_{n\mathbf{k}}} \tag{5.1.17}$$

where $\psi_{n\mathbf{k}}$ and $\epsilon_{n\mathbf{k}}$ is the Bloch wavefunction and eigenenergy, respectively. Since we are interested in contributions over a region, let us use the same argument to reach Eq. 5.1.14 and write the cell averaged Green's function

$$\bar{G}(\mathbf{r},\epsilon) = \frac{1}{\Omega}\sum_{n\mathbf{k}} \int_{\Omega} \frac{\psi_{n\mathbf{k}}(\mathbf{r}')\psi^*_{n\mathbf{k}}(\mathbf{r}+\mathbf{r}')}{\epsilon - \epsilon_{n\mathbf{k}}} d\mathbf{r}' = \frac{1}{\Omega}\sum_{n\mathbf{k}} \frac{e^{i\mathbf{k}\cdot\mathbf{r}}}{\epsilon - \epsilon_{n\mathbf{k}}} \tag{5.1.18}$$

where we have used the normalization property of the Bloch wavefunctions to write the last result. The key to evaluating Eq. 5.1.18 is by choosing $\mathbf{r}$ to be perpendicular to the interface, or the direction with the most charge redistribution.[65] Finally, using the input of the band structure and varying ϵ until there is a sign change which corresponds to the pinning of the charge neutral Fermi energy.

We conclude with a qualitative picture of semiconductor interfaces.[67] In the high surface density (Bardeen) limit, the semiconductor has a lot of surface states, therefore the Fermi energy is so strongly pinned that the details of the metal (work function, etc.) have little influence on the bands. In the low surface density (Schottky) limit, the band alignment is strongly dependent on the metal, specifically the chemical bonding at the interface. Finally we emphasize that V_{cell} in a composite system is arbitrary and in no way can be computed from the two materials independently. Therefore care must be taken when comparing density of states, or other properties of the eigenenergies, between the two materials and their combination.

5.2 Polar crystals

For polar crystals, like ferroelectrics, we are primarily interested in what happens to the polarization as we introduce surfaces or interfaces. Once we truncate an infinite polar crystal a polarization within the crystal is not guaranteed. Before, it was energetically favorable for the polarization to exist throughout the whole space, but now Maxwell's equations tell us that areas without bound charges should not contain polarization. This physical principle leads the system to redistribute charge so that the polarization will be screened outside the polar region, and the mechanism is called the depolarization field. We will discuss the depolarization field within the framework of LGD theory. Finally, regarding band alignment, much of what has been discussed in the previous section still holds, but now an additional term is present due to the displacement field caused by the ferroelectric.[68]

5.2.1 Depolarization field

Surfaces and interfaces can not only give rise to a parallel component in the polarization but also an additional perpendicular component to the bulk polarization. Usually such contributions lower the overall polarization[69] and therefore are referred to as depolarization effects or field. The origin of the depolarization field, in the context of electrodes attached to a film, results in a build up of free charge at the metal-ferroelectric interface to screen the bound charge that is responsible for the ferroelectricity. In Fig. 6a we have a typical setup of a ferroelectric film sandwiched between two metal electrodes with the free charge, electric potential and depolarization field profiles shown in Fig. 6b-6d, respectively. We begin by considering the contribution to the free energy coming from the depolarization field E_d which can be written as

$$F_d = -\frac{1}{2}\int_{\Omega} E_d(\mathbf{r})P(\mathbf{r})d\mathbf{r} \tag{5.2.1}$$

where Ω is the volume of the ferroelectric film. We can further simplify the above expression[70] by considering spatial changes only along the z direction and considering a ferroelectric perfectly insulating, allowing us to rewrite the depolarization field as

$$E_d(z) = Q/\epsilon_f + P(z)/\epsilon_f \tag{5.2.2}$$

where ϵ_f is the permittivity of the film. Furthermore, if we consider the case where $\lambda \ll d$ we can rewrite[69] Q as

$$Q = -\theta P \tag{5.2.3}$$

where

$$\theta = \frac{\epsilon_e/\lambda}{2\epsilon_f/d + \epsilon_e/\lambda}. \tag{5.2.4}$$

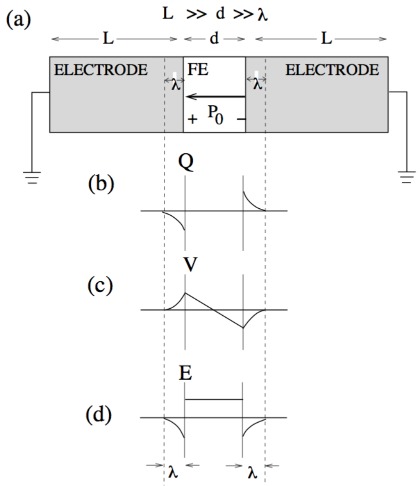

Figure 6: (a) Schematic of short-circuited ferroelectric capacitor with $L \gg d \gg \lambda$, where λ is the screening length, and accompanying plots of the spatial distribution of (b) the free charge Q, (c) the potential V and (d) the depolarization field E. Note that the charge distribution in (b) would simply be Delta functions at the film-electrode interfaces for perfect electrodes; then V and E would simply be constant and zero. Taken from Ref. [5]

Finally, inserting Eq. 5.2.2 and Eq. 5.2.3 into Eq. 5.2.1 yields

$$F_d = -\frac{1}{2\epsilon_f}\int_{-d/2}^{d/2} P^2(1-\theta)dz = \frac{d(\theta-1)}{\epsilon_f}P^2. \tag{5.2.5}$$

We conclude by noting that if either $\lambda \to 0$ or $d \to \infty$ then the depolarization field vanishes and also since the new contribution is proportional to P^2 it has an effect of shifting the Curie temperature.

6 Defects

6.1 Formation Energy

In experiments, the materials synthesized deviate from an ideal crystal. Imperfections in the form of defects, impurities, elastic deformation and cracking will be present in the material. The presence of defects are of great importance, especially in semiconductors and ferroelectrics, where they can change the electrical and optical properties significantly.[71] From a theoretical perspective, the quantity of interest is the defect formation energy, which allows for the calculation of the defect concentration that would be seen in experiments.[71] However, linking computation and experiment is problematic due to the computational cost required to simulate realistic defect concentrations. Large supercells, and therefore many atoms, are required due to periodic boundary conditions. In this section we will outline a general formalism of defect calculations and corrections to results for the defect systems.

Within the DFT formalism of using supercells, the formation energy of a collection of defects D, with their total charge q, in a host system can be calculated[72] as follows

$$\Delta H = E_D - E_H + q(\epsilon_v + \Delta\epsilon_F) + \sum_i n_i \mu_i \tag{6.1.1}$$

where E_D, E_H, ϵ_v, $\Delta\epsilon_F$, n_i and μ_i is the total energy of host+defect supercell, total energy of host supercell, energy of the valence band maximum (VBM) of the host, Fermi energy relative to the VBM, number of i'th defects in the supercell and chemical potential of the i'th defect.

In principle, ϵ_v can be calculated from the energy difference with the host supercell and the host supercell with the missing electron responsible for the VBM, but, most *ab initio* packages do not allow removing of specific electrons. However, it can be shown,[73] with a moderately sized supercell, the value of ϵ_v approaches the difference between the host supercell and the host+hole ($q = +1$) supercell. With ϵ_v we can now properly calculate $\Delta\epsilon_F$ with the correct reference.

The chemical potential of a defect is defined as the most stable phase of the defect in bulk. Since the most stable phase is dependent on the experimental growth conditions, sometimes it is convenient to redefine μ_i as

$\mu_i^0 + \Delta\mu_i$, where μ_i^0 is the chemical potential of the elemental phase and $\Delta\mu_i$ is a free parameter to account for the growth conditions.

6.2 Defect corrections

6.2.1 Shallow level shift correction

The well known problem of the band gap can be fixed in a simplistic fashion by introducing a energy shift for the conduction band maximum (CBM) and valence band maximum (VBM), $\Delta\epsilon_C$ and $\Delta\epsilon_V$, respectively. Since the formation energy linearly depends on the relative Fermi energy, it can also be possible that it would depend on the energy shift introduced. It turns out that this statement is true when the defect forms a shallow (near band edge) level, that modifies the edge bands, which is referred to as a perturbed-host state.[74] The correction to this effect is adding $z_e\Delta\epsilon_C$ or $-z_h\Delta\epsilon_V$ to the formation energy, where the donor or acceptor level is occupied by z_e electrons or z_h holes, respectively.

6.2.2 Moss-Burstein-type correction

If the supercell is small or the density of defects sufficiently high then the donor (acceptor) states shift the conduction (valence) band edge and thus decrease the size of the band gap, this is known as the Moss-Burstein effect (only for donor states).[75] However, we can recover the formation energy in the dilute defect limit by adding to the total energy the term

$$E_{MB} = -\sum_n \int \Theta(\epsilon_n(\mathbf{k}) - \epsilon_C)\big(w(\mathbf{k})f_n(\mathbf{k})\epsilon_n(\mathbf{k}) - \epsilon_C\big)d\mathbf{k} \tag{6.2.1}$$

for donor dominated and

$$E_{MB} = -\sum_n \int \Theta(\epsilon_V - \epsilon_n(\mathbf{k}))\big(\epsilon_V - w(\mathbf{k})f_n(\mathbf{k})\epsilon_n(\mathbf{k})\big)d\mathbf{k} \tag{6.2.2}$$

for acceptor dominated supercells. Here ϵ_n, ϵ_C, ϵ_V, w, f and Θ is the KS eigenenergy, CBM eigenenergy, VBM eigenenergy, k-point weight, fractional occupation and step function, respectively.

6.2.3 Jellium correction

If the defects present are not charge neutral then we have long range Coulomb forces and the total energy does not converge. In *ab initio* calculations the convention[76] is to set $V_{ion}(\mathbf{G}=0)$ and $V_H(\mathbf{G}=0)$ to zero, where $\mathbf{G}$ is the reciprocal lattice vector, allowing for convergence. This is valid for charge neutral systems because the average potential of the crystal is an arbitrary constant, however when the system is charged, such a convention gives rise to a physical compensating jellium. We can account for the creation of this jellium by adding $-q\alpha_{PP}$ to the total energy, with α_{PP} defined as

$$\alpha_{PP} = \frac{1}{\Omega}\sum_j \int_\Omega \left(V^{PP}_{ion,j}(\mathbf{r}) + \frac{Z_j}{\mathbf{r}} \right) d\mathbf{r} \tag{6.2.3}$$

where Ω is the volume of the supercell.[76]

6.2.4 Image charge correction

Localized charged defects within a periodic system interact with one another, which from an *ab initio* point of view, can be thought as image charges interacting between neighbouring supercells. The additional term to the energy would depend on the distribution of localized charges, as well how well they are screened by the compensating background. It can be shown[77] that the contribution to the energy is

$$E_{MP} = \frac{q^2\alpha_M}{2\epsilon\Omega^{-1/3}} + \frac{2\pi q Q}{3\epsilon\Omega^{-1/3}} \tag{6.2.4}$$

where α_M, ϵ, and Q is the Madelung constant, static dielectric constant and the second radial moment, respectively. With Q defined as

$$Q = \int_\Omega \tilde{\rho}(\mathbf{r}) r^2 d\mathbf{r} \tag{6.2.5}$$

where $\tilde{\rho}$ is the difference in the electron density between the host+defect and host supercells.

7 Stochastic Mechanics

7.1 Brownian Motion

Stochastic processes are commonly classified by a random sequence of events on some mathematical space,[78] such as phase space, for example, and exist in many areas of physics. Brownian motion is the quintessential physical example of a stochastic process. The motion describes a particle as it is vibrating in a fluid and is governed by the Langevin equation. Later on we will show that we can generalize the particle and fluid to a multitude of systems. Understanding these concepts will further motivate discussion on this topic.

7.1.1 Langevin equation

The Langevin equation is nothing more than Newton's equation of motion describing a particle in a viscous medium subject to a random force. This equation of motion is

$$m\frac{d\mathbf{v}}{dt} = -\gamma\mathbf{v} + \boldsymbol{\eta}(t) \tag{7.1.1}$$

where m, γ and $\boldsymbol{\eta}$ is the mass, friction coefficient and the random force, respectively. To solve the inhomogeneous part of this first-order differential equation we make the following substitution

$$\mathbf{v}(t) = e^{-\frac{\gamma}{m}t}\mathbf{u}(t) \tag{7.1.2}$$

then

$$e^{-\frac{\gamma}{m}t}\frac{d\mathbf{u}}{dt} = \boldsymbol{\eta}(t)/m \tag{7.1.3}$$

with the solution

$$\mathbf{u}(t) = \mathbf{u}(0) + \int_0^t dt' e^{\frac{\gamma}{m}t'}\boldsymbol{\eta}(t')/m \tag{7.1.4}$$

where we have used $\mathbf{v}(0) = \mathbf{u}(0)$. Using Eq. 7.1.2 and combining the homogeneous solution, we arrive at the complete solution

$$\mathbf{v}(t) = \mathbf{v}(0)e^{-\frac{\gamma}{m}t} + \int_0^t dt' e^{\frac{\gamma}{m}(t-t')}\boldsymbol{\eta}(t')/m. \tag{7.1.5}$$

While we have described the motion of the particle, we did not touch upon the properties of $\boldsymbol{\eta}(t)$. Before we begin, it is useful to think about stochastic quantities by their time average define by

$$\langle A \rangle = \frac{1}{T}\int_0^T A(t)dt \tag{7.1.6}$$

where the accuracy of the time average improves as T approaches infinity. Then, the fluctuation of A is given by

$$\delta A(t) = A(t) - \langle A \rangle. \tag{7.1.7}$$

For a fluid, it helps to think of the origin of $\boldsymbol{\eta}(t)$ as the interaction between the fluid molecules and the Brownian particle. If the fluid is homogeneous there should not be a preferred direction for the force, and we can associate $\boldsymbol{\eta}(t)$ with $\delta\mathbf{F}(t)$, where $\mathbf{F}$ is produced from said interactions. Then, from the definition of Eq. 7.1.7, we can state

$$\langle \boldsymbol{\eta}(t) \rangle = 0. \tag{7.1.8}$$

In addition, the random forces should not be correlated in any way and therefore

$$\langle \mathbf{F}(t) \cdot \mathbf{F}(t') \rangle = \langle \mathbf{F}(t) \rangle \cdot \langle \mathbf{F}(t') \rangle = \langle F \rangle^2. \tag{7.1.9}$$

This can be alternatively written, using Eq. 7.1.7, as

$$\langle \boldsymbol{\eta}(t) \cdot \boldsymbol{\eta}(t') \rangle = 2D\delta(t - t') \tag{7.1.10}$$

where $2D$ is the variance of $\mathbf{F}(t)$.

To understand where the properties of $\boldsymbol{\eta}(t)$ are useful, let us consider the equipartition theorem, which states

$$\langle v^2 \rangle = k_B T/m \tag{7.1.11}$$

where k_B and T is the Boltzmann constant and the temperature of the system at thermal equilibrium, respectively. Using Eq. 7.1.5, we can calculate square of the velocity to be

$$\begin{aligned}\mathbf{v}(t) \cdot \mathbf{v}(t) = v^2(t) = v^2(0)e^{-2\frac{\gamma}{m}t} + 2\mathbf{v}(0) \cdot \int_0^t dt' e^{\frac{\gamma}{m}(t-t')}\boldsymbol{\eta}(t')/m \\ + \int_0^t dt' e^{\frac{\gamma}{m}(t-t')}\boldsymbol{\eta}(t') \cdot \int_0^t dt'' e^{\frac{\gamma}{m}(t-t'')}\boldsymbol{\eta}(t'')/m^2.\end{aligned} \tag{7.1.12}$$

Now taking the time average (only on stochastic quantities) and using Eq. 7.1.8 and Eq. 7.1.10, we arrive at

$$\langle v^2(t)\rangle = v^2(0)e^{-2\frac{\gamma}{m}t} + \frac{D}{\gamma m}(1 - e^{-2\frac{\gamma}{m}t}) \tag{7.1.13}$$

after evaluating the double integral. Observe that in the long time limit we have

$$\langle v^2(t)\rangle = \frac{D}{\gamma m} \tag{7.1.14}$$

meaning that the system is always in motion, and why D is referred to as the diffusion constant. Furthermore, in the long time limit, we are in thermal equilibrium, so that

$$\langle v^2\rangle = k_BT/m = \frac{D}{\gamma m} \tag{7.1.15}$$

and the result

$$D = \gamma k_B T \tag{7.1.16}$$

is known as the fluctuation-dissipation theorem.

7.1.2 Multiparticle Langevin equation

We can extend the Langevin equation to where we have more than one "particle" and write

$$m_i\frac{d\mathbf{v}_i}{dt} = \gamma_i\mathbf{v}_i + \boldsymbol{\eta}_i(t). \tag{7.1.17}$$

Clearly the solution to the multiparticle version is Eq. 7.1.5, but now with an attached index for each particle and with the diffusion constant given by

$$\langle\boldsymbol{\eta}_i(t)\cdot\boldsymbol{\eta}_j(t')\rangle = 2D_{ij}\delta(t-t'). \tag{7.1.18}$$

Let us now consider the fluctuation-dissipation theorem for the multiparticle case by calculating

$$\begin{aligned}\mathbf{v}_i(t)\cdot\mathbf{v}_j(t) = {}& \mathbf{v}_i(0)\cdot\mathbf{v}_j(0)e^{-(\frac{\gamma_i}{m_i}+\frac{\gamma_j}{m_j})t} + \mathbf{v}_i(0)\cdot\int_0^t dt' e^{\frac{\gamma_i}{m_i}(t-t')}\boldsymbol{\eta}_j(t')/m_j \\ &+ \mathbf{v}_j(0)\cdot\int_0^t dt' e^{\frac{\gamma_j}{m_j}(t-t')}\boldsymbol{\eta}_i(t')/m_i \\ &+ \int_0^t dt' e^{\frac{\gamma_i}{m_i}(t-t')}\boldsymbol{\eta}_i(t')\cdot\int_0^t dt'' e^{\frac{\gamma_j}{m_j}(t-t'')}\boldsymbol{\eta}(t'')/(m_i m_j)\end{aligned} \tag{7.1.19}$$

and taking the time average of this expression yields

$$\langle \mathbf{v}_i(t) \cdot \mathbf{v}_j(t) \rangle = \mathbf{v}_i(0) \cdot \mathbf{v}_j(0) e^{-(\frac{\gamma_i}{m_i} + \frac{\gamma_j}{m_j})t} + \frac{2D_{ij}}{\gamma_i m_j + \gamma_j m_i} \Big[1 - e^{-(\frac{\gamma_i}{m_i} + \frac{\gamma_j}{m_j})t} \Big]. \tag{7.1.20}$$

Next, in the long time limit, Eq. 7.1.20 becomes

$$\langle \mathbf{v}_i(t) \cdot \mathbf{v}_j(t) \rangle \equiv \Omega_{ij} = \frac{2D_{ij}}{\Gamma_{ij} + \Gamma_{ij}^{\dagger}} \tag{7.1.21}$$

where $\Gamma_{ij} \equiv \gamma_i m_j$. Solving for D_{ij} results in

$$D_{ij} = \frac{1}{2} \Omega_{ij} (\Gamma_{ij} + \Gamma_{ij}^{\dagger}) \tag{7.1.22}$$

which is the multiparticle fluctuation-dissipation theorem. We note that Γ_{ij} can be decomposed into a symmetric and antisymmetric matrix, giving rise to reciprocal relations,[79] however we do not consider this here.

7.2 Fokker-Planck equations

While describing the random motion of particles has its usefulness, the fact that randomness is involved implies that we can consider the probability distribution of the particles. This allows us to get additional insights into the system because once we have a large amount of particles to track they become hard to analyze and visualize. The Fokker-Planck equations connect the equations for motion and probability density together.

7.2.1 Derivation

Let us begin by considering a generalized version of the Langevin equation

$$\frac{da_i}{dt} = \phi_i(a_1, a_2, \cdots) + \eta_i(t) \tag{7.2.1}$$

where we have dropped the possibility that dynamic variables a_i can be vectors for simplicity. We also assume that η_i is Gaussian noise and therefore

$$\langle \eta_i(t) \eta_j(t') \rangle = 2D_{ij} \delta(t - t'). \tag{7.2.2}$$

We can vectorize these equations as

$$\frac{d\mathbf{a}}{dt} = \boldsymbol{\phi}(\mathbf{a}) + \boldsymbol{\eta}(t) \tag{7.2.3}$$

and

$$\langle \boldsymbol{\eta}(t)\boldsymbol{\eta}(t')\rangle = 2\mathbf{D}\delta(t-t') \tag{7.2.4}$$

where the notation $\mathbf{a} \equiv (a_1, a_2, \cdots)$ is used.

To answer the question what is the probability distribution $\rho(\mathbf{a}, t)$ associated with the generalized Langevin equation we need to derive some properties of the distribution. If the system is closed, physically, the total probability should be conserved and

$$\int \rho(\mathbf{a}, t) d\mathbf{a} = 1, \qquad \forall t. \tag{7.2.5}$$

The conservation of probability implies the following continuity equation

$$\frac{\partial \rho(\mathbf{a}, t)}{\partial t} = -\nabla_{\mathbf{a}} \cdot \left(\frac{\partial \mathbf{a}}{\partial t} \rho(\mathbf{a}, t) \right) \tag{7.2.6}$$

and inserting Eq. 7.2.3 into Eq. 7.2.6 we arrive at

$$\frac{\partial \rho(\mathbf{a}, t)}{\partial t} = -\nabla_{\mathbf{a}} \cdot \Big(\boldsymbol{\phi}(\mathbf{a})\rho(\mathbf{a}, t) + \boldsymbol{\eta}(t)\rho(\mathbf{a}, t) \Big). \tag{7.2.7}$$

To solve Eq. 7.2.7 we make the following ansatz

$$\rho(\mathbf{a}, t) = e^{-t\hat{L}} f(\mathbf{a}, t) \tag{7.2.8}$$

where $\hat{L} = \nabla_{\mathbf{a}} \cdot \boldsymbol{\phi}(\mathbf{a}) + \boldsymbol{\phi}(\mathbf{a}) \cdot \nabla_{\mathbf{a}}$ is analogous to the Liouville operator. Then Eq. 7.2.7 becomes

$$\frac{\partial f(\mathbf{a}, t)}{\partial t} = -e^{t\hat{L}} \nabla_{\mathbf{a}} \cdot \boldsymbol{\eta}(t) e^{-t\hat{L}} f(\mathbf{a}, t). \tag{7.2.9}$$

Next, taking the time integral on both sides and using Eq. 7.2.8 again, we arrive at

$$\rho(\mathbf{a}, t) = \rho(\mathbf{a}, 0)e^{-t\hat{L}} - \int_0^t e^{-(t-t')\hat{L}} \nabla_{\mathbf{a}} \cdot \boldsymbol{\eta}(t')\rho(\mathbf{a}, t')dt'. \tag{7.2.10}$$

While Eq. 7.2.10 is hard to work with due to the time integral and ρ appearing on both sides, we can insert the solution into Eq. 7.2.7 to yield

$$\begin{aligned} \frac{\partial \rho(\mathbf{a}, t)}{\partial t} = &- \nabla_{\mathbf{a}} \cdot \boldsymbol{\phi}(\mathbf{a})\rho(\mathbf{a}, t) - \nabla_{\mathbf{a}} \cdot \boldsymbol{\eta}(t)\rho(\mathbf{a}, 0)e^{-t\hat{L}} \\ &+ \nabla_{\mathbf{a}} \cdot \boldsymbol{\eta}(t) \int_0^t e^{-(t-t')\hat{L}} \nabla_{\mathbf{a}} \cdot \boldsymbol{\eta}(t')\rho(\mathbf{a}, t')dt'. \end{aligned} \tag{7.2.11}$$

Then taking the time average and using the following identity for Gaussian noise[80]

$$\begin{aligned}\langle \boldsymbol{\eta}(t)\boldsymbol{\eta}(t')\rho[\boldsymbol{\eta}(t')]\rangle &= \mathbf{D}\frac{\partial}{\partial \boldsymbol{\eta}(t)}\langle \boldsymbol{\eta}(t)\rho[\boldsymbol{\eta}(t')]\rangle \\ &= \mathbf{D}\langle \rho[\boldsymbol{\eta}(t')]\rangle + \mathbf{D}\langle \boldsymbol{\eta}(t)\frac{\partial}{\partial \boldsymbol{\eta}(t)}\rho[\boldsymbol{\eta}(t')]\rangle = \mathbf{D}\langle \rho[\boldsymbol{\eta}(t')]\rangle\end{aligned} \tag{7.2.12}$$

results in

$$\frac{\partial\langle \rho(\mathbf{a},t)\rangle}{\partial t} = -\nabla_{\mathbf{a}}\cdot\boldsymbol{\phi}(\mathbf{a})\langle\rho(\mathbf{a},t)\rangle + \nabla_{\mathbf{a}}\cdot\mathbf{D}\cdot\nabla_{\mathbf{a}}\langle\rho(\mathbf{a},t)\rangle \tag{7.2.13}$$

the Fokker-Planck (FP) equations for the time averaged $\rho(\mathbf{a},t)$.

7.2.2 Properties

In this section we will mention a few of the interesting properties of the FP equations, specifically their analogy to quantum mechanics. We begin by writing the FP equations in the following way

$$\frac{\partial}{\partial t}\rho(\mathbf{a},t) = \hat{D}\rho(\mathbf{a},t) \tag{7.2.14}$$

where

$$-\nabla_{\mathbf{a}}\cdot\boldsymbol{\phi}(\mathbf{a}) + \nabla_{\mathbf{a}}\cdot\mathbf{D}\cdot\nabla_{\mathbf{a}} \tag{7.2.15}$$

is the FP operator. Then the formal solution to Eq. 7.2.14 is

$$\rho(\mathbf{a},t) = e^{t\hat{D}}\rho(\mathbf{a},0). \tag{7.2.16}$$

The expectation value of a stochastic quantity $\psi(\mathbf{a})$ can be calculated in the following way

$$\langle\psi(\mathbf{a})\rangle = \int \psi(\mathbf{a})\rho(\mathbf{a},t)d\mathbf{a} = \int \psi(\mathbf{a})e^{t\hat{D}}\rho(\mathbf{a},0)d\mathbf{a} \tag{7.2.17}$$

where the expression is evaluated at time t.

Now let us calculate the adjoint of $\hat{D}$ defined by

$$f(\mathbf{a})\hat{D}g(\mathbf{a}) = g(\mathbf{a})\hat{D}^{\dagger}f(\mathbf{a}) \tag{7.2.18}$$

to be

$$\hat{D}^\dagger = \boldsymbol{\phi}(\mathbf{a}) \cdot \nabla_{\mathbf{a}}(\mathbf{a}) + \nabla_{\mathbf{a}} \cdot \mathbf{D} \cdot \nabla_{\mathbf{a}}. \tag{7.2.19}$$

Then the expectation value of a stochastic quantity $\psi(\mathbf{a})$ can also be written as

$$\langle \psi(\mathbf{a}) \rangle = \int \rho(\mathbf{a}, t)\psi(\mathbf{a})d\mathbf{a} = \int \rho(\mathbf{a}, 0)e^{t\hat{D}^\dagger}\psi(\mathbf{a})d\mathbf{a} \equiv \int \rho(\mathbf{a}, 0)\psi(\mathbf{a}, t)d\mathbf{a} \tag{7.2.20}$$

where we defined a time dependent stochastic quantity $\psi(\mathbf{a}, t)$.

The approach of either using $\hat{D}$ or $\hat{D}^\dagger$ to calculate the expectation value is analogous to interpreting quantum mechanics in the Schödinger or Heisenberg representation, respectively.[80] Since in the Schödinger representation we think of the observables (or operators) and the quantum states (and hence probability density) to be time independent and dependent, respectively. While in the Heisenberg representation the converse is true.

7.3 Kramers problem

The Kramers problem[81] asks what is the rate at which a set of Brownian particles (or stochastic variables) escape a potential well. We will approach the answer to this question using the theory of first passage time. As examples, we will give exact solutions for a single Brownian particle in the large and small friction limit.

7.3.1 Mean first passage time

We begin by considering a set of stochastic variables (or particles) $\mathbf{a}$ which are initialized to $\mathbf{a}_0$ and located inside a region of volume V in $\mathbf{a}$-space.[80] Then the probability distribution is governed by

$$\frac{\partial}{\partial t}\langle \rho(\mathbf{a}, t)\rangle = \hat{D}\langle \rho(\mathbf{a}, t)\rangle \tag{7.3.1}$$

with initial conditions

$$\langle \rho(\mathbf{a}, 0)\rangle = \delta(\mathbf{a} - \mathbf{a}_0). \tag{7.3.2}$$

Now because we want to know how many particles are left in V, we should limit our solutions of Eq. 7.3.1 to the following boundary condition

$$\langle \rho(\mathbf{a}, t)\rangle = 0, \qquad \mathbf{a} \in \partial V \tag{7.3.3}$$

and let ∂V be absorbing (non-reflecting). The formal solution, assuming we limit the solutions, to Eq. 7.3.1 is

$$\langle \rho(\mathbf{a}, t)\rangle = e^{t\hat{D}}\delta(\mathbf{a} - \mathbf{a}_0). \tag{7.3.4}$$

To measure the amount of particles in V at time t, we calculate

$$S(t, \mathbf{a}_0) = \int_V \langle \rho(\mathbf{a}, t)\rangle d\mathbf{a} \tag{7.3.5}$$

which explicitly depends on the initial conditions. Then the distribution of the rate at which the particles leave, also known as first passage time, is $-dS(t, \mathbf{a}_0)/dt$. The mean first passage time is then the the first moment of t

$$\tau(\mathbf{a}_0) = -\int_0^\infty \frac{dS(t, \mathbf{a}_0)}{dt} t dt = -S(t, \mathbf{a}_0)t\Big|_0^\infty + \int_0^\infty S(t, \mathbf{a}_0)dt = \int_0^\infty S(t, \mathbf{a}_0)dt \tag{7.3.6}$$

where we have used the fact that $S(t, \mathbf{a}_0)$ vanishes at large t due to absorbing boundary conditions. Then, inserting Eq. 7.3.5 into Eq. 7.3.6 yields

$$\tau(\mathbf{a}_0) = \int_0^\infty dt \int_V \langle \rho(\mathbf{a}, t)\rangle d\mathbf{a} = \int_0^\infty dt \int_V e^{t\hat{D}}\delta(\mathbf{a} - \mathbf{a}_0). \tag{7.3.7}$$

To perform the integration over $\mathbf{a}$ we do the following

$$\tau(\mathbf{a}_0) = \int_0^\infty dt \int_V e^{t\hat{D}}\delta(\mathbf{a} - \mathbf{a}_0) = \int_0^\infty dt \int_V \delta(\mathbf{a} - \mathbf{a}_0)e^{t\hat{D}^\dagger} = \int_0^\infty e^{t\hat{D}^\dagger}dt. \tag{7.3.8}$$

Since the delta function replaces $\mathbf{a}$ with $\mathbf{a}_0$, we can drop the subscript and notice

$$\hat{D}^\dagger\tau(\mathbf{a}) = \int_0^\infty \hat{D}^\dagger e^{t\hat{D}^\dagger}dt = \int_0^\infty \frac{d}{dt}e^{t\hat{D}^\dagger}dt = -1 \tag{7.3.9}$$

where the upper bound vanishes due to absorbing boundary conditions. Finally, the equations governing $\tau(\mathbf{a})$ are

$$\hat{D}^\dagger\tau(\mathbf{a}) = -1 \tag{7.3.10}$$

with the boundary conditions given by

$$\tau(\mathbf{a}) = 0, \qquad \mathbf{a} \in \partial V \tag{7.3.11}$$

which is due to the original absorbing boundary conditions on $\langle \rho(\mathbf{a}, 0)\rangle$. Solving Eq. 7.3.10 for general cases is difficult, so we will consider important 1D scenarios.

7.3.2 Overdamped limit

Let us consider the two variable Langevin equation of a particle, where our variables are x and p. Then our equations are

$$\frac{dx}{dt} = \frac{p}{m} \tag{7.3.12}$$

$$\frac{dp}{dt} = -\frac{d}{dx}U(x) - \gamma\frac{p}{m} + \eta(t) \tag{7.3.13}$$

where $U(x)$ is the potential felt by the particle and $\eta(t)$ is the Gaussian noise. The corresponding FP equation is

$$\frac{\partial}{\partial t}\langle\rho(\mathbf{X},t)\rangle = \left[-\frac{\partial}{\partial x}\frac{p}{m}+\frac{\partial}{\partial p}\Big(\frac{d}{dx}U(x)+\gamma\frac{p}{m}\Big)+\gamma k_B T\frac{\partial^2}{\partial p^2}\right]\langle\rho(\mathbf{X},t)\rangle \tag{7.3.14}$$

where $\mathbf{X} = (x,p)$. We can approximate Eq.7.3.14 in the high friction limit by noticing the following

$$\left|\frac{\partial p}{\partial x}\right| = \frac{\left|\frac{\partial p}{\partial t}\right|}{\left|\frac{\partial x}{\partial t}\right|} = \left|\frac{-\frac{d}{dx}U(x) - \gamma\frac{p}{m} + \eta(t)}{\frac{p}{m}}\right| \approx \gamma \tag{7.3.15}$$

where we assume $m/\gamma \ll 1$, which physically means that the relaxation time to fluctuations of the particle is small. Then, interchanging derivatives, Eq. 7.3.14 becomes

$$\begin{aligned}\frac{\partial}{\partial t}\langle\rho(x,t)\rangle &= \left[\frac{1}{\gamma}\frac{\partial}{\partial x}\frac{d}{dx}U(x) + \frac{k_B T}{\gamma}\frac{\partial^2}{\partial x^2}\right]\langle\rho(x,t)\rangle \\ &= \frac{k_B T}{\gamma}\frac{\partial}{\partial x}e^{\frac{-U(x)}{k_B T}}\frac{\partial}{\partial x}e^{\frac{U(x)}{k_B T}}\langle\rho(x,t)\rangle\end{aligned} \tag{7.3.16}$$

which is known as the Smoluchowski equation (or limit). We can construct a similar equation for τ by taking the adjoint of the RHS to yield

$$\frac{k_B T}{\gamma}e^{\frac{U(x)}{k_B T}}\frac{\partial}{\partial x}e^{\frac{-U(x)}{k_B T}}\frac{\partial}{\partial x}\tau(x) = -1. \tag{7.3.17}$$

This equation can be solved by quadrature and results in

$$\tau(x) = \frac{\gamma}{k_B T}\int_x^b e^{\frac{U(y)}{k_B T}}dy\int_a^y e^{\frac{-U(z)}{k_B T}}dz \tag{7.3.18}$$

where a and b is the bottom of the potential well and the absorbing barrier, respectively.

7.3.3 Underdamped limit

A particle governed by Eq. 7.3.12 and Eq. 7.3.13, in an environment with a low friction implies that energy is conserved. Therefore it will be more illuminating to consider the probability distribution on the energy domain rather than the typical xp phase space. Since the relaxation time ($\approx 1/\gamma$) is slow, we will simply write[80] and forgo the derivation for the following FP equations

$$\frac{\partial}{\partial t} f(\mathbf{X}, t) = \left[\hat{L}_0 + \gamma \hat{L}_1\right] f(\mathbf{X}, t) \tag{7.3.19}$$

with

$$\hat{L}_0 = -\frac{p}{m}\frac{\partial}{\partial x} + \frac{d}{dx}U(x)\frac{\partial}{\partial p} \tag{7.3.20a}$$

$$\hat{L}_1 = \frac{p}{m}\frac{\partial}{\partial p} + k_B T \frac{\partial^2}{\partial p^2} \tag{7.3.20b}$$

where $f(\mathbf{X}, t) \equiv \langle \rho(\mathbf{X}, t) \rangle$. To use perturbation theory beyond small t, let us consider the time scale to be slow or $t = \gamma t$ and hence write

$$\frac{\partial}{\partial t} f(\mathbf{X}, t) = \left[\frac{1}{\gamma}\hat{L}_0 + \hat{L}_1\right] f(\mathbf{X}, t). \tag{7.3.21}$$

Next, consider a power series expansion in γ

$$f(\mathbf{X}, t) = \sum_{n=0}^{\infty} \gamma^n f_n(\mathbf{X}, t) \tag{7.3.22}$$

Then, after equating terms with equal powers of γ in Eq. 7.3.21 we arrive at

$$\hat{L}_0 f_0(\mathbf{X}, t) = 0 \tag{7.3.23a}$$

$$\hat{L}_0 f_1(\mathbf{X}, t) = -\hat{L}_1 f_0(\mathbf{X}, t) + \frac{\partial}{\partial t} f_0(\mathbf{X}, t) \tag{7.3.23b}$$

where we have dropped higher order terms.[82] To solve the matched equations notice the following property

$$\hat{L}_0 H(\mathbf{X}) = 0 \tag{7.3.24}$$

where

$$H(\mathbf{X}) = H(x, p) = \frac{p^2}{2m} - U(x) \equiv E \tag{7.3.25}$$

and solvability condition (constraint to avoid secular solutions)[83]

$$\int \hat{L}_0 f(\mathbf{X},t)F(H(\mathbf{X}))d\mathbf{X} = f(\mathbf{X},t)F(H(\mathbf{X}))\Big|_{-\infty}^{\infty} - \int f(\mathbf{X},t)\hat{L}_0 F(H(\mathbf{X}))d\mathbf{X}$$
$$= -\int f(\mathbf{X},t)\hat{L}_0 F(H(\mathbf{X}))d\mathbf{X} = 0 \tag{7.3.26}$$

where $F(H)$ is a continuous function that decays to 0 as $|p| \to \infty$. This implies that Eq. 7.3.23b must satisfy

$$\int \Big[\hat{L}_1 f_0(\mathbf{X},t) - \frac{\partial}{\partial t} f_0(\mathbf{X},t)\Big] F(H(\mathbf{X}))d\mathbf{X} = 0 \tag{7.3.27}$$

To obtain an equation for the distribution as a function of the energy we want to be able to exchange $\mathbf{X}$ and ∂_p to E and ∂_E, respectively. To proceed consider the following relationships

$$\frac{\partial f}{\partial p} = \frac{\partial E}{\partial p}\frac{\partial f}{\partial E} = \frac{p}{m}\frac{\partial f}{\partial E} \tag{7.3.28}$$

and

$$\frac{\partial^2 f}{\partial p^2} = \frac{\partial}{\partial p}\frac{\partial f}{\partial E} = \frac{\partial f}{\partial E} + \Big(\frac{p}{m}\Big)^2 \frac{\partial^2 f}{\partial E^2}. \tag{7.3.29}$$

Then Eq. 7.3.20b can be written as

$$\int\int \Big[\frac{\partial}{\partial t} - \Big(k_B T - \frac{p^2}{m^2}\Big)\frac{\partial}{\partial E} - k_B T \frac{p^2}{m^2}\frac{\partial^2}{\partial E^2}\Big] f(E,x,t)F(E)\frac{m}{p}dxdE = 0 \tag{7.3.30}$$

where we have used $dp = \frac{m}{p}dE$ from Eq. 7.3.25. To absorb the integration over x we take a page from classical mechanics and define the following action-angle variables

$$I(E) = \int p(E,x)dx \tag{7.3.31}$$

and

$$\omega(E) = 2\pi\Big(\frac{\partial I}{\partial E}\Big)^{-1} = 2\pi\Bigg[\int \frac{\partial p(E,x)}{\partial E}dx\Bigg]^{-1} = 2\pi m\Bigg[\int \frac{1}{p(E,x)}dx\Bigg]^{-1}. \tag{7.3.32}$$

Then observing that for Eq. 7.3.30 to be 0 for an arbitrary function $F(E)$ the term in the bracket needs to be equal to 0 and we can write

$$\frac{\omega(E)}{2\pi}\frac{\partial}{\partial t}f(E,t)-\left(k_BT\frac{\omega(E)}{2\pi}-\frac{I(E)}{m}\right)\frac{\partial}{\partial E}f(E,t)-k_BT\frac{I(E)}{m}\frac{\partial^2}{\partial E^2}f(E,t)=0 \tag{7.3.33}$$

which after rescaling back t results in

$$\frac{\partial}{\partial t}\langle\rho(E,t)\rangle=\frac{\gamma}{m}\frac{\partial}{\partial E}I(E)\left(1+k_BT\frac{\partial}{\partial E}\right)\frac{\omega(E)}{2\pi}\langle\rho(E,t)\rangle \tag{7.3.34}$$

the FP equation in the Freidlin-Wentzell limit.[84]

Finally, to obtain τ we use the same technique as before, which is to take the adjoint of the RHS in Eq. 7.3.34 and set it equal to -1. After some manipulation,[80] this yields

$$\tau(E)=\frac{m}{2\gamma k_BT}\int_E^{E_b}\frac{e^{E'/k_BT}}{I(E')}dE'\int_0^{E'}\frac{\omega(E'')}{2\pi}e^{-E''/k_BT}dE'' \tag{7.3.35}$$

where E_b is the energy at the absorbing boundary (barrier).

7.4 Applications

Stochastic mechanics can be applied to a variety of problems ranging from physics to biology and even finance. In fact, Einstein's mathematical description of the Brownian particle is predated by Bachelier's thesis on the stock market, which was later used as a springboard by Kolmogorov. In this section we will explain how we can use the equations previously derived to work out idealized systems.

7.4.1 Hysteresis

Hysteresis can be broadly understood as an overshoot phenomena, where a system responds, relative to the rate of transitions between its states, to a time dependent perturbation. For a uniaxial ferroelectric material, we typically present its states, within the Landau framework, as a free energy surface defined by the double well potential

$$\Phi(P,t)=\frac{1}{4}bP^4-\frac{1}{2}aP^2-E(t)P \tag{7.4.1}$$

and

$$E(t) = E_0 + E_\omega t \tag{7.4.2}$$

where E_0 and E_ω is the built-in bias and sweep rate of the electric field, respectively. Here the coupling between the time dependent electric field and the polarization is the perturbation that leads to the transition between the stable and metastable state.

Modeling the hysteresis involves determining the probability distribution ρ of a successful transition at $E(\tau)$, where τ is the mean first passage time (MFPT), the average time needed for one state to transition into the other. For $E_\omega = 0$, the MFPT can be approximated, in the overdamped limit, by quadrature to be

$$\tau(P;E) = \frac{1}{D}\int_P^{P_b} dP' e^{\Phi(P')/D} \int_{P_m}^{P'} dP'' e^{-\Phi(P'')/D}, \qquad P_b > P_m \tag{7.4.3}$$

where D, P_b and P_m is the diffusion constant, the polarization at the barrier and the polarization at the local minimum we start in, respectively. When $E_\omega \neq 0$ it turns out that τ and likewise ρ cannot be calculated by quadrature because the bounds, P_b and P_m, now have a time dependence, which is equivalent to having time independent bounds, but at the cost of a multidimensional τ.[85]

Instead we consider the sweeping field to be a series of successive ”microsteps” such that

$$E(\tau) \equiv E_n = E_0 + E_\omega n\Delta \tag{7.4.4}$$

where Δ is the time step connecting rapidly equilibrated states, whose value does not influence the results. Under such an approximation,[86] we can write an iterative solution for the probability distribution as

$$\rho(E(\tau)) \equiv \rho(E_n) = \Big[1 - \sum_i^{n-1} \rho(E_i)\Delta\Big] \frac{e^{-\Delta/\tau(P_m;E_n)}}{\tau(P_m;E_n)}. \tag{7.4.5}$$

We emphasize that the approximation breaks down when E_0 is near the transition where Φ has a single well. Finally, we can write the polarization, normalized to its maximum magnitude, as

$$P(E(\tau)) = 1 - 2\int_{E(\tau)}^{E_0} \rho(E')dE' \tag{7.4.6}$$

which gives the upper branch of the hysteresis loop, with the lower branch given by recalculating τ when P_b is less than P_m and the sign of E_ω is reversed.

Part II

Results and Discussion

8 Bulk $PbTiO_3$

8.1 Introduction

Ferroelectric perovskites, with chemical formula ABO_3, have a wide range of applications and serve an important role in data storage, being good candidates for non-volatile memory devices.[87] However, even in ideal growth conditions, the devices present atomic defects or impurities, which affect their electronic properties. Among the standard problems associated to the presence of these defects are ferroelectric fatigue and up-down asymmetry (sometimes referred to as imprint)[14] are the two most commonly discussed. Fatigue is the decrease in magnitude of the polarization after repeated switching between the two polarization states, and up-down asymmetry is when one polarization state is easier to switch than the other. The problem of fatigue has been extensively studied [88, 89, 90] and can be well explained by local distortions of oxygen octahedra caused by charged oxygen vacancies which result in domain wall pinning. Although other, more complex, interactions have been proposed.[91]

The problem of up-down asymmetry is much more nuanced. The existence of a preferred polarization state is observed in experiments as a voltage (or field) shift of the hysteresis loop. The proposed origin of this effect is the presence of dipolar defects (DDs).[92, 93] The dipole moments of the DDs produce an electric field that changes the relative energy between the two spontaneous polarization states through the $\mathbf{E} \cdot \mathbf{P}$ term in the free energy of the ferroelectric.

Typically, these DDs are created from a charged oxygen vacancy and a Pt_{Ti} impurity created from the diffusion of the metal electrode atoms into the ferroelectric perovskite lattice.[94, 14] However, there is no actual detailed understanding about of how the net alignment of DDs affects the electric field contribution to the free energy of the ferroelectric. In particular, disagreement exists on whether the electric field produced from the DDs is a constant electric field always built-in the material[95] or a transient electric field only present when the polarization of ferroelectric is near the spontaneous polarization.[96, 97] Recently, it has been observed that these types of DDs are present even in the absence of bulk metal electrodes and the hysteresis could not be explained using transient electric fields (See Sec. 9.3.3.2).

In this work we model the dipolar defect problem using phenomenological theory and electrostatics to understand how the $\mathbf{E} \cdot \mathbf{P}$ term in the free energy is responsible for the up-down polarization asymmetry observed in ferroelectrics. Then, using atomistic density functional theory (DFT) simulations we attempt to validate the model's results, in addition to, providing new insights into the problem. While the focus of this work is on DDs which are formed from an oxygen anion and an A cation vacancy pair, the methodologies are readily applicable to DDs which are formed from any type of impurities.

8.2 Phenomenological theory

The collective interaction of DDs alter the switching in ferroelectrics by creating an electric field $\mathbf{E}_{DD}$ which modifies the free energy. (See Fig. 7a and Fig. 7b). Many different phenomenological models exist for exploring defects in ferroelectric materials.[98] We model the defects in the ferroelectric using Landau-Ginzburg-Devonshire theory (LGDT).[19] In the model, the defects exist in a planar interface, normal to the direction of spontaneous polarization, within a uniaxial ferroelectric material and couple to the local polarization of the ferroelectric at the interface. The main advantage to this method is a straightforward approach, within a mean field theory, to control the defect concentration and coupling to the ferroelectric. The main disadvantage to this method is the coupling between different interfaces of defects is missing, however this can be recovered by considering multiple interfaces.[99]

8.2.1 Landau-Ginzburg-Devonshire Theory

We consider a uniaxial ferroelectric, which is only polarized along the z direction, and whose in-plane spatial variation is averaged, such that $1/S \int P_z(x, y, z) dxdy \equiv P(z)$, where S is the surface area. Therefore the system can be fully characterized by a one-dimensional periodic cell, in the z direction, of length L.

Then, the free energy, to 6th order in the polarization, (cf. Ref [3, 99]) is

$$F = \int_0^L \left[\frac{1}{2}\left(A + \frac{1}{\epsilon}\right) P^2 + \frac{1}{4}BP^4 + \frac{1}{6}CP^6 + \frac{1}{2}D\left(\frac{\partial P}{\partial z}\right)^2 \right] dz - \frac{1}{2\epsilon L^2}\left[\int_0^L P dz\right]^2 \tag{8.2.1}$$

where the constants, chosen for the ubiquitous ferroelectric perovskite $\mathrm{PbTiO_3}$ at $T = 300\mathrm{K}$, are given in Table 1.[100]

The defect is introduced at the periodic cell boundary. This creates an interface, whose energetics are sensitive to the direction of polarization due to local dipole moments of the defects. In addition, the presence of defects should partially weaken the ferroelectric coupling between neighboring $\mathrm{PbTiO_3}$ unit cells across the interface. Therefore we can write the free energy at the interface to be

$$\begin{aligned} F_I = & \frac{D}{2\delta}\left[P(0)^2 + P(L)^2\right] + \frac{D^2}{2\delta'}\left[P(0)^4 + P(L)^4\right] - \xi P(0)P(L) \\ & - \eta\left[P(0)^3 P(L) + P(0)P(L)^3\right] - \alpha_1 P(0) - \alpha_2 P(L) \end{aligned} \tag{8.2.2}$$

where the constants are given in Table 1 and the interfacial coupling constants ξ and η are the same as in Ref. [3] and taken to be 1.2 and 0.18, respectively. Here α_1 and α_2 are the coefficients coupling the polarization to the left and right surfaces of the defect interface, respectively. Specifically for a DD, α_1 and α_2 physically represent the coupling of the tail and head of the DD with the left and region, respectively and therefore are chosen to be equal and opposite. The contribution from the DD electric field E_{DD} modifies Eq. 8.2.1 by an additional term in the integral, $E_{DD}P$. Finally, we note that the free energy coefficients can be renormalized due to the lattice strain by the defects.[101]

8.2.2 Euler-Lagrange equations

We can calculate the polarization profile by minimizing the total free energy $F + F_I$ to obtain the following Euler-Lagrange (EL) equation

$$D\frac{d^2P}{dz^2} - AP - BP^3 - CP^5 + \frac{1}{\epsilon}\left(\langle P\rangle - P\right) + E = 0 \tag{8.2.3}$$

where

$$\langle P\rangle = \frac{1}{L}\int_0^L P dz \tag{8.2.4}$$

is the average polarization. We note that E can include an external electric field in addition to E_{DD}. The corresponding Robin boundary conditions (cf. Ref [3]) are

$$\begin{aligned} -D\frac{dP}{dz}\bigg|_{z=0} &+ \frac{D}{\delta}P(0) + \frac{2D^2}{\delta'}P(0)^3 - \xi P(L) - \alpha_1 \\ &- 3\eta P(0)^2 P(L) - \eta P(L)^3 = 0 \end{aligned} \tag{8.2.5a}$$

$$\begin{aligned} D\frac{dP}{dz}\bigg|_{z=L} &+ \frac{D}{\delta}P(L) + \frac{2D^2}{\delta'}P(L)^3 - \xi P(0) - \alpha_2 \\ &- 3\eta P(0) P(L)^2 - \eta P(0)^3 = 0. \end{aligned} \tag{8.2.5b}$$

In the case when $\alpha_1 = 0$ and $\alpha_2 = 0$ we have standard periodic boundary conditions

$$P(0) = P(L) \tag{8.2.6a}$$

$$\frac{dP}{dz}\bigg|_{z=0} = \frac{dP}{dz}\bigg|_{z=L}. \tag{8.2.6b}$$

For computational efficiency[102] we use the following reduced variables

$$A^* = \frac{A}{|A_0|}, \quad B^* = \frac{BP_s^2}{|A_0|}, \quad C^* = \frac{BP_s^4}{|A_0|}, \quad D^* = \frac{D}{D_0}$$

$$\epsilon^* = \epsilon|A_0|, \quad \alpha_1^* = \frac{\alpha_1}{|P_s A_0|}, \quad \alpha_2^* = \frac{\alpha_2}{|P_s A_0|}, \quad E^* = \frac{E}{|P_s A_0|} \tag{8.2.7}$$

where P_s, A_0 and D_0 is the spontaneous polarization, A evaluated at 300K and $D/2$, respectively, whose values are given in Table 1. We note that the scaling constants $|A_0|$ and D_0 were chosen in such a way that the unit of length $\sqrt{D_0/|A_0|}$ is 1.0 nm. We solve the coupled EL equations, with their boundary conditions, applying a finite difference method on a discrete grid of z points, where the integral in $\langle P \rangle$ is evaluated using trapezoidal quadrature. In our calculations every two grid points physically corresponds to a $PbTiO_3$ unit cell. We set $L = 10a$, where a is the lattice constant of $PbTiO_3$, because this is the minimum number of unit cells required to stabilize both polarization directions for varying α_1^*, α_2^* and E^*. Using Broyden's method,[21] we randomly initialize the polarization on the grid from a Gaussian distribution centered at P_s, then iteratively find the eigenvectors of the system which yield the polarization profile.

8.2.3 Polarization kinetics

In the most general case, a kinetic model of the one-dimensional polarization will assume

$$\frac{\partial P}{\partial t} = \Gamma[P] \tag{8.2.8}$$

where Γ is some partial differential operator.[103] From a thermodynamic viewpoint Eq. 8.2.8 is restricted by the second law[104] which requires

$$\frac{dF}{dt} + \frac{dJ}{dz} \leq 0 \tag{8.2.9}$$

where F and J is the free energy and free energy current, respectively. If we assume that $J = 0$ then it is easy to verify[103] that the simplest $\Gamma[P]$ that satisfies Eq. 8.2.9 is

$$\Gamma[P] = -l_1 \frac{\partial F}{\partial P} \tag{8.2.10}$$

where l_1 is a positive constant, we define as the first polarization conductivity coefficient. We note that Eq. 8.2.10 associates temporal changes in the polarization with changes in the free energy. Inserting Eq. 8.2.10 into Eq. 8.2.8 yields the Landau-Khalatnikov transport equation[105] (sometimes called the bistable diffusion equation) which is typically used for calculating dynamical properties in ferroelectric materials.[106, 107]

However, let us examine the case when $J \neq 0$. Since we associated temporal changes in the polarization with changes in the free energy, let us assume for simplicity that $J \propto \partial P/\partial t = \Gamma$. From Eq. 8.2.9 this assumption yields[108]

$$\Gamma[P] = -l_1 \frac{\partial F}{\partial P} - l_2 \frac{\partial}{\partial z} l_1 \frac{\partial^2 P}{\partial z \partial t} \tag{8.2.11}$$

where l_2 is a positive constant, we define as the second polarization conductivity coefficient. Notice that a non-zero free energy current produced an additional term in Γ. Because the additional term is typically neglected in kinetic calculations of polarization we assume, and later computationally verify, that $l_1 \gg l_2$ for conventional ferroelectrics.

Using this time-dependent Landau theory we can model the polarization kinetics, under a periodic external electric field, to calculate the hysteresis curve. Using Eq. 8.2.1, Eq. 8.2.8 and Eq. 8.2.11 yields the time evolution of the polarization

$$-\frac{\partial P}{\partial t}-l_1\left[D\frac{\partial^2 P}{\partial z^2}-AP-BP_1^3-CP^5+\frac{1}{\epsilon}\left(\langle P\rangle-P\right)+E(t)\right]-l_1 l_2\frac{\partial^3 P}{\partial z^2\partial t}=0 \tag{8.2.12}$$

where

$$E(t)=E_{\text{ext}}(t)+E_{DD}=E_{\text{ext}}\sin\left(2\pi f t\right)+E_{DD} \tag{8.2.13}$$

and E_{ext}, f, E_{DD}, l_1 and l_2 is magnitude of the external electric field, frequency of the external field and DD electric field, respectively. To our knowledge this is the first instance the second conductivity coefficient is included in ferroelectric calculations. For computational efficiency the reduced variables that we employ are

$$t^*=|A_0|l_1 t,\quad E^*_{\text{ext}}=\frac{E_{\text{ext}}}{|P_s A_0|},\quad f^*=\frac{f}{|A_0|l_1},\quad E^*_{DD}=\frac{E_{DD}}{|P_s A_0|}.$$

In addition, for the last term, we can rewrite the reduced time as $t^*=\lambda t D_0/l_2$, where $\lambda=l_1 l_2|A_0|/D_0$ is a dimensionless constant. This change of variables scales t and l_2 by l_1, allowing us to eliminate l_1 from the equation. The solutions to Eq. 8.2.12 are initialized at $t^*=0$ to a random Gaussian spatial distribution centered at $P=0$ and subject to the same spatial Robin boundary conditions, as before, for all t^*. We solve Eq. 8.2.12 iteratively using the implicit Euler method,[109] where, at each iteration, the system of equations is solved using Broyden's method. The constants Δt^*, E^*_{ext}, f^*, and λ are set to 0.1, 6.0, 0.1 and 0.01, respectively,

8.3 Density functional theory

To explicitly verify our phenomenological results we perform numerical experiments on bulk $PbTiO_3$ using density functional theory. First, to purely understand what role the $\mathbf{E}\cdot\mathbf{P}$ term has on the up-down polarization asymmetry, we perform finite field DFT simulations on pristine $PbTiO_3$ without any defects. Second, to model DDs, we consider a V_{Pb}-V_O vacancy pair in a supercell of $PbTiO_3$. Then, using the modern theory of polarization[**?**] we can calculate polarization profiles to assess the accuracy of our phenomenological model.

In addition, studies on the effects of DD in ferroelectrics perovskites have been limited to the cubic phase of the material.[14, 110] Therefore, we explore the energetics and structural relaxations of $PbTiO_3$ as a function of the defect density.

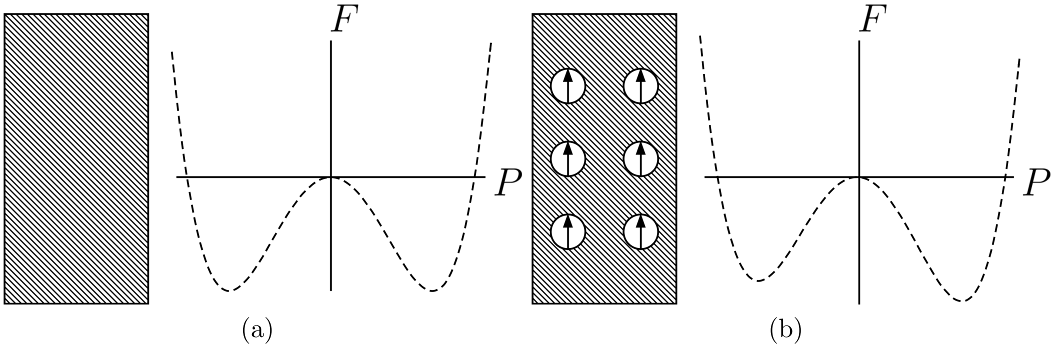

(a) (b)

Figure 7: Schematic representation of a double well potential of the free energy with respect to the polarization in a ferroelectric that is (a) pristine or (b) with dipolar defects.

$A(10^5$ C^{-2} m^2 N$)$	$3.8 \times (T - 752)$
$B(10^7$ C^{-4} m^6 N$)$	-7.3
$C(10^8$ C^{-6} m^{10} N$)$	2.6
$D(10^{-10}$ C^{-2} m^4 N$)$	3.44
$\epsilon(10^{-10}$ C^2 m^{-2} N$^{-1})$	4.43
$P_s($C m$^{-2})$	0.757
$A_0(10^8$ C^{-2} m^2 N$)$	-1.72
$D_0(10^{-10}$ C^{-2} m^4 N$)$	1.72
a(nm)	0.3904
δ(nm)	0.3904
δ'(nm)	∞

Table 1: Free energy coefficients and other material constants for $PbTiO_3$ in SI units and T in K.

8.3.1 Computational details

We perform simulations using LAUTREC, an in-house code, utilizing the projector augmented wave (PAW) scheme.[48] The exchange-correlation functional used was PW92[111] and the Brillouin zone was sampled for $PbTiO_3$, with and without a $V_{Pb\text{-}O}$, using a $2 \times 2 \times 1$ and $4 \times 4 \times 4$ Monkhorst-Pack mesh,[50] respectively, with a plane wave cutoff energy of 160 Ry. We initialize the system in the P4mm space group, where the Ti and O atoms in the TiO_2 planes are displaced, in opposite directions, along the [001] (out-of-plane) axis, from their ideal P4/mmm space group positions. We perform finite electric field calculations for bulk $PbTiO_3$ using the scheme of Ref. [58] which minimizes the electric enthalpy. We simulate $4 \times 2\sqrt{2} \times 2\sqrt{2}$, $9 \times 2\sqrt{2} \times 2\sqrt{2}$, and $4 \times 3\sqrt{2} \times 3\sqrt{2}$ $PbTiO_3$ supercells with a single V_{Pb}-V_O vacancy pair, whose defect densities are referred to as n, $n_{\|}$ and $n_{\perp}$, respectively. We emphasize that $n_{\|}$ and $n_{\perp}$ have the same volumetric density of defects, but the linear density is more dilute in the parallel and perpendicular direction relative to the spontaneous polarization, respectively. (See Fig. 8) The V_{Pb}-V_O vacancy pair is formed by removing a Pb atom in a PbO plane and the O atom in the adjacent TiO_2 plane so that the vacancy pair dipole moment is in the [101] axis. Due to computational costs we only simulate a single V_{Pb}-V_O vacancy pair, however, using electrostatics (see Appendix C.3) we verify that multiple V_{Pb}-V_O vacancy pairs, with different orientations, but the same defect density, are not, any more energetically favorable. The valence electrons explicitly treated for Pb, Ti and O were $6s^2 5d^{10} 6p^2$, $3s^2 3p^6 4s^2 3d^2$ and $2s^2 2p^4$, respectively. The lattice constants, a and c, were fixed to 3.854Å and 4.024Å, respectively,[112] while the force tolerance, for atomic relaxations, was 0.08 eV/Å.

8.3.2 Oxygen octahedra rotations

Even for bulk equilibrium lattice constants it is known that oxygen octahedra tilts and rotations are present in $PbTiO_3$ under an applied field.[113] Hence it is sensible to consider that such relaxations will occur when a V_{Pb}-V_O vacancy pair is present. Since we do not enforce any symmetry constraints during relaxation, each octahedra rotation in the supercell will have some spatial variation. Therefore we define the average planar octehdra rotation

$$\bar{\mathbf{R}}^{\alpha} = \frac{1}{N} \sum_j \underset{\mathbf{R}_j^{\alpha}}{\arg\min} \sum_i |\mathbf{x}_{ij} - \mathbf{R}_j^{\alpha} \cdot \mathbf{x}_{ij}^0|^2 \tag{8.3.1}$$

where N, $\mathbf{R}_j^\alpha$, $\mathbf{x}_{ij}$, and $\mathbf{x}_{ij}^0$ is the number of oxygen octahedra in the plane, the rotation tensor around the α^{th} axis for the j^{th} oxygen octahedra, the relaxed coordinates of the i^{th} oxygen atom in the j^{th} oxygen octahedra of the plane, and the initial coordinates of the i^{th} oxygen atom in the j^{th} oxygen octahedra of the plane, respectively. We take the rotation axes to be the crystallographic directions.

8.3.3 Polarization calculation

We calculate the polarization using hybrid Wannier functions,[30] only localized in the direction of the c axis. Then we define the average planar polarization

$$\bar{P} = \frac{1}{N_k}\sum_{\mathbf{k}}\left[\sum_{\alpha} Q_\alpha (X_\alpha - \bar{X}) - 2e\sum_i (x_{i\mathbf{k}} - \bar{X}_l) - 2e\sum_i x_i^{EV} + Q_{\mathbf{k}}\bar{X}\right] \tag{8.3.2}$$

and

$$Q_{\mathbf{k}} = \sum_\alpha Q_\alpha - 2eN \tag{8.3.3}$$

$$\bar{X} = \frac{1}{N}\sum_\alpha X_\alpha \tag{8.3.4}$$

where the indexes α, i, k run over atoms in the plane, Wannier orbitals in the plane, and k-points, respectively. Q_α and X_α are the ion core charges and the position of the α^{th} atom, N is the number of atoms in the layer, $x_{i\mathbf{k}}$ is the position of the Wannier center of the i, k Wannier orbital, and N_k is the number of k-points. The third term on the RHS of Eq. 9.2.1 is the contribution to the polarization due to the use of PAWs.[114]

8.4 Results

To systematically study the free energy of the ferroelectric-DD complex we vary the interfacial and bulk coupling strengths (α^* and E^*, respectively) to determine how they effect a realistic system. The polarization profile of the intuitive picture, where the DD only couples to the bulk polarization (low interfacial coupling limit), is shown in Fig. 9a. We find that when the $-\mathbf{E}_{DD}\cdot\mathbf{P}$ term is negative, the average polarization increases with an increasing E_{DD}, but when the term is positive there is only a constant decrease in the average

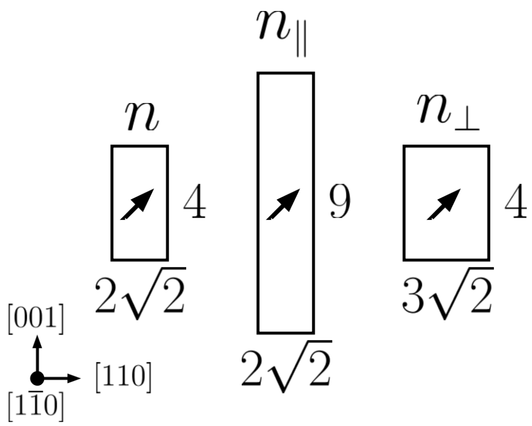

Figure 8: Schematic representation of the different supercells and their associated defect densities. Here the numbers represent the amount of unit cells in a particular dimension. Both $n_{\parallel}$ and $n_{\perp}$ have the same supercell volume. The black arrow represents the dipole moment of the $\mathrm{V_{Pb}}$-$\mathrm{V_O}$ vacancy pair, along the [101] axis, in the supercell.

polarization, regardless of the E_{DD} strength. To reduce the energy cost of a positive $-\mathbf{E}_{DD} \cdot \mathbf{P}$ it is more favorable for the system to stay in a specific weakly polarize state than transition into a non-polar state. As expected, we also observe that the polarization profile at the interface is insensitive to the sign of α^{*}.

The polarization profile for the low bulk coupling limit is shown in Fig. 9b. We find a decrease in the magnitude of the average polarization when interfacial coupling is present because the long range coupling of the ferroelectric is broken by the interface. In addition, the $-\alpha P$ term in the free energy causes the polarization at the interface to decrease significantly when the sign of α^{*} and the average polarization are opposite.

Finally, for a realistic system, where both interfacial and bulk coupling constants are large, the polarization profile is shown in Fig. 9c. By inspection we can approximate this polarization profile to be a linear combination of the polarization profiles in the low interfacial and low bulk coupling limits discussed previously. The origin of why this approximation is valid is because the total free energy is a linear combination of interfacial and bulk free energies.

Although the polarization profile is sensitive to the interfacial terms in the free energy, the kinetic calculations, shown in Fig. 11a, reveal that only the details of the bulk coupling determine the shift and shape of the hysteresis. However, it is interesting to note that by varying α and λ, shown in Fig. 10, we are able to induce phase transitions in the ferroelectric. For sufficiently strong interfacial coupling the system becomes paraelectric-like, shown in Fig. 11b, where $E^* = 0$ is taken for clarity. In addition, for sufficiently large λ, potentially created by defects, the system becomes dielectric as shown in Fig. 11c. An interesting note, for a critical value $\lambda \approx 0.073$ the system loses its ferroelectric properties even without bulk and interfacial coupling terms in the free energy. This suggests that defect engineering in perovskite oxides can create ferroelectric-paraelectric or ferroelectric-dielectric transitions.

To validate the LGDT results using first principles simulations we compute the out-of-plane polarization profiles when $PbTiO_3$ is subject to an out-of-plane applied external electric field, shown in Fig. 12a, and a V_{Pb}-V_O vacancy pair, shown in Fig. 12b. We find that the applied external field affects both spontaneous polarizations in the same way, unlike the LGDT results, which were dependent on the sign of $-\mathbf{E}_{DD} \cdot \mathbf{P}$. We attribute this to the stability of the polar state caused by the hybridization between the Ti 3d and O 2p orbitals, and also the Pb 6s, Pb 6s and O 2p orbitals.[8] Comparing the polarization profiles of the finite field and the V_{Pb}-V_O vacancy pair, we find large deviations specifically near the defect site. However, there is good agreement between LGDT and DFT polarization profiles showing the correct polarization behavior at the defect site when the sign of α and the vacancy charge match. This strongly implies that while the LGDT does not account for the in-plane component of the DD dipole moment, including this contribution in the free energy is not essential in reproducing the out-of-plane polarization. We note that when $-\mathbf{E}_{DD} \cdot \mathbf{P}$ is negative, the magnitude of the average polarization is higher in the DFT calculations, which we attribute to not including higher order coupling terms, in the free energy, between adjacent unit cells across the interface. We conclude that to properly explain the ferroelectric-DD complex, considering only coupling of the bulk polarization to the DD electric field is insufficient and must be amended to include coupling of the local polarization at the DD site.

To better understand the differences between the defect concentrations we calculate the free energy surface, which is obtained by linearly interpolating the atomic coordinates between the two polarization states and computing their total energies. The asymmetrical double well, shown in Fig. 13a, is commensurate with the hysteresis obtained from LGDT. In addition, our first principles results reveal necessary considerations when formulating the up-down asymmetry caused by DDs. First, the notion that the defect concentration is a uniform bulk property effecting the ferroelectric is erroneous. The total energies, shown in Fig. 13b, reveal that while the energy barrier is insensitive to the directional density of the defects, the up-down asymmetry is stronger for $n_{\parallel}$ than $n_{\perp}$, suggesting that directional defect control can be an interesting venue to reduce the asymmetry. Second, we find local oxygen octahedra rotations that couple to the dipole moment of the V_{Pb}-V_O vacancy pair as shown in Fig. 14. This is clearly seen from the average planar oxygen rotations for different defect concentrations, shown in Fig. 15. The magnitudes of oxygen rotations only decrease for $n_{\perp}$ due to the decrease in the defect concentration within those planes. In addition, we find that the oxygen rotations are independent of the bulk polarization direction and vanish within two unit cells, in the out-of-plane direction, from the vacancy pair. Our results suggest that dipolar defects can be used to locally activate oxygen rotations in ferroelectric materials.

8.5 Conclusion

The up-down asymmetry observed in ferroelectrics perovskites is a combination of bulk polarization coupling to the constant electric field produced by dipolar defects and local polarization coupling at the defect site. While the bulk coupling is able to reproduce the correct shifted hysteresis, local coupling is needed to accurately capture the polarization profile in the ferroelectric. We also found oxygen octahedra rotations which couple to the local polarization distortions created by the defects, suggesting a three parameter phenomenological model is more appropriate to capture the corresponding physics. Varying the degree of defect coupling and defect concentration it may be possible to engineer a dielectric, or a paraelectric phase from a simple ferroelectric perovskite oxide.

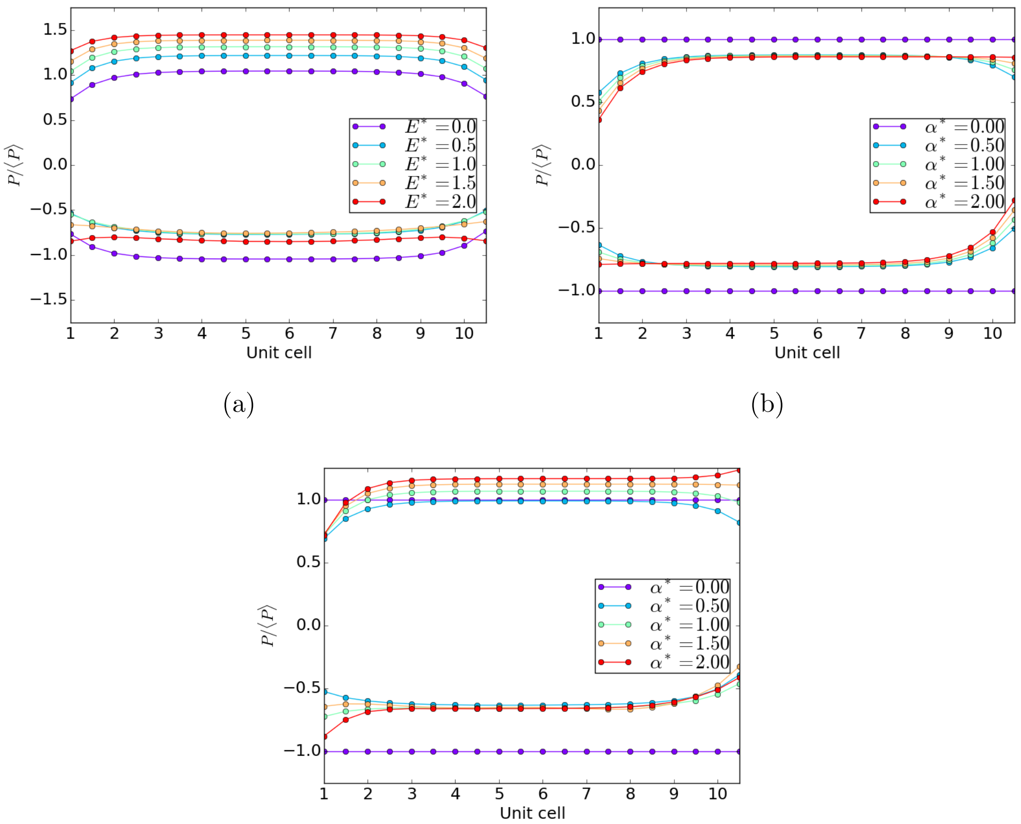

(a)

(b)

(c)

Figure 9: Polarization profiles obtained from LGDT where $\alpha_1^* = -\alpha^*$, $\alpha_2^* = \alpha^*$ and $\langle P\rangle = \langle P\rangle\Big|_{\alpha^*=0}$ with (a) $\alpha^* = 0.1$, (b) $E^* = 0.1$ and (c) $E^* = \frac{|\alpha_1^*|+|\alpha_2^*|}{2}$.

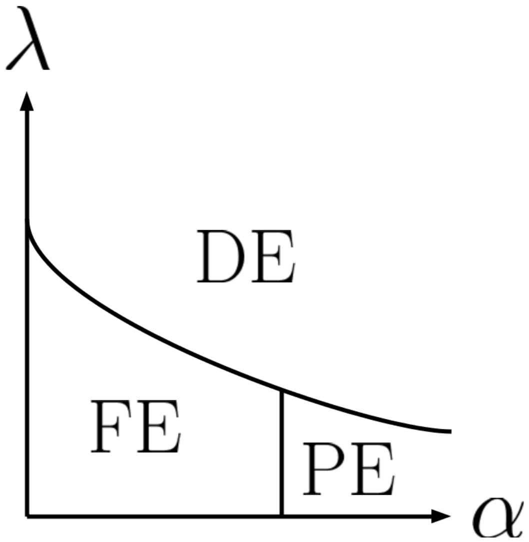

Figure 10: Schematic representation of the λ-α phase diagram of $PbTiO_3$. Here the FE, PE and DE refer to the ferroelectric, paraelectric and dielectric phase of the material, respectively.

9 $PbTiO_3$ based superlattices

9.1 Introduction

In an ideal ferroelectric the symmetries of the crystal only allow for the expansion of the free energy in even powers of the polarization, producing two degenerate ground states, one for each polarization direction, [19]. In the presence of an electric field, the degeneracy breaks due to a linear coupling between the field and polarization, favoring one state over the other depending on the sign of the field, which should produce ferroelectric polarization-field hysteresis loops with two equal but opposite coercive fields. This result would also hold for bulk-like ferroelectric layers within an inversion symmetry allowed dielectric-ferroelectric superlattice structure,[115, 116] such as $SrTiO_3/PbTiO_3$.[11].

However, electric polarization asymmetry where one polarization state is preferred over another is often seen in ferroelectric thin films and superlattices[117, 118, 119, 120, 121]. Many contributing factors have been suggested as sources of polarization asymmetry, for example polarization-strain gradient coupling[117, 122], chemical and or compositional gradient[118], domain pinning[121], asym-

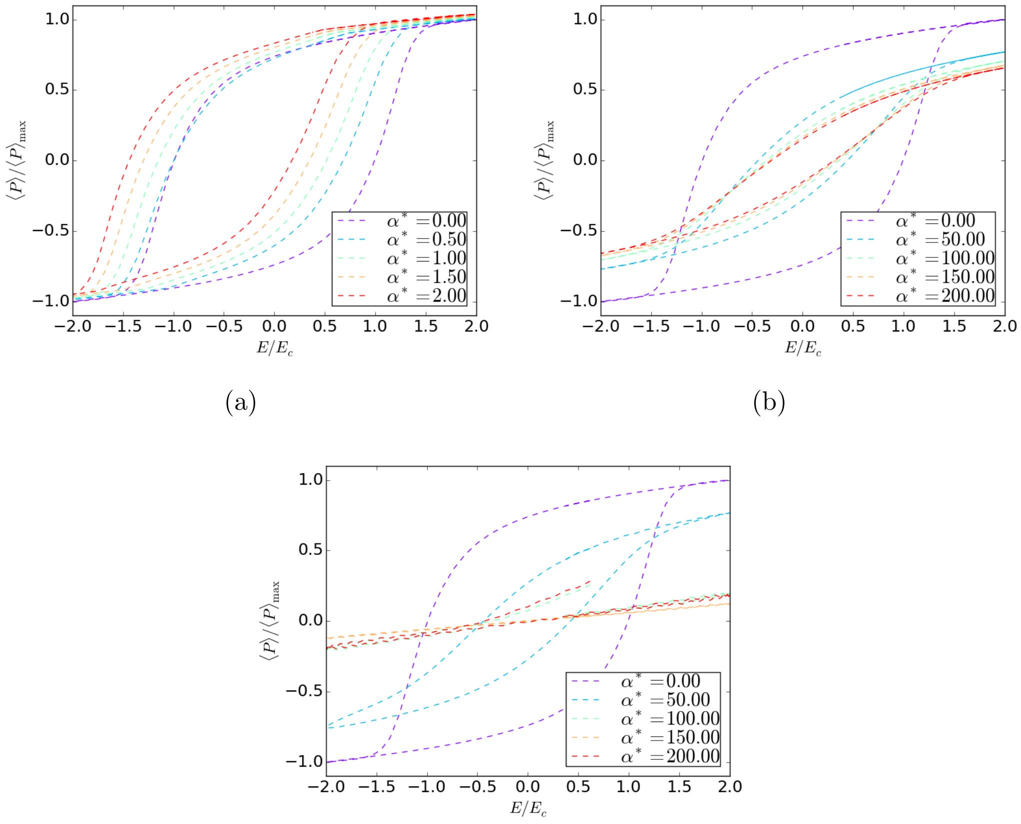

(a) (b)

(c)

Figure 11: Hysteresis curves obtained from LGDT where $\alpha_1^* = -\alpha^*$, $\alpha_2^* = \alpha^*$, (a) $E_{DD}^* = \frac{|\alpha_1^*|+|\alpha_2^*|}{2}$, (b) $E_{DD}^* = 0$ and (c) $E_{DD}^* = 0$ with $\lambda = 0.07$. Here $E_c = \arg\min\left\{\langle P\rangle\Big|_{\alpha^*=0}\right\}$ and $\langle P\rangle_{\max} = \max\left\{\langle P\rangle\Big|_{\alpha^*=0}\right\}$.

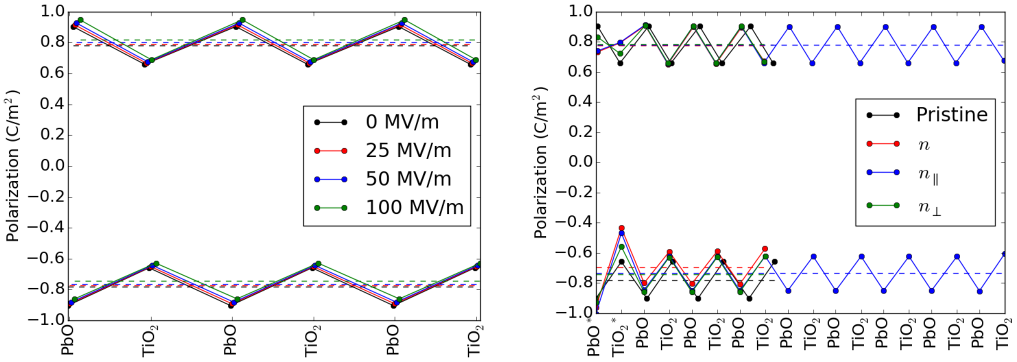

(a) (b)

Figure 12: Out-of-plane polarization profiles obtained from DFT for PTO (a) with an applied electric field and (b) with dipolar defect, where the asterisk signifies a plane with a vacancy. The dashed line represents the average polarization.

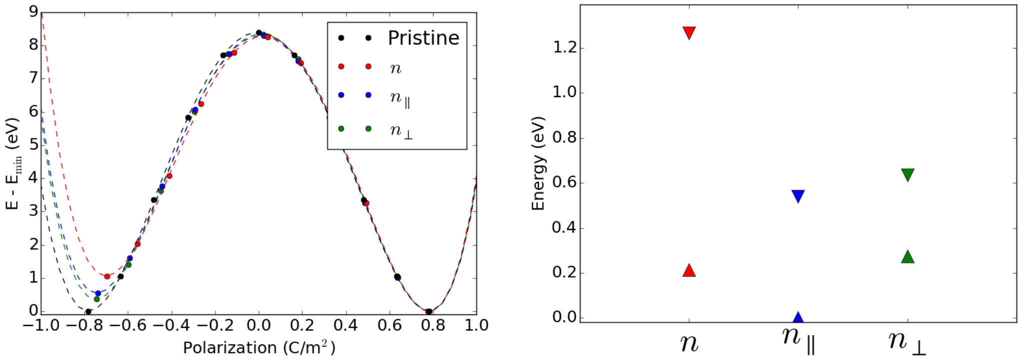

(a) (b)

Figure 13: DFT calculations of the (a) double well potentials, where each curve is relative to the ground state of the system, and (b) total energies, where up (down) triangles represent positive (negative) polarization. In the figures, the energies of n are scaled to match the energy at the potential well maximum ($P = 0$) of $n_\perp$ and $n_\parallel$.

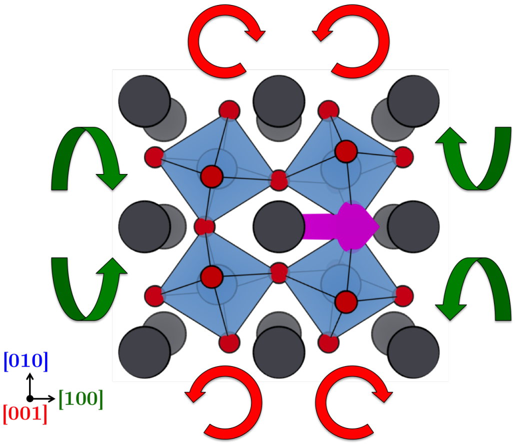

Figure 14: Representation of the local oxygen octahedra rotations near the V_{Pb}-V_O vacancy pair. The purple vector, along the [101] axis, represents the vacancy pair dipole moment. Red and green arrows represent rotations around the [100] and [001] axis, respectively. Black, blue and red spheres represent Pb, Ti, and O atoms, respectively.

metric interface[13], and other local inhomogeneities such as defects[123]. Due to all the intrinsic and extrinsic factors, it is difficult to decisively identify the source of polarization asymmetry in any given material system, and concrete solutions to control and tune this built-in bias are lacking. In artificially layered superlattices variables such as numbers of interface, asymmetry at the interface, and the composition of the superlattice can be precisely controlled, providing an excellent opportunity to systematically study the built-in bias. The goal of this study is to understand which symmetry breaking defects are the cause of the large implicit bias behavior observed in two-component superlattices, specifically $SrTiO_3/PbTiO_3$ (STO/PTO) and $SrRuO_3/PbTiO_3$ (SRO/PTO).

9.2 Methods

9.2.1 Density functional theory

Our calculations involve density functional theory (DFT) within the local density approximation (LDA) using numerical atomic orbitals implemented in SIESTA[42] and augmented plane-waves implemented in LAUTREC, an

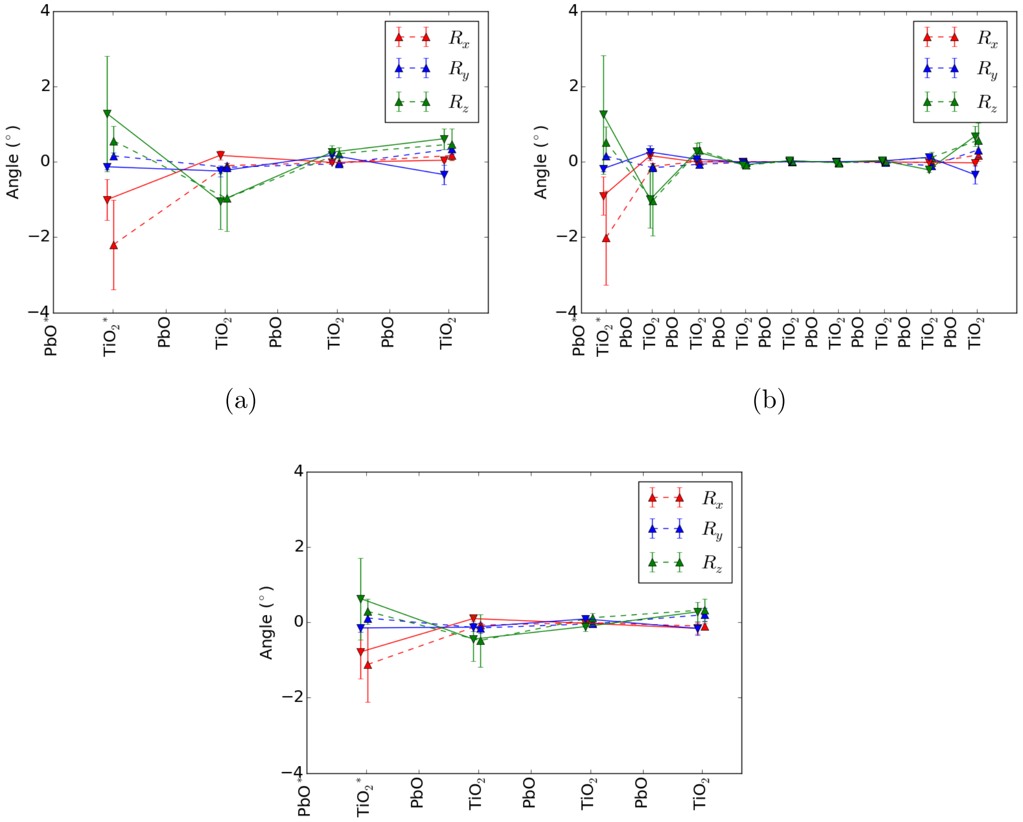

(a)

(b)

(c)

Figure 15: Rotations around the crystallographic axes for (a) n, (b) $n_\|$ and (c) $n_\perp$, where z corresponds to the direction of spontaneous polarization and the asterisk signifies a plane with a vacancy. Here x, y and z correspond to the [001], [010], and [100] axis, respectively.

in-house code.

For SIESTA, we used norm-conserving psuedopotentials generated using the Trouiller-Martins[43] scheme. The exchange-correlation functional used was PZ[124] The electrons treated explicitly with a single-ζ were $5d^{10}$ (Pb), $4s^2 4p^6$ (Sr, Ru) and $3s^2 3p^6$ (Ti). The electrons treated with a double-ζ were $6p^2$ (Pb), $5s^2$ (Sr), $4s^2 3d^2$ (Ti), $5s^1 4d^7$ (Ru) and $2s^2 2p^4$ (O). The Brillouin zone was sampled using a $6 \times 6 \times 1$ Monkhorst-Pack[50] mesh with a plane wave equivalent cutoff energy of 400 Ry. When possible the force and pressure tolerances were 0.04 eV/Å and 0.0006 eV/Å^3, respectively.

For LAUTREC, we used the projector augmented wave (PAW) scheme.[48] The exchange-correlation functional used was PW92[111] which is equivalent to PZ because they are fit to the same Ceperely-Alder data. The valence electrons explicitly treated for Pb, Sr, Ti, Ru and O were $6s^2 5d^{10} 6p^2$, $4s^2 4p^6 5s^2$, $3s^2 3p^6 4s^2 3d^2$, $4s^2 4p^6 5s^1 4d^7$ and $2s^2 2p^4$, respectively. The Brillouin zone was sampled using a $2 \times 2 \times 1$ Monkhorst-Pack mesh with a plane wave cutoff energy of 160 Ry. When possible the force tolerance was 0.08 eV/Å.

9.2.2 Polarization calculation

We calculate the polarization of our system along the growth direction (x-direction) using the modern theory of polarization. In the 1-D Wannier representation,[30] this can be written as

$$\begin{aligned} P = \frac{1}{\Omega}\sum_{l} \bar{p}_l =& \frac{1}{V}\sum_{l}\frac{1}{N_k}\sum_{\mathbf{k}}\Big[\sum_{\alpha\in l} Q_\alpha (X_\alpha - \bar{X}_l) \\ & - 2e\sum_{i\in l} f_{i\mathbf{k}}(x_{i\mathbf{k}} - \bar{X}_l) - 2e\sum_{i\in l} x_i^{EV} + Q_{l\mathbf{k}}\bar{X}_l\Big] \end{aligned} \tag{9.2.1}$$

and

$$Q_{l\mathbf{k}} = \sum_{\alpha\in l} Q_\alpha - 2e\sum_{i\in l} f_{i\mathbf{k}} \tag{9.2.2}$$

$$\bar{X}_l = \frac{1}{N_l}\sum_{\alpha\in l} X_\alpha \tag{9.2.3}$$

where Ω is the volume of the supercell, indexes α, i, k, l run over atoms, Wannier orbitals, k-points and layers respectively. $\bar{p}_l$ is the k-space averaged polarization of the l layer, Q_α and X_α are the ion core charges and the x position of the α atom, N_l is the number of atoms in the l layer, $x_{i\mathbf{k}}$ is the x position of the Wannier center of the i, k Wannier orbital, N_k is the number of k-points and $f_{i\mathbf{k}}$ is the fractional occupation of the i, k Wannier orbital. The third term on the RHS of Eq. 9.2.1 is the contribution to the polarization due to the use of PAWs.[114] We emphasize that the average over k-space should be done before doing the summation over the planes to calculate polarization, as the total charge of the system $\sum_l Q_{l\mathbf{k}}$ at each k-point is not zero, and therefore the polarization would be ill-defined otherwise. We note that the use of the fractional occupation allows us to calculate the polarization of metallic systems, which is not possible using the standard Berry phase approach.[25]

Polarization calculations as defined above are computed using the LAUTREC code on relaxed structures obtained with SIESTA. For SRO/PTO, the LAUTREC code is also used to improve on the geometry optimization of the structures, given that it implements an optimized relaxation scheme for metallic systems, allowing for quicker convergence.[125]

9.3 Results

9.3.1 Pb and O vacancies

In bulk PTO the most stable point defects are charged O vacancies.[126] However, such charged defects would lead to tail-to-tail domains[89] and not create a built-in bias. The next likely candidate, charged Pb vacancies, would similarly lead to head-to-head domains. We therefore consider Pb and O complexes, which are either nearest or next-nearest neighbor. The complexes are charge neutral because a charged Pb vacancy donates two electrons, while a charged O vacancy accepts two electrons. The divacancies can be exothermic depending on the position Fermi level in the band gap.[127] It is known that dipolar defects strongly prefer one polarization state over another which would lead to a built-in bias.[96, 94] We consider nearest neighbor Pb-O divacancies since these are found to be lower in energy than next-nearest neighbor divacancies.[110]

9.3.2 Pb-O divacancies in $SrTiO_3/PbTiO_3$

We investigated the potential energy surface of a $(STO)_2/(PTO)_5$ superlattice, with supercell area $2\sqrt{2} \times 2\sqrt{2}$, which was chosen on the criteria of having a large enough supercell to be able to simulate a moderate defect

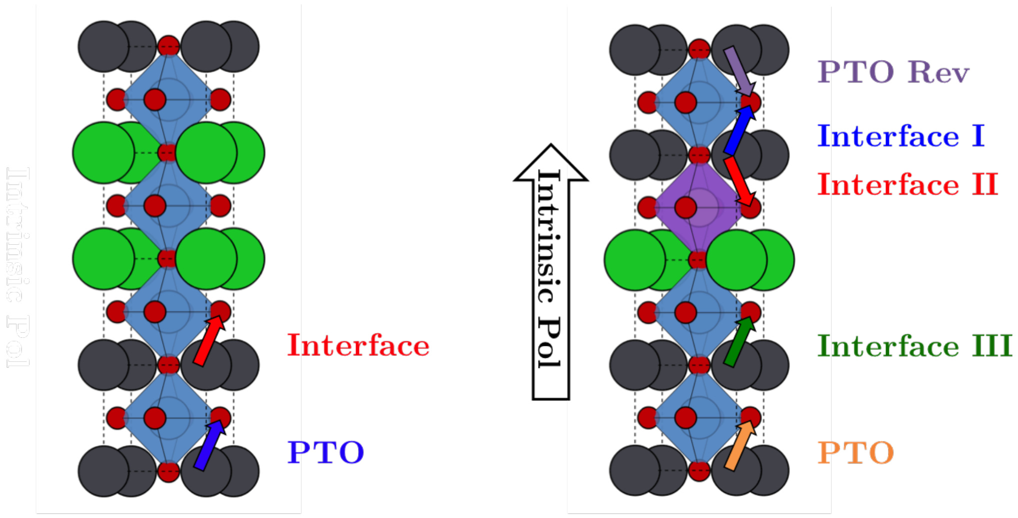

(a) (b)

Figure 16: Location of unique Pb-O divacancies dipole moments near the interface in the (a) STO/PTO and (b) SRO/PTO superlattice. For STO/PTO superlattices there is no intrinsic polarization due to the reflection symmetry at the interface. Note that the actual position of the divacancy in the PTO is much farther away from the interface than shown in the schematic.

concentration, while not being so large that at computational cost became impractical. To simulate growth on a STO substrate, the in-plane lattice constant was constrained to the STO equilibrium lattice constant, determined from first principles, to be 3.87 Å. The DVs are formed by removing a Pb atom in a PbO plane and the O atom in the adjacent TiO_2 plane which minimizes the in-plane component of the DV dipole moment. Given that STO/PTO superlattices have inversion symmetry, we only need to consider one DV dipole moment orientation (this will not be the case for SRO/PTO superlattices), shown in Fig. 16a.

We initialize our superlattice in the $P4mm$ space group, which naturally gives rise to polar distortions along the [001] direction. This is achieved through distorting the TiO_2 planes by displacing Ti atom above (below) and the O atoms below (above) the planar center, which corresponds to the system being polarized up (down). Relaxation of the system, in general, leads to two stable polarization states of opposite sign.

Our results, plotted as double well potentials in Fig. 17a show that the most stable polarization state is such that it always aligns with the DV dipole moment. The largest difference in total energy between the two polarization states, is observed when the divacancy is in the central PTO unit cell rather than at the interface. Performing simulations of model potentials by solving Fokker-Planck equations, detailed in Appendix D, we can relate the energy difference between the two polarization states to a measurable bias in the hysteresis. Fig. 17b shows that the preferred location of the DV is in the interface between the PTO and STO. We note that when the DV is in the interface the double well potential is shifted horizontally and the positive and negative polarization states are quite different in magnitude. In the experimental measurement of hysteresis we are not sensitive to this polarization shift (see Appendix D) because only the difference between the two polarization states is measured through the integrated current as the material is switched from one direction to the other.

A priori, it might be considered that DVs are equally likely to form in either direction and would have no net effect on the bias. However, as a superlattice is a grown structure there is an asymmetry introduced by the growth process. While it is not possible to directly capture this growth induced assymetry using first principle calculations, we postulate that it is this that allows the DVs to be a significant source of the bias in our samples. Consider that bulk PTO has a larger lattice constant than bulk STO due to having a larger A cation and that the superlattice as a whole is grown

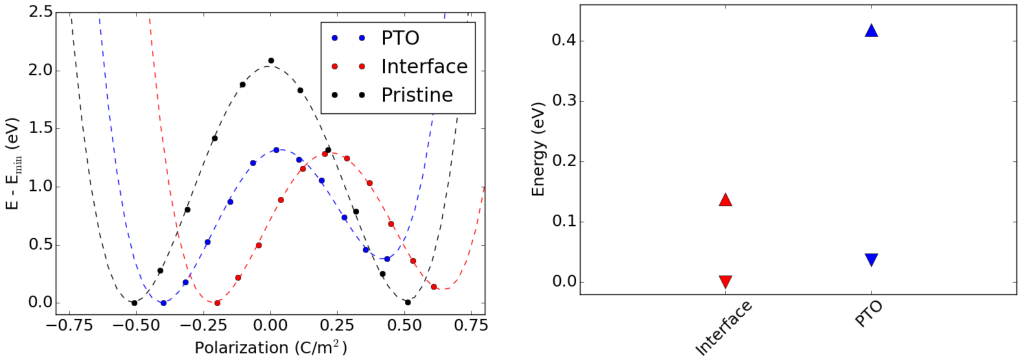

(a)

(b)

Figure 17: 2/5 STO/PTO superlattice: (a) Double well potential, where the intermediate points between the two local minima are calculated by interpolating the atomic positions. The dashed lines are best fits to a sixth order polynomial and each curve is plotted relative to its most stable state. (b) Total energy, where the up and down triangles represent positive and negative polarization of the local minima, respectively.

on an STO substrate. Therefore, when the PTO is grown on top of the STO, there is an additional drive towards vacancy formation to enable the PTO to conform to lattice constant to the substrate which is not present at the interface where STO is grown on top of PTO. There is thus a preferred interface where the DVs form with a fixed direction of the dipole moment. As DVs continue to form within the bulk of growing PTO layers they will tend to align themselves with the existing DVs that formed at the interface layer and the collective alignment of the DV dipole moments would lead to the experimentally observed bias. The observation that the built-in bias increases with increasing PTO volume fraction can be explained through a mechanism in which as thicker PTO layers are grown, more DVs are being continuously formed and they collectively align and enlarge the bias. Using the energetics of the superlattice with DVs we are able to construct a phenomenological model that can accurately map the potential energy surface.

9.3.3 Pb-O divacancies in $SrRuO_3/PbTiO_3$

Previous work[13] has shown that for SRO/PTO superlattices, with an integer number of unit cells, the interface between the SRO and PTO breaks inversion symmetry. The broken inversion symmetry adds stability to one of the polarization directions along [001], dependent on the relative ordering of the SrO and RuO_2 planes at the interface, which leads to an intrinsic polarization. This intrinsic polarization is observed in the free energy surface as an asymmetric double well potential. This asymmetric double well potential is connected to an built-in bias that would occur even in a ideal superlattice that lacked any defects. It turns out that the difference in energy between the two polarization states decreases with increasing PTO volume fraction, while for very low PTO volume fractions only one of the two states survives and the potential energy surface can be approximated as a single well potential.[13] However, just the presence of the broken inversion symmetry cannot explain the experimentally observed trend of the built-in bias with PTO volume fraction. The observed trend seen in SRO/PTO is also qualitatively different than in STO/PTO. Unlike the positive and monotonically increasing bias in STO/PTO, the bias, in SRO/PTO, is first positive and monotonically increasing, then at some critical PTO volume fraction, the bias becomes negative and monotonically decreasing.

During and after the growth of the superlattice it is not possible to experimentally determine the type of metal-ferroelectric interfaces present and therefore the direction of the intrinsic polarization. However, since the sign of the built-in bias holds for a multitude of synthesized samples, for the same PTO and SRO volume fractions, we are confident that the interfaces throughout the samples are of the same kind. Therefore, our goal is to shed light on the mechanisms behind the change in the sign of the built-in bias given a specific interface, rather than explain how and why a given interface is formed, which is outside the scope of first principles.

Ideally, to consider the role of divacancies, we would want to consider a superlattice with a very large PTO volume fraction, where the broken inversion symmetry contribution is on the order of the numerical accuracy, so that we do not confound different effects, however the convergence of such a system, with divacancies, would be impractical. Instead we studied divacancies in $(SRO)_1/(PTO)_7$ and $(SRO)_1/(PTO)_{10}$ superlattices, where contributions from the asymmetry was significant, but the two data sets, with respect to PTO volume fraction, allowed us to make confident extrapolations

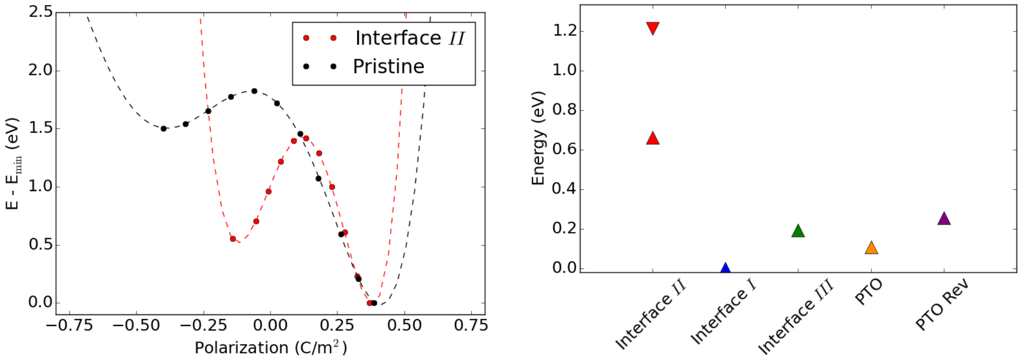

(a) (b)

Figure 18: (a) Double well potential, where the intermediate points between the two local minima are calculated by interpolating the atomic positions. The dashed lines are best fits to a sixth order polynomial and each curve is plotted relative to its most stable state. (b) Total energy, where the up and down triangles represent positive and negative polarization of the local minima, respectively.

for larger PTO volume fractions that are outside the reach of first principles calculations.

9.3.3.1 $\mathbf{SrRuO_3/PbTiO_3}$ 1/7 superlattice We begin by considering the $(\mathrm{SRO})_1/(\mathrm{PTO})_7$ superlattice, with supercell area $2\sqrt{2} \times 2\sqrt{2}$, which has a relatively high PTO volume fraction and is still computationally feasible after the introduction of DVs. Again the in-plane lattice constant was constrained to the STO equilibrium lattice constant of 3.87 Å. We initialize our PTO unit cells in the $P4mm$ space group by distorting the $\mathrm{TiO_2}$, as in the STO/PTO superlattice, giving two possible polarizations along [001]. The DVs are formed by removing a Pb atom in the PbO plane and the O atom in the adjacent $\mathrm{TiO_2}$ or $\mathrm{RuO_2}$ plane which minimizes the in-plane component of the DV dipole moment, such that the main component is along the [001] direction. For DVs formed at the interface, there are three unique locations, where the location fixes the direction of the DV dipole moment and unlike the interfacial DVs in the STO/PTO superlattice, these DVs cannot be related through a π rotation.

The three interfacial DVs, shown in Fig. 16b, are in the PTO unit cell near to the RuO_2 layer (Interface I), in the PTO unit cell near the SrO layer (Interface III) and in the PbO-RuO_2 layers, which we refer to as the $PbRuO_3$ (PRO) unit cell (Interface II). We note that Interface I and Interface III dipole moments are parallel with the direction of the asymmetry in the superlattice, while for Interface II the dipole moment is antiparallel. For DVs formed in the center of the PTO, we must consider both orientations, because, in contrast to DVs in PTO/STO, they would not lead to the same energetics due to the presence of the asymmetry. To summarize, in total, we separately consider 5 DVs, for both of the initial polarizations, three in the interface, at different locations with varying orientations, and two in the same central PTO unit cell, but with different orientations.

The intrinsic polarization direction, shown by the asymmetric double well in Fig. 18a, is determined by the order of the SrO and RuO_2 planes, which we keep constant throughout all our other calculations. We found that for all DVs, except the one formed in Interface II, we were only able to stabilize the intrinsic polarization state. Among the interfacial DVs, the most stable location is Interface I followed by Interface III, with the least stable being Interface II, as shown in Fig. 18b. We speculate that the reason Interface II has two stable polarization states is because of the metallic RuO_2 layer screening the DV, which reduced the coupling of the DV with the asymmetry. Likewise, Interface I is the most stable configuration due to favorable coupling with the asymmetry as well as being closer to the RuO_2 layer to better screen the polarization charges. In addition, the computational constraints on the calculations cause the defect concentration, calculated in Appendix E, to be significantly higher than experiments. The result that the majority of the calculations lead to a single polarization state give evidence that even for a superlattice, with a relatively high PTO volume fraction, the broken inversion symmetry plays a very dominant role. However, we do note that the difference in energy between the two polarization states is decreased, relative to the pristine case, when the DV exists in the interface. We emphasize that in experiments, the PTO volume fraction in SRO/PTO superlattices needed to achieve the same asymmetry seen in first principle calculations would be significantly lower and therefore we should not interpret our results as probing the true high PTO volume fraction superlattices.

In the absence of the asymmetry, the stability of the interfacial DVs would involve an interplay between epitaxial strain, screening and electrostatic coupling, whose sources are the STO substrate, Ru atoms and the PTO

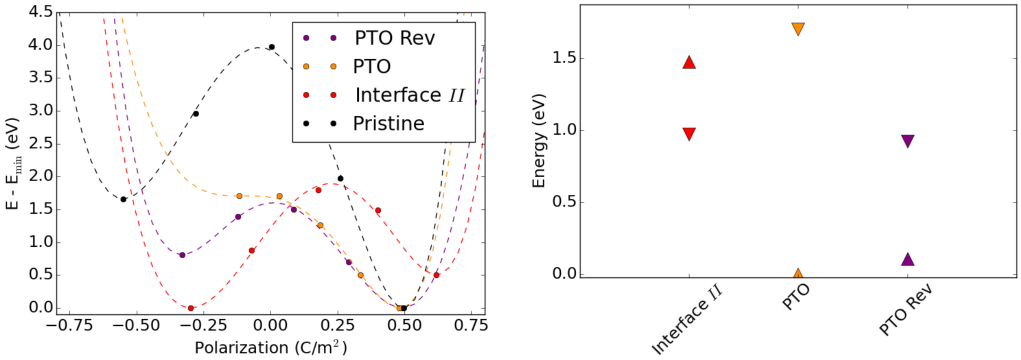

(a) (b)

Figure 19: 1/10 SRO/PTO superlattice: (a) Double well potential, where the intermediate points between the two local minima are calculated by interpolating the atomic positions. The dashed lines are best fits to a sixth order polynomial and each curve is plotted relative to its most stable state. (b) Total energy, where the up and down triangles represent positive and negative polarization of the local minima, respectively.

unit cells, respectively. We can get an insight into how the these effects contribute to the ground state energy by analyzing the formation energy of the Pb-O DV in bulk PRO and PTO constrained to the STO lattice constant, which corresponds to competition of the epitaxial strain with the screening and electrostatic coupling effects, respectively. The results, detailed in Appendix F, suggest that, in the absence of the asymmetry, the most energetically favorable location for the DV to form is in the PRO unit cell, previously labeled as Interface II. Coupling these results with the increase in the stability of the polarization opposite to the intrinsic direction when the DV is present in Interface II, we further probe the SRO/PTO superlattice with even higher PTO volume fraction to observe a new intrinsic polarization direction.

9.3.3.2 SrRuO$_3$/PbTiO$_3$ 1/10 superlattice We followed the same methodology as for the 1/7 superlattice, except, due to computational constraints, only studied the DVs located in the central layer of the PTO and PRO layer of the interface. Our results, summarized in Fig. 19a, confirm a new intrinsic polarization direction, relative to the pristine superlattice, when the DV is present in the interface. While we do not observe such a reversal when the DVs are in the PTO, we emphasize that we are now able to stabilize two polarization states, strongly implying that a reversal would occur at higher PTO volume fractions. The most stable location for DV formation, shown in Fig. 19b, is in the PTO when the orientation of the DV dipole moment is parallel to the intrinsic polarization. We strongly suspect from the trend in the data that going to higher PTO concentrations would yield even more favorable results for DVs to form in Interface *II*. While the total energy is higher for the DV to form in the interface than the PTO, we emphasize that growth conditions need to be taken into account, which favor the DVs to initially form in the interface as the superlattice is being grown. Therefore, during growth, the initial formation of DVs at Interface *II* cause additional DVs that form in the PTO to align with their orientation. The collective coupling of the DVs leads to the stability of the polarization state that is opposite to the intrinsic polarization induced from the broken inversion symmetry at the interface.

The experimentally seen built-in bias can thus be divided into two regimes, the low PTO volume fraction and the high PTO volume fraction regime, where the bias is positive and negative, respectively. In the low PTO regime the superlattice asymmetries are dominated by the inversion symmetry breaking at the interface, which as the previous authors[13] has shown, can be effectively described as a single well potential. The negative sign of the bias is determined by the direction of the asymmetry, fixed by the ordering of the interface during growth. It is likely that DVs are also are formed in this regime, however their effects are washed out due to the strength of the asymmetry. As the superlattice is grown with higher PTO volume fractions the effects from the inversion symmetry breaking, while present, become much weaker and the effects of the DVs start to dominate. The most energetically favorable interfacial DV to form is within the PRO unit cell (Interface *II*) and its dipole moment direction is opposite to that of the intrinsic polarization direction coming from the broken inversion symmetry. This implies that there should be a reversal in the sign of the bias when the inversion symmetry breaking effects are sufficiently weak and the bias now being determined by the collective alignment of dipole moments, to minimize the total energy, whose orientations are fixed by the DVs formed in the PRO. We can summarize the behaviors of the two regimes by stating that the low PTO regime is dominated by inversion symmetry breaking that favors a particular polarization direction, while the high PTO regime is dominated by DVs, whose dipole moment orientations are precisely opposite to that of the intrinsic polarization direction.

9.4 Conclusion

Our results attribute the built-in bias, seen in experiments, to Pb-O divacancy formation, whose orientation determines the sign of the bias. In STO/PTO superlattices, growth conditions determine the dipole moment orientation of the divacancies nucleating at the interface, with additional divacancies forming parallel in the PTO, as the superlattice is being grown, leading to a larger bias with increasing PTO thickness. Meanwhile, in SRO/PTO superlattices the location and orientation of the divacancy dipole moment is determined by the interplay between the strength of the inversion breaking asymmetry, regulated by the PTO thickness, screening, and the epitaxial strain, which leads to the formation of two regimes, with opposite bias. By identifying the mechanisms behind the presence of the asymmetries we will able to engineer robust superlattices by combining the phenomena that cause biases, with opposite signs, creating an built-in bias-free superlattice.

10 $PbTiO_3$ based capacitors

10.1 Introduction

Thin film capacitors have an encouraging outlook on being used as memory storage devices over flash memory, primarily due to their low energy consumption and write speed. Lead titanate is a suitable candidate for such devices primarily due to its large switching charge and low process temperature,[128] however, in trying to push the boundaries of information storage density, scalability issues arise. There has been experimental evidence[129, 130] showing that the ferroelectric phase of lead titanate is limited by the layer thickness, where the suppression of the ferroelectricity is due to the reconstruction of atoms. In addition, the decrease of the lead titanate phase would add importance to any effects coming from the ferroelectric/metal interface. Therefore, understanding the interfacial effects would aid in tailoring the design of nanocapacitors with favorable properties.

While previous studies on $PbTiO_3$ (PTO) with $SrRuO_3$ (SRO) electrodes have been studied for both capacitors[131] and superlattices,[13] to our knowledge, there lacked a systematic study of the interfacial effects to determine the underlying mechanics in the enhancement or suppression of the polar order in these materials. In this first principles study, we focus on symmetrical SRO/PTO capacitors and superlattices, under epitaxial strain, allowing us to analyze interfacial effects for both paraelectric and ferroelectric phases. We relate our results to the conclusions drawn by previous work done on these systems and suggest other systems where our results can be applied to.

10.2 Methods

Our calculations involve density functional theory (DFT) within the local density approximation (LDA) using numerical atomic orbitals implemented in the SIESTA[42] code. We used norm-conserving psuedopotentials generated using the Trouiller-Martins[43] scheme. The electrons treated explicitly with a single-ζ were $5d^{10}$ (Pb), $4s^2 4p^6$ (Sr, Ru) and $3s^2 3p^6$ (Ti). The electrons treated with a double-ζ were $6p^2$ (Pb), $5s^2$ (Sr), $4s^2 3d^2$ (Ti), $5s^1 4d^7$ (Ru) and $2s^2 2p^4$ (O). The Brillouin zone was sampled using a $6 \times 6 \times 1$ Monkhorst-Pack[50] mesh. We converged our electronic density with a tolerance of 10^{-4} eV on a uniform real space grid with a plane wave equivalent cutoff energy of 400 Ry and a Fermi smearing temperature of 0.009 eV (100 K) for quicker convergence. The force and pressure tolerances were 0.01 eV/Å and 0.0006 eV/Å^3, respectively.

The systems under consideration are symmetrically terminated SRO/(PTO)$_m$ superlattice and SRO/(PTO)$_m$/SRO capacitors, where m is an integer. There are two possible cases, either we have RuO$_2$-SrO-RuO$_2$/(PbO-TiO$_2$)$_m$-PbO/[RuO$_2$-SrO-RuO$_2$] or SrO-RuO$_2$-SrO/TiO$_2$-(PbO-TiO$_2$)$_m$/[SrO-RuO$_2$-SrO] layers, as illustrated in Fig. 20a and 20b, where the term in the square brackets is absent if our system is a superlattice. We refer to these two cases, both for superlattice and capacitor, as Sr and Ru excess, respectively. To probe the rich parameter space available, we varied the amount of PTO layers from 2 and 4, the supercell area from 1×1 to $\sqrt{2} \times \sqrt{2}$ and the in-plane lattice constant ($a = b$) from 3.87 Å, which is the superlattice SrTiO$_3$ (STO) equilibrium lattice constant, a_0, determined from first principles, to 3.67 Å. Varying the lattice constant is equivalent to inducing an epitaxial strain $e = \frac{a-a_0}{a}$ on the crystal from 0% to -5.16%. To determine the lowest energy ground state we avoid initializing our system in highly symmetric space groups such as $P4/mmm$ and $Pm\bar{3}m$ because it allows our system to be trapped in a saddle point. Instead, we initialized our system in either the $P4mm$ or $P4bm$ space group when the supercell area was either 1×1 or $\sqrt{2} \times \sqrt{2}$, respectively. The $P4mm$ and $P4bm$ space groups naturally give rise to polar distortions along the c-axis and additionally oxygen octahedra rotations around the c-axis, respectively. It is important to note that we did not enforce any symmetry group constraints during the course of the relaxation.

10.3 Results

The main challenge for synthesizing ferroelectric materials as the boundary condition changes from closed to open is the presence of the depolarization field.[69] The strength of the depolarization field depends on the amount of screening charge coming from the electrodes. For fixed screening length, the electrode with more metallic states should be able to better stabilize the ferroelectric state. However, this picture is not fully applicable to the systems in question, because the electrode is only a single layer thick, and thus we might expect pathological cases to develop. In addition, the electrode is subject to the same strain conditions as the ferroelectric, potentially modifying its screening properties.

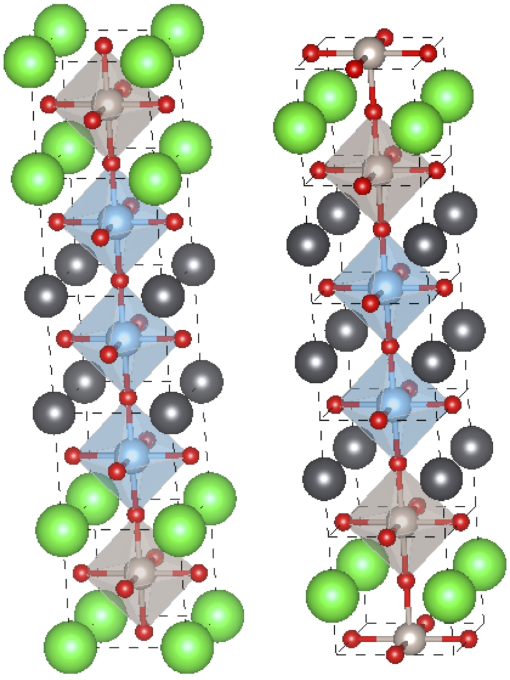

(a) (b)

Figure 20: Supercell of the capacitor for SRO/$(PTO)_2$/SRO where the interface has an excess of either (a) Sr or (b) Ru. Green, grey, brown, blue and red correspond to Sr, Pb, Ru, Ti and O, respectively.

10.3.1 Superlattices

Although the superlattices are not subject to surface effects, each metal/ferroelectric/metal layer in the superlattice needs to be able to screen the bound charges to develop a polarization within the ferroelectric. Therefore, the more metal present at the interface the better the charge screening. The nature of ferroelectricity in PTO originates from the hybridization of the Ti $3d$ and O $2p$ orbitals.[8] This implies that the sensitivity of the hybridization, and thus the polar order, will be dependent on the distance between the Ti and O atom lying along the direction of polarization. We thus define the average distance along the z axis (the axis of polarization), between Ti and O atoms, normalized to superlattice PTO (cf. Ref. [132]) as the parameter of interest, given in Eq. 10.3.1.

$$\Delta_{norm} = \frac{\bar{d}^p - \bar{d}^f}{d^p_{PTO} - d^f_{PTO}} \tag{10.3.1}$$

Here $\bar{d}^p$ and $\bar{d}^f$ is the average distance between the Ti and the apical O atoms for the paraelectric and the ferroelectric phase of the PTO/SRO superlattice, respectively. Δ_{norm} is zero when the ground state of the superlattice is paraelectric and can go above 1 if the polar order is greater than bulk PTO. We access the paraelectric phase of the superlattice by initializing the PTO layers in the $P4/mmm$ space group and constraining the PTO layers to be centrosymmetric.

In Fig. 22a, Δ_{norm}, for either amount of PTO layers, is larger when there is an excess of Ru than Sr at the interface. In addition, for $m = 2$, superlattices with Ru excess interfaces are able to undergo a ferroelectric transition at a smaller strain (larger lattice constant) than an interface with Sr excess, irrespective of the supercell area. The general trend is an enhancement of Δ_{norm} for Ru excess interfaces regardless of lattice strain or PTO composition, which thus far can be attributed to double the amount of free charge in Ru excess interface relative to the Sr excess interface.

To analyze the effects on Δ_{norm} coming from the SRO, shown in Fig. 21, we fixed our parameters to be $m = 2$, $A = 1 \times 1$ and the in-plane lattice constant as 3.72 Åand varied the amount of SRO layers in the superlattice from 1 to 3. In the figure, Δ_{norm} for Sr excess superlattices decreases with increasing SRO layers, due to a lack of coupling between adjacent PTO layers, while Δ_{norm} for Ru excess superlattices is able to keep its polar order constant up to two layers of SRO, after which it converges to the Sr excess value. We can conclude that interface effects are only relevant below three layers of

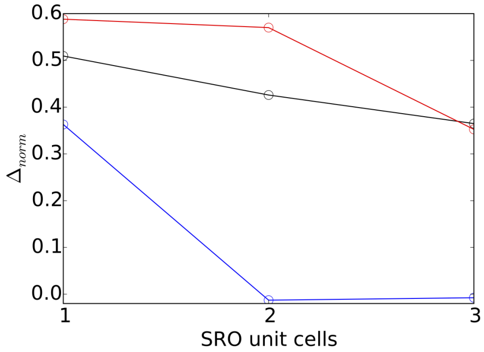

Figure 21: Δ_{norm} measure of SRO/PTO superlattices. Black, red and blue correspond to superlattices with Sr excess, Ru excess and asymmetric interfaces, respectively.

SRO.

10.3.2 Capacitors

To determine the polar order of the capacitors we calculate the macroscopic dipole moment of the supercell given in Eq. 10.3.2.

$$\mu = \int_{\Omega} z(\rho(\mathbf{r}) - \rho_{atom}(\mathbf{r}))\, d\mathbf{r} \tag{10.3.2}$$

Here Ω, ρ, and ρ_{atom} is the volume of the supercell, pseudovalence charge density and atomic (non-interacting) pseudovalence charge density, respectively. The quantity, $\rho - \rho_{atom}$, is also equivalent to the charge deformation density. The dipole moment, μ, is uniquely defined because periodic boundary conditions are broken along the z direction.

The uniformity of the polar order that was seen in the superlattices is absent when we study capacitors, suggesting that surface effects are present. In Fig. 22b, we reaffirm that for $A = 1 \times 1$, Ru excess capacitors undergo a ferroelectric transition at a smaller strain than Sr excess capacitors, but there are significant differences. (i) When the supercell area is 1×1 and at a high strain the dipole moment is larger for Sr excess than Ru excess capacitors. (ii) The polar order in Ru excess capacitors varies little with increased strain or amount of PTO layers, but varies greatly with the supercell area. (iii) When the supercell area is $\sqrt{2} \times \sqrt{2}$ both Sr and Ru excess interfaces undergo a ferroelectric transition at the same strain. These differences occur due to multiple competing mechanisms present in the capacitors, which will be analyzed separately and related to the deviation from the superlattice results.

We find that Sr excess interfaces require a larger strain to overstabilize the polar order relative to Ru excess interfaces because of a charge spillout from the electrode.[68] One of the TiO_2 planes closest to the electrode becomes metallic, as shown in Fig. 24a, which prevents that Ti from taking part in the development of polar order, however at relatively large strains where the polar order is stabilized anyway, the TiO_2 metallic layer provides additional screening and thus the capacitor is able to develop a stronger polar order. It is important to note that this effect only occurs when $A = 1 \times 1$ and thus is an artifact, as shown in Fig. 24b, attributed to the underapproximation of the conduction band minimum in the DFT calculation.

The weak dependence of the polar order on strain in Ru excess capacitors can be explained by the formation of a relatively huge surface dipole, with opposite orientation to the dipole moment of the PTO layers. Analyzing the pattern of the charge deformation density reveals that Ti ions in Sr excess capacitors, polarize in the direction of the total dipole moment as expected, shown in Fig. 26a. However, Ti ions in Ru excess capacitors are anomalously polarized in the opposite direction, shown in Fig. 26b.

To get a better understanding of how effects (i) and (ii) influence the total dipole moment of the capacitor, we define the charge neutral unit cell dipole moment, given in Eq. 10.3.3.

$$\mu_i = \int_{\Omega_i} z\tilde{\lambda}(z)dz \tag{10.3.3}$$

Here $\tilde{\lambda}$ and Ω_i is the nanosmoothed[133] linear charge deformation density and the length of the unit cell along the c-axis, subject to the constraint $\int_{\Omega_i} \tilde{\lambda}(z)dz = 0$, respectively. The charge neutral unit cells are uniquely defined, due to a lack of periodic boundary conditions, as long as Ω_i do not envelope the vacuum region. In the paraelectric phase, the μ_i have inversion symmetry, as shown in Fig. 25a. However, not only is the inversion symmetry broken during the ferroelectric phase transition, giving rise to a net dipole in the PTO, but also a large dipole is present in the outer RuO_2 layer, because of the suppressed charge deformation, shown in Fig. 25b. This surface dipole always forms on the electrode which is at the head of the dipole moment vector in the PTO, and thus the surface dipole points into the interface. It

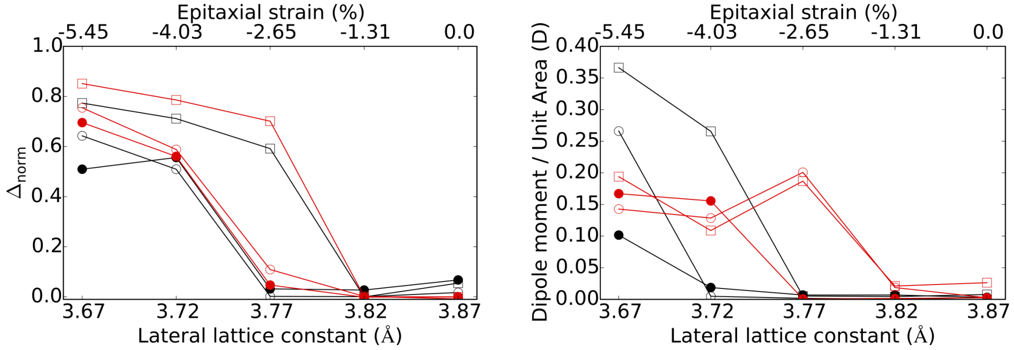

(a)

(b)

Figure 22: Ferroelectricity measures for (a) capacitor SRO/(PTO)$_m$/SRO and (b) superlattice SRO/(PTO)$_m$. Black and red correspond to capacitors (superlattices) with Sr excess and Ru excess interfaces, respectively. Open circles, closed circles and open squares correspond to (m, A) values of (2, 1×1), (2, $\sqrt{2} \times \sqrt{2}$) and (4, 1×1), respectively.

is important to note that when the simulation is repeated with more than one layer of SRO, the surface dipole disappears.

When the area of the supercell is doubled, additional structural relaxations occur in the form of oxygen octahedra rotations around the z-axis. Sr excess capacitors exhibit, in Glazer notation,[134] $a^0a^0c^+$ and $a^0a^0c^-$ tilts in the PTO, shown in Fig. 23a, while for Ru excess capacitors only $a^0a^0c^-$ tilts are present for both PTO and SRO, shown in Fig. 23b. The addition of rotations diminish the stability of the polar order, which is evident for Ru excess capacitors where the polar order is suppressed at 3.77 Å. It is also interesting to note that the surface dipole in Ru excess capacitors is enhanced from the oxygen rotations. However, for both types of capacitors, the oxygen rotations have a minimal effect on μ_i and thus are secondary corrections, relative to strain, to the ferroelectricity.

10.4 Conclusion

We have investigated the effects of interfaces on polarization in epitaxially strained SRO/PTO superlattices and capacitors by varying the supercell area and PTO volume fraction for a given strain. Our results indicate that, for

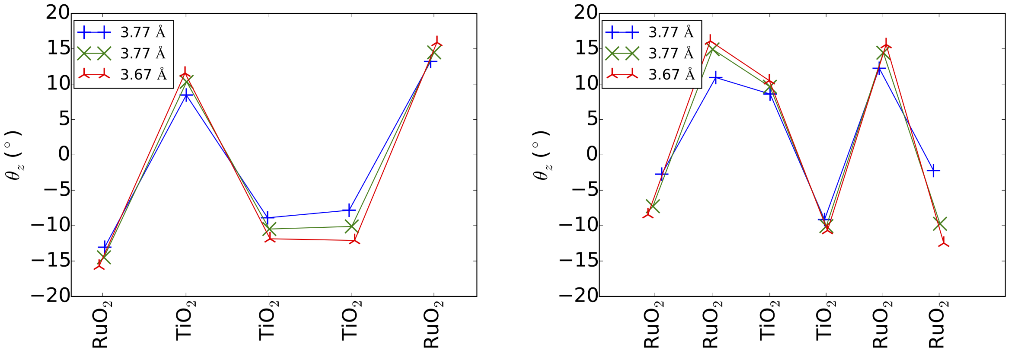

(a) (b)

Figure 23: Rotations around the c-axis for (a) Sr and (b) Ru excess interfaces, $\sqrt{2} \times \sqrt{2}$ capacitor.

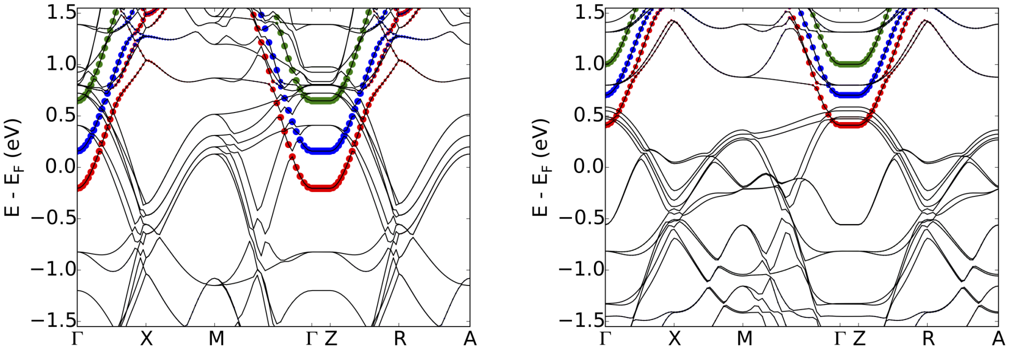

(a) (b)

Figure 24: Projected Ti $d_{x^2-y^2}$ orbitals on the electronic dispersion for Sr excess capacitor ($m = 2$; $A = \sqrt{2} \times \sqrt{2}$) with (a) frozen $A = 1 \times 1$ and (b) fully relaxed configurations. Red, blue, and green correspond to the first, second, and third TiO$_2$ layer relative to the head of the dipole moment in the capacitor, respectively.

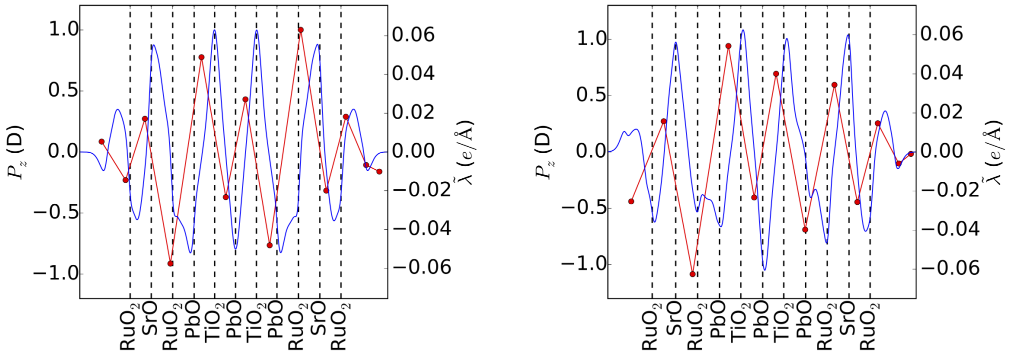

(a) (b)

Figure 25: The blue lines and red data points represent the nanosmoothed linear charge deformation density and the layer dipole moment, respectively, when the Ru excess $\sqrt{2}\times\sqrt{2}$ capacitor is (a) paraelectric and (b) ferroelectric. The black dashed lines represent the average position of the atoms in that plane.

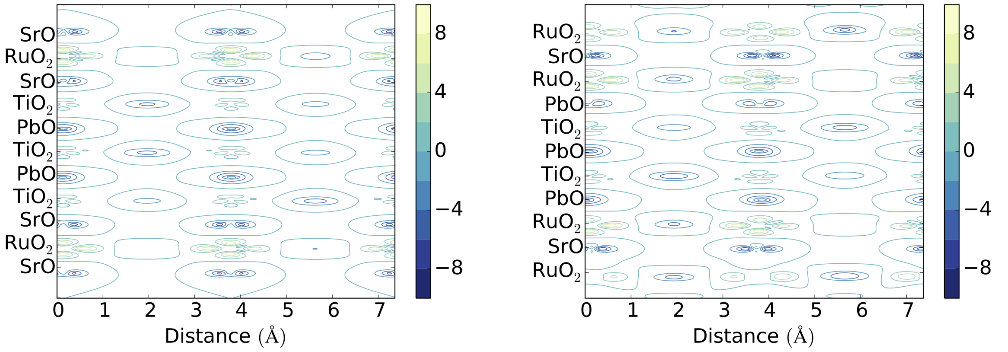

(a) (b)

Figure 26: Charge deformation density, in units of $e/\text{Å}^3$, $\rho - \rho_{atom}$ for (a) Sr and (b) Ru excess $\sqrt{2} \times \sqrt{2}$ ferroelectric capacitor. Positive (negative) charge density correspond to electron deficient (excess) regions.

superlattices, the polar order is proportional to the amount of screening charge available, coming from the Ru ions at the interface and is insensitive to the other parameters we varied. Therefore, a possible way to determine the type of interfaces in the superlattice is to keep the amount of PTO layers fixed, while varying the SRO from one to two layers. A decrease in the polar order would signify Sr excess interfaces, while a lack of change would imply Ru excess interfaces.

Capacitors under strain exhibit oxygen octahedra rotations, although their contribution to the polar order was secondary compared to the other parameters that were varied. For capacitors, with Ru excess surfaces, we observed an anomalously large surface dipole on the RuO_2 layer, coming from the epitaxial strain on the electrode. The surface dipole moment is aligned opposite to the dipole moments of the PTO layers and dominates the total dipole moment of the capacitor. While the surface dipole would either form on the top or bottom electrode depending on the polarization direction of the PTO, in practice, the bottom electrode would be attached to the substrate, which could provide additional screening to the polarization and suppress the formation of the dipole in the bottom electrode. Since a surface dipole would only form for one direction of the polarization, a measurable bias would form even when both surfaces are symmetric. If the amount of SRO layers is increased, the surface dipole disappears, suggesting that the metallic layer should be no smaller than two layers to have a functional capacitor.

A Fast evaluation of the Madelung constant

Evaluations of Madelung constants is important to perform charge corrections or any other interactions that involve central potentials. In general we want to evaluate the following quantity

$$\alpha_s(\mathbf{d}) = \sum_{\mathbf{n}=-\infty}^{\infty} \frac{q(\mathbf{n})}{|\mathbf{A}\cdot\mathbf{n}-\mathbf{d}|^s} \equiv \sum_{\mathbf{n}=-\infty}^{\infty} \frac{e^{2\pi i \mathbf{c}\cdot\mathbf{A}\cdot\mathbf{n}}}{|\mathbf{A}\cdot\mathbf{n}-\mathbf{d}|^s} \tag{A.1}$$

where $\mathbf{A}$, $\mathbf{n}$, $\mathbf{d}$, $\mathbf{c}$, s is the matrix governing the periodicity of the crystal, 3-dimensional vector of integers, vector where we evaluate the Madelung constant at, auxiliary vector that gives the charges at the lattice points and a complex number, respectively. This form of the Madelung constant is known as the generalized (Epstein) zeta function, and it is implied that the summation over vanishing denominators is ignored. Computing α_s involves using the Theta function identity[135]

$$\sum_{\mathbf{n}=-\infty}^{\infty} e^{2\pi i \mathbf{c}\cdot\mathbf{A}\cdot\mathbf{n}-\pi t|\mathbf{A}\cdot\mathbf{n}-\mathbf{d}|^2} = t^{-3/2}\frac{e^{2\pi i \mathbf{c}\cdot\mathbf{d}}}{\det\mathbf{A}} \sum_{\mathbf{k}=-\infty}^{\infty} e^{-2\pi i \mathbf{d}\cdot\mathbf{B}\cdot\mathbf{k}-\pi|\mathbf{B}\cdot\mathbf{k}-\mathbf{c}|^2/t} \tag{A.2}$$

where $\mathbf{B} = \mathbf{A}^{-T}$ and t is a real number. Now to proceed, we can recast the zeta function as a Mellin transform,[136] and we write

$$\alpha_s(\mathbf{d}) = \frac{\pi^{s/2}}{\Gamma(s/2)} \int_0^{\infty} t^{s/2-1}\Big[-\delta(\mathbf{d}) + \sum_{\mathbf{n}=-\infty}^{\infty} e^{2\pi i \mathbf{c}\cdot\mathbf{A}\cdot\mathbf{n}-\pi t|\mathbf{A}\cdot\mathbf{n}-\mathbf{d}|^2}\Big]dt. \tag{A.3}$$

Next, we split the integral into $(0,1)$ and $(1,\infty)$. Then, for the integral over $(1,\infty)$ we do a change of variables to $u = 1/t$. Finally, evaluating both integrals yields incomplete gamma functions and results in[135]

$$\begin{aligned}\alpha_s(\mathbf{d}) = \frac{\pi^{s/2}}{\Gamma(s/2)}\Bigg[&\frac{\delta(\mathbf{c})\det\mathbf{B}}{s/2-3/2} - \frac{\delta(\mathbf{d})}{s/2} + \sum_{\mathbf{n}=-\infty}^{\infty}\frac{\Gamma(s/2,\pi|\mathbf{A}\cdot\mathbf{n}-\mathbf{d}|^2)e^{2\pi i \mathbf{c}\cdot\mathbf{A}\cdot\mathbf{n}}}{(\pi|\mathbf{A}\cdot\mathbf{n}-\mathbf{d}|^2)^{s/2}} \\ &+ \frac{e^{2\pi i \mathbf{c}\cdot\mathbf{d}}}{\det\mathbf{A}}\sum_{\mathbf{k}=-\infty}^{\infty}\frac{\Gamma(\frac{3-s}{2},\pi|\mathbf{B}\cdot\mathbf{k}-\mathbf{c}|^2)e^{-2\pi i \mathbf{d}\cdot\mathbf{B}\cdot\mathbf{k}}}{(\pi|\mathbf{B}\cdot\mathbf{k}-\mathbf{c}|^2)^{\frac{3-s}{2}}}\Bigg]\end{aligned} \tag{A.4}$$

which, while nuanced, is computationally feasible due to the rapidly decaying sums of incomplete gamma functions.

B Hybrid Wannier functions

Often one is interested in the polarization of a system only along one direction. In the Wannier representation the 1D polarization would then be given by

$$P = \frac{e}{\Omega}\sum_n \langle x\rangle_n + \frac{e}{\Omega}\sum_I Z_I X_I \tag{B.1}$$

which is defined modulo eL/Ω, where L is the dimension of the primitive cell parallel to the direction of polarization. Since we are only interested in the x position of the center of mass we can potentially generate Wannier functions that are maximally localized in x, but delocalized in the other orthogonal directions. Such functions are called hybrid Wannier functions, however we do not need to explicitly calculate them and we can obtain $\langle x\rangle_n$ through other means.[137]

We begin by constructing the overlap matrix

$$M_{mn}^{(k_i)} = \langle u_{mk_i}|u_{nk_{i+1}}\rangle \tag{B.2}$$

where the increment of k is along the direction polarization. Next, we can construct M to be Hermitian from the singular value decomposition by

$$M = V\Sigma W^\dagger = (V\Sigma V^\dagger)(VW^\dagger) \tag{B.3}$$

therefore to cancel out $VW^\dagger$ we must apply a unitary transformation on M by $WV^\dagger$. The unitary transformation $WV^\dagger$ is applied at each k-point in succession to pick up a generalized Berry phase[30] defined by

$$\Lambda = \prod_{j=1}^{N} W^{(k_j)} V^{\dagger(k_j)} \tag{B.4}$$

where the product spans a closed path. Finally the positions are obtained from

$$\langle x\rangle_n = -\frac{L}{2\pi}\Im\log(\lambda_n) \tag{B.5}$$

where λ_n are the eigenvalues of Λ.

C Dipole lattices

The dipolar defects (DDs) in a ferroelectric can be considered to exist on a lattice and assuming the defect density is dilute, their interactions can be described using a dipole approximation. Such a derivation of the electric field is preferred over the use of spherical inclusions[96, 138] because the calculation becomes cumbersome when DD electric field $\mathbf{E}_{DD}$ is not oriented with the spontaneous polarization $\mathbf{P}_s$ and the crystal symmetry needs to be accounted for.[139] We calculate the electric field arising from these dipole interactions and the energy of the DD lattice to determine which defect formations are the most stable.

C.1 Electric field of the dipole lattice

We begin by considering a dielectric with negligible polarization, such as a ferroelectric shortly after growth, with point DDs ordered in orthorhombic lattices. The structure of dipoles lead to a macroscopically observable $\mathbf{E}_{DD}$ which is the contribution of the dipole electric field at one dipole caused by all the other dipoles.[140] The total field can be written as

$$\mathbf{E}_{DD}^{(\nu_0)} = \sum_{\nu}\sum_{i} \frac{3(\mathbf{p}_{i\nu} \cdot \mathbf{r}_{i\nu})\mathbf{r}_{i\nu} - r_{i\nu}^2 \mathbf{p}_{i\nu}}{r_{i\nu}^5} \tag{C.1}$$

where $\mathbf{p}_{i\nu}$ and $\mathbf{r}_{i\nu}$ is the i^{th} dipole of the ν^{th} sublattice and i^{th} dipole position of the ν^{th} sublattice relative to the ν_0 sublattice. It is possible to rewrite Eq. C.1 as

$$\mathbf{E}_{DD}^{(\nu_0)} = \sum_{\nu} \mathbf{S}_{\nu}^{(\nu_0)} \cdot \mathbf{p}_{\nu} \tag{C.2}$$

where $\mathbf{S}_{\nu}^{(\nu_0)}$ is a symmetric traceless tensor[141] of the ν^{th} sublattice, whose origin is relative to the ν_0 sublattice and $\mathbf{p}_{\nu}$ is the dipole species of the ν^{th} lattice. The details of calculating $\mathbf{S}$ involve summations of rapidly decaying exponentials, related to the symmetry of the lattice, found in Ref [141]. We note that in the calculation of $\mathbf{S}$ it is assumed that the shape of the material is a slab, which fixes the depolarization field to be only in the direction of the spontaneous polarization.

C.2 Energy of the dipole lattice-ferroelectric system

The ferroelectric-DD complex can be described as a ferroelectric crystal embedded with electric DDs and elastic DDs[142, 96] and immersed in the DD electric field. Then, the energy density is defined as

$$w = -\sum_{\nu} \mathbf{P}_{\nu} \cdot \mathbf{E}_{DD} - \mathbf{P}_s(\{\boldsymbol{\lambda}\}) \cdot \mathbf{E}_{DD} - \sum_{\nu} g_{\nu}(\boldsymbol{\lambda}_{\nu}) \tag{C.1}$$

where $\mathbf{P}_{\nu} \equiv \mathbf{p}_{\nu}/\Omega_{\nu}$ the polarization density of the ν^{th} sublattice, Ω_{ν} is the primitive unit cell of the ν^{th} sublattice, $\boldsymbol{\lambda}_{\nu}$ is the elastic dipole tensor of the ν^{th} sublattice, $\mathbf{P}_s$ is the spontaneous polarization density and g_{ν} is the free energy of the elastic DD from the ν^{th} sublattice. We emphasize that the spontaneous polarization is modified by the presence of the elastic DDs. It can be shown[142] that g_{ν} is linear in $\boldsymbol{\lambda}_{\nu}$ and $\boldsymbol{\lambda}_{\nu}$ is proportional to linear combinations of $\mathbf{a}^{-1} \cdot \partial \mathbf{a}/\partial \Omega_{\nu}^{-1}$ where $\mathbf{a}$ is the lattice vector of the ferroelectric primitive unit cell. Experimentally it is observed that DDs are stabilized when then the perovskite has tetragonal symmetry[93] and first principle calculations show that the lattice constants and polarization change slowly under strain.[143] Therefore, for a ferroelectric perovskite, we expect the lattice constants to have a weak dependence on the defect density, so that we can drop the last term because it is approximately constant and consider the energy density of the system to be

$$w = -\sum_{\nu} \mathbf{P}_{\nu} \cdot \mathbf{E}_{DD} - \mathbf{P}_s \cdot \mathbf{E}_{DD} \tag{C.2}$$

where we note that the spontaneous polarization is for a pristine ferroelectric.

C.3 Orthorhombic dipole lattices

We consider a set of dipole lattices, listed in Table 2, of either a single dipole species with a net in-plane dipole moment or two dipole species without a net in-plane dipole moment. We find, for fixed dipole densities, dipole lattices with a net in-plane dipole moment are more stable than dipole lattices without. When increasing the out-of-plane (in-plane) dipole density, the stability, shown in Fig. 27, of the dipole lattices with a net in-plane dipole moment is higher (lower) than dipole lattices without a net in-plane moment. In our DFT simulations the in-plane defect density is always smaller than the out-of-plane defect density and contains a net in-plane dipole moment which justifies not considering more than one dipolar defect.

Lattice	Species	Sublattice Origin
U	$(0,0,p)$	$(0,0,0)$
A_+	$\frac{1}{\sqrt{2}}(p,0,p)$	$(0,0,0),\ \frac{1}{2}(a,0,0)$
A_-	$\frac{1}{\sqrt{2}}(p,0,p)$	$(0,0,0)$
	$\frac{1}{\sqrt{2}}(-p,0,p)$	$\frac{1}{2}(a,0,0)$
B_+	$\frac{1}{\sqrt{2}}(p,0,p)$	$(0,0,0),\ \frac{1}{2}(a,b,0)$
B_-	$\frac{1}{\sqrt{2}}(p,0,p)$	$(0,0,0)$
	$\frac{1}{\sqrt{2}}(-p,0,p)$	$\frac{1}{2}(a,b,0)$
C_+	$\frac{1}{\sqrt{2}}(p,0,p)$	$(0,0,0),\ \frac{1}{2}(a,b,c)$
C_-	$\frac{1}{\sqrt{2}}(p,0,p)$	$(0,0,0)$
	$\frac{1}{\sqrt{2}}(-p,0,p)$	$\frac{1}{2}(a,b,c)$

Table 2: Dipole lattices, where p is the dipole moment and a, b and c are the axial distances of the orthorhombic lattice.

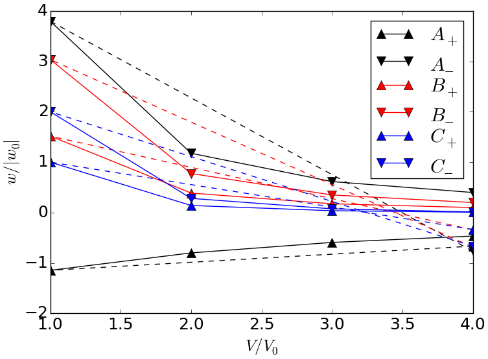

Figure 27: Energy densities w of dipole lattices normalized to the energy density of the U lattice w_0 with unit axial distances and cell volume V_0. Solid and dashed lines represent increasing the axial distance of c and $a, b(= a)$, respectively. Here the volume V of an orthorhombic cell is ca^2.

D Stochastic hysteresis

Hysteresis can be broadly understood as an overshoot phenomena, where a system responds, relative to the rate of transitions between its states, to a time dependent perturbation. For a uniaxial ferroelectric material, we typically present its states, within the Landau framework, as a free energy surface defined by the double well potential

$$\Phi(P,t) = \frac{1}{4}bP^4 - \frac{1}{2}aP^2 - E(t)P \tag{D.1}$$

and

$$E(t) = E_0 + E_\omega t \tag{D.2}$$

where E_0 and E_ω is the built-in bias and sweep rate of the electric field, respectively. Here the coupling between the time dependent electric field and the polarization is the perturbation that leads to the transition between the stable and metastable state.

Modeling the hysteresis involves determining the probability distribution ρ of a successful transition at $E(\tau)$, where τ is the mean first passage time (MFPT), the average time needed for one state to transition into the other. For $E_\omega = 0$, the MFPT can be approximated, in the overdamped limit, by quadrature[80] to be

$$\tau(P;E) = \frac{1}{D}\int_P^{P_b} dP' e^{\Phi(P')/D} \int_{P_m}^{P'} dP'' e^{-\Phi(P'')/D}, \qquad P_b > P_m \tag{D.3}$$

where D, P_b and P_m is the diffusion constant, the polarization at the barrier and the polarization at the local minimum we start in, respectively. When $E_\omega \neq 0$ it turns out that τ and likewise ρ cannot be calculated by quadrature because the bounds, P_b and P_m, now have a time dependence, which is equivalent to having time independent bounds, but at the cost of a multidimensional τ.[85]

Instead we consider the sweeping field to be a series of successive "microsteps" such that

$$E(\tau) \equiv E_n = E_0 + E_\omega n\Delta \tag{D.4}$$

where Δ is the time step connecting rapidly equilibrated states, whose value does not influence the results. Under such an approximation,[86] we can

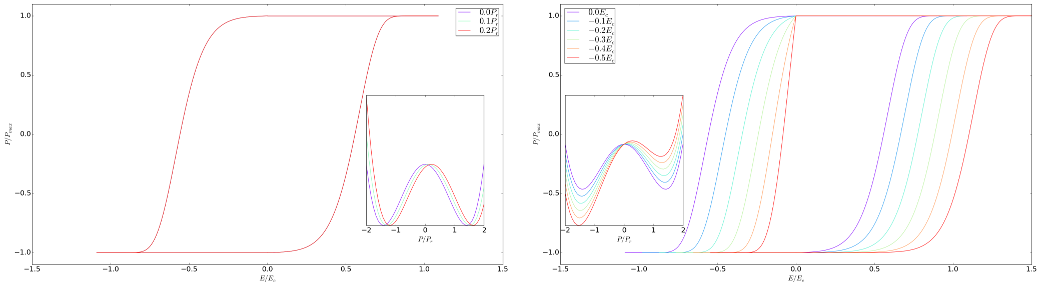

(a)

(b)

Figure 28: The hysteresis of a ferroelectric system where the free energy Φ is (a) rigidly shifted and (b) asymmetrical, respectively. The inset shows the free energy in arbitrary units of energy.

write an iterative solution for the probability distribution as

$$\rho(E(\tau)) \equiv \rho(E_n) = \left[1 - \sum_{i}^{n-1} \rho(E_i)\Delta\right] \frac{e^{-\Delta/\tau(P_m;E_n)}}{\tau(P_m;E_n)}. \tag{D.5}$$

We emphasize that the approximation breaks down when E_0 is near the transition where Φ has a single well. Finally, we can write the polarization, normalized to its maximum magnitude, as

$$P(E(\tau)) = 1 - 2\int_{E(\tau)}^{E_0} \rho(E')dE' \tag{D.6}$$

which gives the upper branch of the hysteresis loop, with the lower branch given by recalculating τ when P_b is less than P_m and the sign of E_ω is reversed.

Our results, reveal that a rigid shift in Φ, shown in the inset of Fig. 28a, does not lead to any changes in the observed hysteresis. Therefore, rigid shifts in the hysteresis, require an asymmetric Φ as shown in Fig. 28b. The values used in our calculations for a, b, E_ω, D, Δ, E_c and P_r were 2.0, 1.0, 5.4×10^{-3}, 0.1, 5.0×10^{-4}, 1.0887 and 2.0, respectively.

E Defect concentration

For a given superlattice period we can have a wide range of defect concentrations within a simulation, that depend on the supercell area and length.

In practice, the supercell length is that of a single bilayer, while the supercell area varies depending on which properties are of interest in the superlattice. Therefore, from a theoretical point of view, it is fruitful to discuss quantities such as energy and number of divacancies per supercell area. However to link theory and experiments we calculate an order of magnitude value for the defect concentration. The order of magnitude value should be the same for both STO/PTO and SRO/PTO due to the volumetric difference between STO/PTO and SRO/PTO is only in the number of unit cells of the bilayer which is 7 and 8, respectively. The supercell area contains 8 unit cells and we approximate the a and c lattice constants to both be 4 Å. Therefore the supercell volume is 10^3 Å^3, which corresponds to defect concentration of 10^{-21} cm^{-3}.

F Thermochemistry

The formation energies of Pb-O divacancies can be calculated by

$$E_{\text{form}} = E_D - E_H + q(\epsilon_v + \Delta\epsilon_F) + \sum_i n_i \mu_i \tag{F.1}$$

where E_D, E_H, ϵ_v, $\Delta\epsilon_F$, n_i and μ_i is the total energy of host+defect supercell, total energy of host supercell, energy of the valence band maximum of the host, Fermi energy relative to the VBM, number of i'th defects in the supercell and chemical potential of the i'th defect. The chemical potentials chosen are such that they correspond to the details of the experimental conditions.[126] The results, summarized in Table 3, highlight that regardless of the chemical potential used, forming a divacancy in the PRO is always more energetically favorable, sometimes even thermodynamically favorable. We note that the chemical potential channel where the divacancy is formed through the loss and gain of a PTO and TiO_2 unit cell, respectively, would not be possible in bulk PRO, however because we ultimately consider superlattices with both SRO and PTO present, these channels would not be forbidden.

References

[1] J.-M. T. Karin M. Rabe, Charles H. Ahn, *Physics of Ferroelectrics: A Modern Perspective (Topics in Applied Physics)*. Springer, 2007.

Chemical Potential	E_{form} (eV)	
	$PbRuO_3$	$PbTiO_3$
Pb + $\frac{1}{2}O_2$	3.923	6.589
PbO (OP)	0.357	3.023
$PbRuO_3$ - RuO_2 (OR)	0.986	3.652
$PbTiO_3$(PE) - TiO_2 (OR)	-0.185	2.481
$PbTiO_3$(FE) - TiO_2 (OR)	-0.237	2.429

Table 3: Formation energies for a Pb-O divacancy in either a 2×2×2 $PbRuO_3$ or $PbTiO_3$ supercell constrained to the $SrTiO_3$ lattice constant. OP and OR refer to oxygen poor and oxygen rich environments, which would be present in experiments.

[2] S. Denev, A. Kumar, M. D. Biegalski, H. W. Jang, C. M. Folkman, A. Vasudevarao, Y. Han, I. M. Reaney, S. Trolier-McKinstry, C.-B. Eom, D. G. Schlom, and V. Gopalan, "Magnetic color symmetry of lattice rotations in a diamagnetic material," *Phys. Rev. Lett.*, vol. 100, p. 257601, Jun 2008.

[3] B. D. Qu, W. L. Zhong, and R. H. Prince, "Interfacial coupling in ferroelectric superlattices," *Phys. Rev. B*, vol. 55, pp. 11218–11224, May 1997.

[4] R. T. Tung, "Recent advances in schottky barrier concepts," *Materials Science and Engineering: R: Reports*, vol. 35, pp. 1–138, nov 2001.

[5] P. Chandra and P. B. Littlewood, *A Landau Primer for Ferroelectrics*, pp. 69–116. Berlin, Heidelberg: Springer Berlin Heidelberg, 2007.

[6] J. F. Scott, "A review of ferroelectric switching," *Ferroelectrics*, vol. 503, pp. 117–132, oct 2016.

[7] D. J. Jung, M. Dawber, J. F. Scott, L. J. Sinnamon, and J. M. Gregg, "Switching dynamics in ferroelectric thin films: An experimental survey," *Integrated Ferroelectrics*, vol. 48, no. 1, pp. 59–68, 2002.

[8] R. E. Cohen, "Origin of ferroelectricity in perovskite oxides," *Nature*, vol. 358, pp. 136–138, jul 1992.

[9] G. Santi and T. Jarlborg, "Calculation of the electronic structure and the magnetic properties of and," *Journal of Physics: Condensed Matter*, vol. 9, pp. 9563–9584, nov 1997.

[10] L. Klein, J. S. Dodge, C. H. Ahn, G. J. Snyder, T. H. Geballe, M. R. Beasley, and A. Kapitulnik, "Anomalous spin scattering effects in the badly metallic itinerant ferromagnet srruo_3," *Phys. Rev. Lett.*, vol. 77, pp. 2774–2777, Sep 1996.

[11] M. Dawber, C. Lichtensteiger, M. Cantoni, M. Veithen, P. Ghosez, K. Johnston, K. M. Rabe, and J.-M. Triscone, "Unusual behavior of the ferroelectric polarization in $\mathrm{pbtio}_3/\mathrm{srtio}_3$ superlattices," *Phys. Rev. Lett.*, vol. 95, p. 177601, Oct 2005.

[12] E. Bousquet, M. Dawber, N. Stucki, C. Lichtensteiger, P. Hermet, S. Gariglio, J.-M. Triscone, and P. Ghosez, "Improper ferroelectricity in perovskite oxide artificial superlattices," *Nature*, vol. 452, pp. 732–736, apr 2008.

[13] S. J. Callori, J. Gabel, D. Su, J. Sinsheimer, M. V. Fernandez-Serra, and M. Dawber, "Ferroelectric $\mathrm{pbtio}_3/\mathrm{srruo}_3$ superlattices with broken inversion symmetry," *Phys. Rev. Lett.*, vol. 109, p. 067601, Aug 2012.

[14] S. Pöykkö and D. J. Chadi, "Dipolar defect model for fatigue in ferroelectric perovskites," *Phys. Rev. Lett.*, vol. 83, pp. 1231–1234, Aug 1999.

[15] L. D. Landau, "On the theory of phase transitions," in *Collected Papers of L.D. Landau* (D. T. Haar, ed.), pp. 193 – 216, Pergamon, 1965.

[16] M. Ernzerhof, "Taylor-series expansion of density functionals," *Phys. Rev. A*, vol. 50, pp. 4593–4607, Dec 1994.

[17] F. Aryasetiawan, *Group Theory.* Berlin, Heidelberg: University of Lund, 1997.

[18] D. J. Amit, "The ginzburg criterion-rationalized," *Journal of Physics C: Solid State Physics*, vol. 7, no. 18, p. 3369, 1974.

[19] A. Devonshire, "Theory of ferroelectrics," *Advances in Physics*, vol. 3, no. 10, pp. 85–130, 1954.

[20] K.-H. Chew, L.-H. Ong, and M. Iwata, "Switching dynamics in ferroelectric superlattices," *Current Applied Physics*, vol. 11, pp. 755–761, may 2011.

[21] C. G. Broyden, "A class of methods for solving nonlinear simultaneous equations," *Mathematics of Computation*, vol. 19, no. 92, pp. 577–577, 1965.

[22] R. Resta and D. Vanderbilt, *Theory of Polarization: A Modern Approach*, pp. 31–68. Berlin, Heidelberg: Springer Berlin Heidelberg, 2007.

[23] R. Resta, "Theory of the electric polarization in crystals," *Ferroelectrics*, vol. 136, no. 1, pp. 51–55, 1992.

[24] M. Born and V. Fock, "Beweis des adiabatensatzes," *Zeitschrift für Physik*, vol. 51, pp. 165–180, Mar 1928.

[25] R. D. King-Smith and D. Vanderbilt, "Theory of polarization of crystalline solids," *Phys. Rev. B*, vol. 47, pp. 1651–1654, Jan 1993.

[26] M. Kolodrubetz, D. Sels, P. Mehta, and A. Polkovnikov, "Geometry and non-adiabatic response in quantum and classical systems," *Physics Reports*, vol. 697, pp. 1 – 87, 2017. Geometry and non-adiabatic response in quantum and classical systems.

[27] D. J. Thouless, "Quantization of particle transport," *Phys. Rev. B*, vol. 27, pp. 6083–6087, May 1983.

[28] G. H. Wannier, "The structure of electronic excitation levels in insulating crystals," *Phys. Rev.*, vol. 52, pp. 191–197, Aug 1937.

[29] E. Blount, "Formalisms of band theory," vol. 13, pp. 305 – 373, 1962.

[30] N. Marzari and D. Vanderbilt, "Maximally localized generalized wannier functions for composite energy bands," *Phys. Rev. B*, vol. 56, pp. 12847–12865, Nov 1997.

[31] W. Kohn and L. J. Sham, "Self-consistent equations including exchange and correlation effects," *Phys. Rev.*, vol. 140, pp. A1133–A1138, Nov 1965.

[32] P. Hohenberg and W. Kohn, “Inhomogeneous electron gas,” *Phys. Rev.*, vol. 136, pp. B864–B871, Nov 1964.

[33] R. Fukuda, T. Kotani, Y. Suzuki, and S. Yokojima, “Density functional theory through legendre transformation,” *Progress of Theoretical Physics*, vol. 92, no. 4, p. 833, 1994.

[34] N. Argaman and G. Makov, “Density functional theory: An introduction,” *American Journal of Physics*, vol. 68, no. 1, pp. 69–79, 2000.

[35] O. Gunnarsson and B. I. Lundqvist, “Exchange and correlation in atoms, molecules, and solids by the spin-density-functional formalism,” *Phys. Rev. B*, vol. 13, pp. 4274–4298, May 1976.

[36] I. Gelfand and S. Fomin, “Calculus of variations..” Revised English edition. Translated and edited by Richard A. Silverman. 3rd. printing. Englewood Cliffs, N.J.: Prentice-Hall, Inc. VII, 232 p. (1965)., 1965.

[37] M. S. Hybertsen and S. G. Louie, “Electron correlation in semiconductors and insulators: Band gaps and quasiparticle energies,” *Phys. Rev. B*, vol. 34, pp. 5390–5413, Oct 1986.

[38] J. Paldus, “Group theoretical approach to the configuration interaction and perturbation theory calculations for atomic and molecular systems,” *The Journal of Chemical Physics*, vol. 61, no. 12, pp. 5321–5330, 1974.

[39] J. Wang, G. Romn-Prez, J. M. Soler, E. Artacho, and M.-V. Fernndez-Serra, “Density, structure, and dynamics of water: The effect of van der waals interactions,” *The Journal of Chemical Physics*, vol. 134, no. 2, p. 024516, 2011.

[40] W. Kohn, Y. Meir, and D. E. Makarov, “van der waals energies in density functional theory,” *Phys. Rev. Lett.*, vol. 80, pp. 4153–4156, May 1998.

[41] G. Zhang and C. B. Musgrave, “Comparison of dft methods for molecular orbital eigenvalue calculations,” *The Journal of Physical Chemistry A*, vol. 111, no. 8, pp. 1554–1561, 2007. PMID: 17279730.

[42] J. M. Soler, E. Artacho, J. D. Gale, A. Garcia, J. Junquera, P. Ordejon, and D. Sanchez-Portal, "The siesta method for ab initio order- n materials simulation," *Journal of Physics: Condensed Matter*, vol. 14, no. 11, p. 2745, 2002.

[43] N. Troullier and J. L. Martins, "Efficient pseudopotentials for plane-wave calculations," *Phys. Rev. B*, vol. 43, pp. 1993–2006, Jan 1991.

[44] D. R. Hamann, M. Schlüter, and C. Chiang, "Norm-conserving pseudopotentials," *Phys. Rev. Lett.*, vol. 43, pp. 1494–1497, Nov 1979.

[45] L. Kleinman and D. M. Bylander, "Efficacious form for model pseudopotentials," *Phys. Rev. Lett.*, vol. 48, pp. 1425–1428, May 1982.

[46] O. F. Sankey and D. J. Niklewski, "Ab initio," *Phys. Rev. B*, vol. 40, pp. 3979–3995, Aug 1989.

[47] E. Artacho, D. Snchez-Portal, P. Ordejn, A. Garca, and J. M. Soler, "Linear-scaling ab-initio calculations for large and complex systems," *physica status solidi (b)*, vol. 215, no. 1, pp. 809–817, 1999.

[48] P. E. Blöchl, "Projector augmented-wave method," *Phys. Rev. B*, vol. 50, pp. 17953–17979, Dec 1994.

[49] J. Moreno and J. M. Soler, "Optimal meshes for integrals in real- and reciprocal-space unit cells," *Phys. Rev. B*, vol. 45, pp. 13891–13898, Jun 1992.

[50] H. J. Monkhorst and J. D. Pack, "Special points for brillouin-zone integrations," *Phys. Rev. B*, vol. 13, pp. 5188–5192, Jun 1976.

[51] N. W. Ashcroft and N. D. Mermin, *Solid State Physics.* Brooks Cole, 1976.

[52] M. C. Payne, M. P. Teter, D. C. Allan, T. A. Arias, and J. D. Joannopoulos, "Iterative minimization techniques for ab initio total-energy calculations: molecular dynamics and conjugate gradients," *Rev. Mod. Phys.*, vol. 64, pp. 1045–1097, Oct 1992.

[53] R. Car and M. Parrinello, "Unified approach for molecular dynamics and density-functional theory," *Phys. Rev. Lett.*, vol. 55, pp. 2471–2474, Nov 1985.

[54] R. Rosenberg, *Analytical Dynamics of Discrete Systems.* Springer, 2012.

[55] L. Verlet, “Computer ”experiments” on classical fluids. i. thermodynamical properties of lennard-jones molecules,” *Phys. Rev.*, vol. 159, pp. 98–103, Jul 1967.

[56] G. Nenciu, “Dynamics of band electrons in electric and magnetic fields: rigorous justification of the effective hamiltonians,” *Rev. Mod. Phys.*, vol. 63, pp. 91–127, Jan 1991.

[57] J. E. Avron, J. Zak, A. Grossmann, and L. Gunther, “Instability of the continuous spectrum: The n-band stark ladder,” *Journal of Mathematical Physics*, vol. 18, pp. 918–921, may 1977.

[58] I. Souza, J. Íñiguez, and D. Vanderbilt, “First-principles approach to insulators in finite electric fields,” *Phys. Rev. Lett.*, vol. 89, p. 117602, Aug 2002.

[59] M. Stengel, N. A. Spaldin, and D. Vanderbilt, “Electric displacement as the fundamental variable in electronic-structure calculations,” *Nature Physics*, vol. 5, pp. 304–308, feb 2009.

[60] O. Diéguez and D. Vanderbilt, “First-principles calculations for insulators at constant polarization,” *Phys. Rev. Lett.*, vol. 96, p. 056401, Feb 2006.

[61] W. Kohn, “Analytic properties of bloch waves and wannier functions,” *Phys. Rev.*, vol. 115, pp. 809–821, Aug 1959.

[62] A. Baldereschi, S. Baroni, and R. Resta, “Band offsets in lattice-matched heterojunctions: A model and first-principles calculations for gaas/alas,” *Phys. Rev. Lett.*, vol. 61, pp. 734–737, Aug 1988.

[63] S. O. K. Prof., *Principles of Electronic Materials and Devices.* McGraw-Hill Education, 2005.

[64] J. J. Rehr and W. Kohn, “Wannier functions in crystals with surfaces,” *Phys. Rev. B*, vol. 10, pp. 448–455, Jul 1974.

[65] J. Tersoff, “Theory of semiconductor heterojunctions: The role of quantum dipoles,” *Phys. Rev. B*, vol. 30, pp. 4874–4877, Oct 1984.

[66] R. E. Allen, "Green's functions for surface physics," *Phys. Rev. B*, vol. 20, pp. 1454–1472, Aug 1979.

[67] F. Garcia-Moliner and F. Flores, *Introduction to the Theory of Solid Surfaces (Cambridge Monographs on Physics)*. Cambridge University Press, 2009.

[68] M. Stengel, P. Aguado-Puente, N. A. Spaldin, and J. Junquera, "Band alignment at metal/ferroelectric interfaces: Insights and artifacts from first principles," *Phys. Rev. B*, vol. 83, p. 235112, Jun 2011.

[69] R. R. Mehta, B. D. Silverman, and J. T. Jacobs, "Depolarization fields in thin ferroelectric films," *Journal of Applied Physics*, vol. 44, no. 8, pp. 3379–3385, 1973.

[70] S. Li, J. Eastman, Z. Li, C. Foster, R. Newnham, and L. Cross, "Size effects in nanostructured ferroelectrics," *Physics Letters A*, vol. 212, no. 6, pp. 341 – 346, 1996.

[71] F. Kroger, *The Chemistry of Imperfect Crystals.* North-Holland, 1st ed., 1964.

[72] S. Lany and A. Zunger, "Assessment of correction methods for the band-gap problem and for finite-size effects in supercell defect calculations: Case studies for zno and gaas," *Phys. Rev. B*, vol. 78, p. 235104, Dec 2008.

[73] C. Persson, Y.-J. Zhao, S. Lany, and A. Zunger, "n," *Phys. Rev. B*, vol. 72, p. 035211, Jul 2005.

[74] S. Lany and A. Zunger, "Anion vacancies as a source of persistent photoconductivity in ii-vi and chalcopyrite semiconductors," *Phys. Rev. B*, vol. 72, p. 035215, Jul 2005.

[75] E. Burstein, "Anomalous optical absorption limit in insb," *Phys. Rev.*, vol. 93, pp. 632–633, Feb 1954.

[76] J. Ihm, A. Zunger, and M. L. Cohen, "Momentum-space formalism for the total energy of solids," *Journal of Physics C: Solid State Physics*, vol. 12, no. 21, p. 4409, 1979.

[77] G. Makov and M. C. Payne, "Periodic boundary conditions in ab initio calculations," *Phys. Rev. B*, vol. 51, pp. 4014–4022, Feb 1995.

[78] J. Lamperti, *Stochastic Processes: A Survey of the Mathematic Theory.* Springer-Verlag Berlin and Heidelberg GmbH & Co. K, 1977.

[79] L. Onsager, "Reciprocal relations in irreversible processes. i.," *Phys. Rev.*, vol. 37, pp. 405–426, Feb 1931.

[80] R. Zwanzig, *Nonequilibrium Statistical Mechanics.* Oxford University Press, 2001.

[81] H. Kramers, "Brownian motion in a field of force and the diffusion model of chemical reactions," *Physica*, vol. 7, no. 4, pp. 284 – 304, 1940.

[82] E. Nelson, *Dynamical Theories of Brownian Motion.* Princeton University Press, 1967.

[83] A. H. Nayfeh, *Perturbation Methods.* Wiley-VCH, 2000.

[84] M. I. Freidlin and A. D. Wentzell, *Random Perturbations of Dynamical Systems.* Springer, 1998.

[85] H. C. Tuckwell and F. Y. M. Wan, "First-passage time of markov processes to moving barriers," *Journal of Applied Probability*, vol. 21, pp. 695–709, dec 1984.

[86] M. C. Mahato and S. R. Shenoy, "Langevin dynamic simulation of hysteresis in a field-swept landau potential," *Journal of Statistical Physics*, vol. 73, pp. 123–145, oct 1993.

[87] W. Eerenstein, N. D. Mathur, and J. F. Scott, "Multiferroic and magnetoelectric materials," *Nature*, vol. 442, pp. 759–765, aug 2006.

[88] Y. I. K. and D. S. B., "Mechanism of fatigue in ferroelectric thin films," *physica status solidi (a)*, vol. 133, no. 2, pp. 565–573.

[89] C. H. Park and D. J. Chadi, "Microscopic study of oxygen-vacancy defects in ferroelectric perovskites," *Phys. Rev. B*, vol. 57, pp. R13961–R13964, Jun 1998.

[90] M. Dawber and J. F. Scott, “A model for fatigue in ferroelectric perovskite thin films,” *Applied Physics Letters*, vol. 76, no. 8, pp. 1060–1062, 2000.

[91] M.-G. Han, J. A. Garlow, M. Bugnet, S. Divilov, M. S. J. Marshall, L. Wu, M. Dawber, M. Fernandez-Serra, G. A. Botton, S.-W. Cheong, F. J. Walker, C. H. Ahn, and Y. Zhu, “Coupling of bias-induced crystallographic shear planes with charged domain walls in ferroelectric oxide thin films,” *Phys. Rev. B*, vol. 94, p. 100101, Sep 2016.

[92] P. V. Lambeck and G. H. Jonker, “Ferroelectric domain stabilization in batio3 by bulk ordering of defects,” *Ferroelectrics*, vol. 22, no. 1, pp. 729–731, 1978.

[93] W. L. Warren, G. E. Pike, K. Vanheusden, D. Dimos, B. A. Tuttle, and J. Robertson, “Defectdipole alignment and tetragonal strain in ferroelectrics,” *Journal of Applied Physics*, vol. 79, no. 12, pp. 9250–9257, 1996.

[94] J. F. Scott, C. A. Araujo, B. M. Melnick, L. D. McMillan, and R. Zuleeg, “Quantitative measurement of spacecharge effects in lead zirconatetitanate memories,” *Journal of Applied Physics*, vol. 70, no. 1, pp. 382–388, 1991.

[95] C. M. Folkman, S. H. Baek, C. T. Nelson, H. W. Jang, T. Tybell, X. Q. Pan, and C. B. Eom, “Study of defect-dipoles in an epitaxial ferroelectric thin film,” *Applied Physics Letters*, vol. 96, no. 5, p. 052903, 2010.

[96] G. Arlt and H. Neumann, “Internal bias in ferroelectric ceramics: Origin and time dependence,” *Ferroelectrics*, vol. 87, no. 1, pp. 109–120, 1988.

[97] W. L. Warren, D. Dimos, B. A. Tuttle, G. E. Pike, and H. N. Alshareef, “Relationships among ferroelectric fatigue, electronic charge trapping, defect-dipoles, and oxygen vacancies in perovskite oxides,” *Integrated Ferroelectrics*, vol. 16, no. 1-4, pp. 77–86, 1997.

[98] C. Brennan, “Model of ferroelectric fatigue due to defect/domain interactions,” *Ferroelectrics*, vol. 150, no. 1, pp. 199–208, 1993.

[99] M. B. Okatan, J. V. Mantese, and S. P. Alpay, "Polarization coupling in ferroelectric multilayers," *Phys. Rev. B*, vol. 79, p. 174113, May 2009.

[100] M. J. Haun, E. Furman, S. J. Jang, H. A. McKinstry, and L. E. Cross, "Thermodynamic theory of pbtio3," *Journal of Applied Physics*, vol. 62, no. 8, pp. 3331–3338, 1987.

[101] D. Balzar, P. A. Ramakrishnan, and A. M. Hermann, "Defect-related lattice strain and the transition temperature in ferroelectric thin films," *Phys. Rev. B*, vol. 70, p. 092103, Sep 2004.

[102] H.-L. Hu and L.-Q. Chen, "Computer simulation of 90 ferroelectric domain formation in two-dimensions," *Materials Science and Engineering: A*, vol. 238, no. 1, pp. 182 – 191, 1997. Microstructure Evolution in Bulk Phases F.

[103] O. Penrose and P. C. Fife, "Thermodynamically consistent models of phase-field type for the kinetic of phase transitions," *Physica D: Nonlinear Phenomena*, vol. 43, no. 1, pp. 44 – 62, 1990.

[104] I. Müller, "On the entropy inequality," *Archive for Rational Mechanics and Analysis*, vol. 26, pp. 118–141, jan 1967.

[105] "82 - on the anomalous absorption of sound near a second order phase transition point," in *Collected Papers of L.D. Landau* (D. T. HAAR, ed.), pp. 626 – 629, Pergamon, 1965.

[106] S. R. P. Smith, D. R. Tilley, and C. L. Wang, "Recent applications of landau theory to ferroelectric structures," *Ferroelectrics*, vol. 197, no. 1, pp. 105–110, 1997.

[107] Y. Ishibashi, "Theory of polarization reversals in ferroelectrics based on landau-type free energy," *Japanese Journal of Applied Physics*, vol. 31, no. 9R, p. 2822, 1992.

[108] P. Ván, "The ginzburg-landau equation as a consequence of the second law," *Continuum Mechanics and Thermodynamics*, vol. 17, pp. 165–169, May 2005.

[109] J. C. Butcher, *Numerical methods for ordinary differential equations.* Chichester, West Sussex, England Hoboken, NJ: J. Wiley, 2003.

[110] E. Cockayne and B. P. Burton, “Dipole moment of a pb-o vacancy pair in pbtio$_3$,” *Phys. Rev. B*, vol. 69, p. 144116, Apr 2004.

[111] J. P. Perdew and Y. Wang, “Accurate and simple analytic representation of the electron-gas correlation energy,” *Phys. Rev. B*, vol. 45, pp. 13244–13249, Jun 1992.

[112] A. Roy, M. Stengel, and D. Vanderbilt, “First-principles study of high-field piezoelectricity in tetragonal pbtio$_3$,” *Phys. Rev. B*, vol. 81, p. 014102, Jan 2010.

[113] C. Cazorla and M. Stengel, “Electrostatic engineering of strained ferroelectric perovskites from first principles,” *Phys. Rev. B*, vol. 92, p. 214108, Dec 2015.

[114] D. Vanderbilt and R. D. King-Smith, “Electronic polarization in the ultrasoft pseudopotential formalism,” *eprint arXiv:cond-mat/9801177*, Jan. 1998.

[115] J. B. Neaton and K. M. Rabe, “Theory of polarization enhancement in epitaxial BaTiO3/SrTiO3 superlattices,” *Applied Physics Letters*, vol. 82, pp. 1586–1588, mar 2003.

[116] K. Johnston, X. Huang, J. B. Neaton, and K. M. Rabe, “First-principles study of symmetry lowering and polarization inBaTiO3SrTiO3superlattices with in-plane expansion,” *Physical Review B*, vol. 71, mar 2005.

[117] J. Zhang, R. Xu, A. R. Damodaran, Z.-H. Chen, and L. W. Martin, “Understanding order in compositionally graded ferroelectrics: Flexoelectricity, gradient, and depolarization field effects,” *Phys. Rev. B*, vol. 89, p. 224101, Jun 2014.

[118] J. C. Agar, A. R. Damodaran, G. A. Velarde, S. Pandya, R. V. K. Mangalam, and L. W. Martin, “Complex evolution of built-in potential in compositionally-graded pbzr1xtixo3 thin films,” *ACS Nano*, vol. 9, no. 7, pp. 7332–7342, 2015. PMID: 26125636.

[119] D. Lee, B. C. Jeon, S. H. Baek, S. M. Yang, Y. J. Shin, T. H. Kim, Y. S. Kim, J.-G. Yoon, C. B. Eom, and T. W. Noh, “Active control

of ferroelectric switching using defect-dipole engineering," *Advanced Materials*, vol. 24, no. 48, pp. 6490–6495.

[120] B. Zhao, Z. Chen, J. Meng, H. Lu, D. W. Zhang, and A. Jiang, "Ferroelectric polarization and defect-dipole switching in an epitaxial (111) bifeo3 thin film," *Journal of Applied Physics*, vol. 117, no. 20, p. 204103, 2015.

[121] H. H. Wu, J. Wang, S. G. Cao, L. Q. Chen, and T. Y. Zhang, "Micro-/macro-responses of a ferroelectric single crystal with domain pinning and depinning by dislocations," *Journal of Applied Physics*, vol. 114, no. 16, p. 164108, 2013.

[122] J. Karthik, R. V. K. Mangalam, J. C. Agar, and L. W. Martin, "Large built-in electric fields due to flexoelectricity in compositionally graded ferroelectric thin films," *Phys. Rev. B*, vol. 87, p. 024111, Jan 2013.

[123] P. Gao, C. T. Nelson, J. R. Jokisaari, S.-H. Baek, C. W. Bark, Y. Zhang, E. Wang, D. G. Schlom, C.-B. Eom, and X. Pan, "Revealing the role of defects in ferroelectric switching with atomic resolution," *Nature Communications*, vol. 2, sep 2011.

[124] J. P. Perdew and A. Zunger, "Self-interaction correction to density-functional approximations for many-electron systems," *Physical Review B*, vol. 23, pp. 5048–5079, may 1981.

[125] M. Stengel and A. D. Vita, "First-principles molecular dynamics of metals: A lagrangian formulation," *Physical Review B*, vol. 62, pp. 15283–15286, dec 2000.

[126] Z. Zhang, P. Wu, L. Lu, and C. Shu, "Study on vacancy formation in ferroelectric PbTiO3 from ab initio," *Applied Physics Letters*, vol. 88, p. 142902, apr 2006.

[127] S. Pöykkö and D. J. Chadi, "First principles study of pb vacancies in PbTiO3," *Applied Physics Letters*, vol. 76, pp. 499–501, jan 2000.

[128] H. Funakubo, T. Watanabe, H. Morioka, A. Nagai, T. Oikawa, M. Suzuki, H. Uchida, S. Kouda, and K. Saito, "Polarization comparison of pb(zr,ti)o3 and bi4ti3o12-based ferroelectrics," *Materials Science and Engineering: B*, vol. 118, no. 1, pp. 23 – 27, 2005. EMRS

2004, Symposium D: Functional Oxides for Advanced Semiconductor Technologies.

[129] D. D. Fong, G. B. Stephenson, S. K. Streiffer, J. A. Eastman, O. Auciello, P. H. Fuoss, and C. Thompson, "Ferroelectricity in ultrathin perovskite films," *Science*, vol. 304, no. 5677, pp. 1650–1653, 2004.

[130] A. Munkholm, S. K. Streiffer, M. V. Ramana Murty, J. A. Eastman, C. Thompson, O. Auciello, L. Thompson, J. F. Moore, and G. B. Stephenson, "Antiferrodistortive reconstruction of the pbtio$_3$(001) surface," *Phys. Rev. Lett.*, vol. 88, p. 016101, Dec 2001.

[131] Y. Umeno, J. M. Albina, B. Meyer, and C. Elsässer, "Ab initio calculations of ferroelectric instability in pbtio$_3$ capacitors with symmetric and asymmetric electrode layers," *Phys. Rev. B*, vol. 80, p. 205122, Nov 2009.

[132] P. Aguado-Puente and J. Junquera, "Ferromagneticlike closure domains in ferroelectric ultrathin films: First-principles simulations," *Phys. Rev. Lett.*, vol. 100, p. 177601, Apr 2008.

[133] J. Junquera, M. H. Cohen, and K. M. Rabe, "Nanoscale smoothing and the analysis of interfacial charge and dipolar densities," *Journal of Physics: Condensed Matter*, vol. 19, no. 21, p. 213203, 2007.

[134] A. M. Glazer, "The classification of tilted octahedra in perovskites," *Acta Crystallographica Section B*, vol. 28, pp. 3384–3392, Nov 1972.

[135] R. E. Crandall, "Fast evaluation of epstein zeta functions," *manuscript*, 1998.

[136] I. J. Zucker, "Madelung constants and lattice sums for invariant cubic lattice complexes and certain tetragonal structures," *Journal of Physics A: Mathematical and General*, vol. 8, no. 11, p. 1734, 1975.

[137] D. Gresch, G. Autès, O. V. Yazyev, M. Troyer, D. Vanderbilt, B. A. Bernevig, and A. A. Soluyanov, "Z2pack: Numerical implementation of hybrid wannier centers for identifying topological materials," *Phys. Rev. B*, vol. 95, p. 075146, Feb 2017.

[138] U. Robels, J. H. Calderwood, and G. Arlt, “Shift and deformation of the hysteresis curve of ferroelectrics by defects: An electrostatic model,” *Journal of Applied Physics*, vol. 77, no. 8, pp. 4002–4008, 1995.

[139] B. Nijboer and F. D. Wette, “The internal field in dipole lattices,” *Physica*, vol. 24, no. 1, pp. 422 – 431, 1958.

[140] C. Kittel, *Introduction to Solid State Physics.* Wiley, 8 ed., 11 2004.

[141] F. W. de Wette and G. E. Schacher, “Internal field in general dipole lattices,” *Phys. Rev.*, vol. 137, pp. A78–A91, Jan 1965.

[142] A. S. Nowick, *Anelastic Relaxation in Crystalline Solids.* Academic Press, 2012.

[143] Y. Duan, H. Shi, and L. Qin, “Studies of tetragonal pbtio 3 subjected to uniaxial stress along the c -axis,” *Journal of Physics: Condensed Matter*, vol. 20, no. 17, p. 175210, 2008.